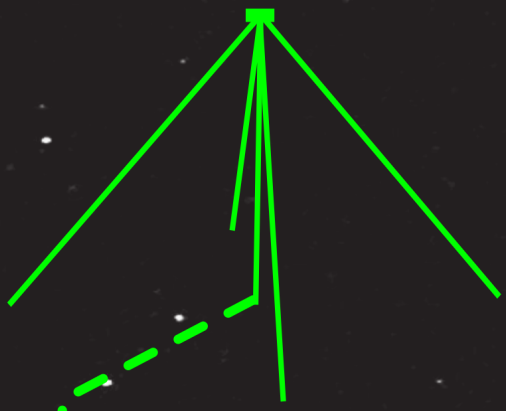

Radio Galaxies at Low Frequencies

high spatial and spectral resolution studies with LOFAR

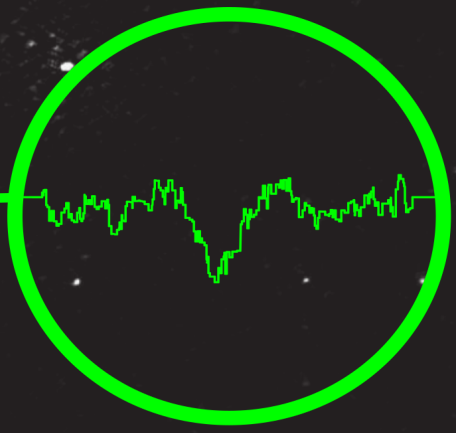

Leah K. Morabito

Radio Galaxies at Low Frequencies

high spatial and spectral resolution studies with LOFAR

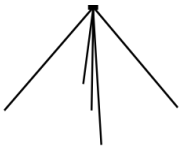

Leah K. Morabito

ISBN: 978-90-9029907-5

Cover: Design and images by Leah K. Morabito.

Background: A portion of a wide-field image around a high redshift radio galaxy, 4C 39.37, at 56 MHz using only 2 MHz of bandwidth from a Low Frequency Array observation made with the Low Band Antenna.

Foreground: At the top is a representation of a Low Band Antenna dipole. In the left circle is the stacked line profile from the first extragalactic detection of carbon radio recombination lines, and in the right circle are smoothed contours from the highest resolution image at frequencies below 100 MHz.

Radio Galaxies at Low Frequencies

high spatial and spectral resolution studies with LOFAR

Proefschrift

ter verkrijging van
de graad van Doctor aan de Universiteit Leiden,
op gezag van Rector Magnificus prof. mr. C.J.J.M. Stolker,
volgens besluit van het College voor Promoties
te verdedigen op dinsdag 13 september 2016
klokke 13:45 uur

door

Leah K. Morabito

geboren te Englewood, Colorado, Verenigde Staten
in 1983

Promotiecommissie

Promotor:	Prof. dr. Huub Röttgering	Leiden University
Co-Promotor:	Prof. dr. George Miley	Leiden University
Overige leden:	Prof. dr. Michael Garrett	ASTRON/Leiden University
	Prof. dr. Raffaella Morganti	ASTRON/University of Grongingen
	Prof. dr. Alexander Tielens	Leiden University
	Prof. dr. Huib van Langevelde	JIVE/Leiden University
	Dr. Adam Deller	ASTRON
	Dr. Huib Intema	Leiden University
	Dr. Raymond Oonk	ASTRON/Leiden University

To follow knowledge like a sinking star,
Beyond the utmost bound of human thought.
◂ Alfred Lord Tennyson ▸

Contents

List of Figures

List of Tables

CHAPTER 1

Introduction

"Space is big. You just won't believe how vastly, hugely, mind-bogglingly big it is.
I mean, you may think it's a long way down the road to the chemist's,
but that's just peanuts to space."
−Douglas Adams−

1.1 Early Radio Astronomy and Distant Radio Galaxies

Karl G. Jansky was conducting experiments in the early 1930s with telecommunications receivers for the Holmdel Radio Laboratories of Bell Telephone Laboratories, Inc. when he serendipitously detected electromagnetic radiation of an unknown origin. Using the receivers, tuned to frequencies of 20.5 MHz (wavelengths of 14.6 m), he tracked the signal for 24 hours approximately once a month during 1932. These observations led Jansky to determine that the origin of the radiation was fixed in space and localized in the direction of the Galactic center. Jansky published his results in 1933. Grote Reber read about Jansky's discovery and followed it up with observations using a radio telescope of his own design. Reber mapped the Galactic center and a bright source in the direction of the Cygnus constellation at frequencies of 3.3 GHz, 900 MHz, and 160 MHz (Reber, 1949). A census of radio 'stars' in the sky began to emerge.

In 1954 Walter Baade and Rudolph Minkowski first associated the radio source in Cygnus with a faint distant galaxy. Based on the distance to the galaxy, Baade and Minkowski came to the conclusion that the total energy of the radio emission was almost 10^{43} ergs s^{-1}, larger than the total optical emission. The discovery that galaxies could produce such large amounts of energy revolutionised astronomy, but it would be another 30 years before radio galaxies were placed as important pieces in the overall scheme of galaxy evolution.

Early studies of energetic radio sources and their optical counterparts were enabled by significant advances in radio astronomy over the next few decades.

These advances included the first use of multi-element systems by Ryle and Vonberg in 1946 and the first use of earth rotation synthesis by Ryle in 1962. The work initially focused on cataloguing the brightest sources in the sky at radio frequencies less than 200 MHz. Surveys with Cambridge interferometry mainly covered frequencies ranging from 151 to 178 MHz (Edge et al., 1959; Bennett, 1962; Pilkington & Scott, 1965). Several surveys were conducted with simple wire or dipole instruments at frequencies less than 100 MHz, including surveys from the Cambridge Interferometer at 38 MHz (Kellermann et al., 1969); the Clark Lake Radio Observatory at 26.3 MHz (Viner & Erickson, 1975); and the Dominion Radio Astrophysical Observatory 'T-shaped' radio telescope at 22 MHz (Roger et al., 1986).

The surveys revealed different types of radio sources. Many bright, powerful radio sources consisted of radio jets up to hundreds of times larger than their optical host galaxies. Fanaroff & Riley (1974) sorted these extended radio sources into two classes based on their morphological features. Fanaroff-Riley I (FR I) sources consist of radio jets that are more like fountains, with wider opening angles and dimmer radio luminosities towards their extremities. Fanaroff-Riley II (FR II) sources have highly collimated radio jets that are edge brightened where the jets terminate. An example of each class is shown in Figure 1.1. Generally FR I sources have lower radio powers ($\lesssim 10^{25}\,\mathrm{W\,Hz^{-1}}$ at 1.4 GHz) and it is thought that the jet power as well as the ambient density play a role in whether a highly collimated jet will remain collimated and turn into an FR II source or be disrupted and change into an FR I source (e.g., Kaiser & Best, 2007). In cases where the ambient density is asymmetric, hybrid sources with characteristics of both FR classes can be observed.

Until the mid-1980's radio galaxies were seen merely as exotic high-energy phenomena that were useful as a way to refine searches for distant optical host galaxies (e.g., Smith & Spinrad, 1980). In particular, a correlation emerged where radio sources with ultra-steep spectral indices ($\alpha > 1$, where flux density $S \propto \nu^{-\alpha}$) were more likely to be found at higher redshifts, see Figure 1.2 (Tielens et al., 1979; Blumenthal & Miley, 1979). This correlation has been successfully exploited to push the limit for finding massive galaxies at high redshift (e.g. Röttgering et al., 1994).

1.2 High-Redshift Radio Galaxies

1.2.1 Characteristics

The unexpected discovery in 1987 of an alignment between the radio jets and optical continuum emission for radio galaxies at $z \geq 0.7$ changed the entire way

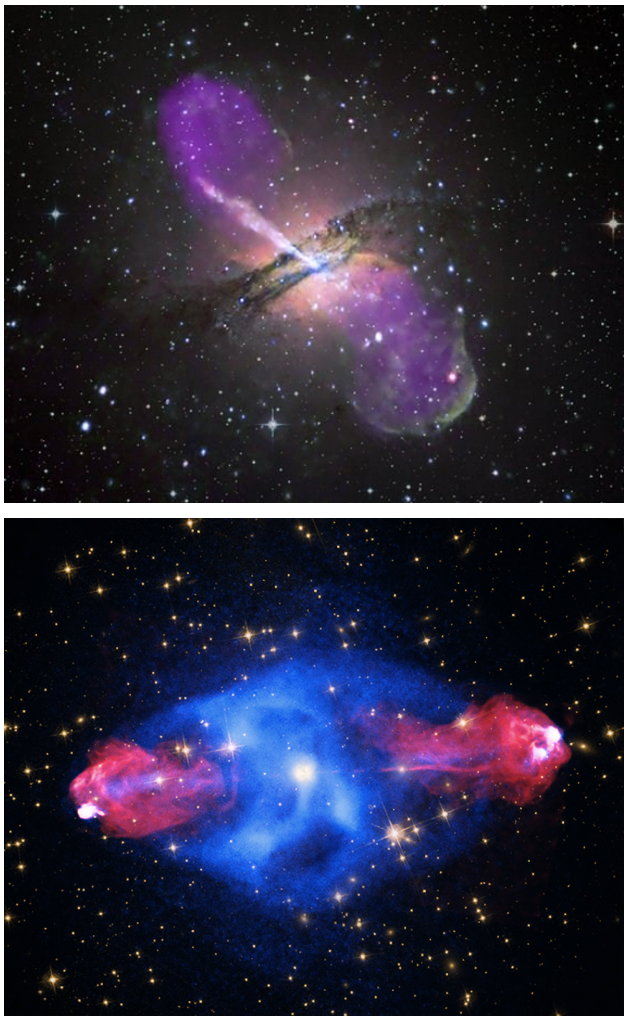

Figure 1.1: Composite images showing examples of typical Fanaroff-Riley FRI and FRII sources. *Top:* A composite image of FRI radio galaxy Centaurus A. The color purple shows the radio emission which is brighter along the jets towards the host radio galaxy, with fainter emission at the ends of the jets (Credit: X-ray: NASA/CXC/CfA/R.Kraft et al; Radio: NSF/VLA/Univ.Hertfordshire/M.Hardcastle; Optical: ESO/WFI/M.Rejkuba et al.). *Bottom:* Radio galaxy Cygnus A, the archetypal FRII radio galaxy. The color red shows the edge-brightened radio emission. The X-ray emission shown in blue traces the cocoon of shocked jet material and intergalactic medium (X-ray: NASA/CXC/SAO; Optical: NASA/STScI; Radio: NSF/NRAO/AUI/VLA).

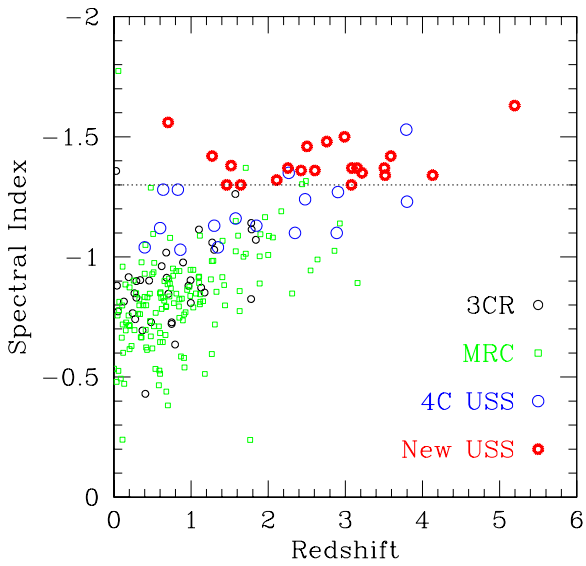

Figure 1.2: The correlation between spectral index and redshift seen for bright radio galaxies. Plot from De Breuck et al. (2000).

radio galaxies were seen (Chambers et al., 1987; McCarthy et al., 1987). Two things became clear: first, that the radio jets interact with their host galaxy and could possibly impact its evolution; and second, that high redshift radio galaxies might be fundamentally different sources than local radio galaxies, where the alignment effect is not observed. High-redshift radio galaxies (HzRGs, defined here as having $z \geq 2$) became the subject of intense multi-wavelength studies during the 1990s and 2000s. Often found surrounded by over-densities of galaxies indicating the presence of a proto-cluster, HzRGs are now thought to evolve into the most massive galaxies in the present-day Universe (e.g., Pentericci et al., 2000b; Hatch et al., 2011). They are therefore important beacons for studying the evolution of galaxies as they traverse into clusters of galaxies, which are the largest gravitationally bound objects in the Universe.

HzRGs exhibit characteristics that indicate an interaction with their host galaxies, providing a feedback mechanism by which the radio jets can influence galaxy evolution. The optical morphologies of HzRGs are clumpy and extended along the radio jet axis (e.g., Pentericci et al., 1998, 1999). Many HzRGs are embedded in huge Lyman-α haloes, indicating the presence of ionised gas (e.g., Humphrey et al., 2007). Emission lines other than Lyman-α are present and also extended along the jet axis (Motohara et al., 2000; Humphrey et al.,

2007). The kinematics indicated by these emission lines provide evidence for both an infalling quiescent halo (e.g., Villar-Martín et al., 2003; Humphrey et al., 2007) and turbulent outflows (Villar-Martín et al., 1999; Humphrey et al., 2006). Asymmetries in the radio lobes have been linked to properties of the emission lines. Humphrey et al. (2007) found that Lyman-α was always brighter in relation to other emission lines on the side of the brighter radio lobe. The spatial correlation of the emission line properties with the radio jets is strong evidence for feedback between radio jets and the host galaxy.

1.2.2 Feedback Processes

The alignment of optical continuum and the radio jets in HzRGs is not the only indication that radio jets can interact with their host galaxies. Radio jets are powered by super-massive black holes at the centre of their host galaxies. There are observed correlations between the mass of the super-massive black hole and properties of the host galaxy such as velocity dispersion (e.g., Ferrarese & Merritt, 2000; Gebhardt et al., 2000), bulge mass (e.g., Kormendy & Richstone, 1995; Magorrian et al., 1998), and galaxy luminosity (e.g., Marconi & Hunt, 2003; Gültekin et al., 2009). These correlations indicate that the super-massive black hole and its host galaxy co-evolve. Radio jets can play a part in this co-evolution, either by jet-induced star formation or by regulation of star formation via heating of cold gas that would otherwise condense into stars.

Radio jets can drive shocks into the interstellar medium, enhancing star formation by increasing turbulent pressure and compressing clouds that then form stars (e.g., Silk & Nusser, 2010). Observational evidence for this 'positive' feedback can be found in both nearby sources (e.g., Blanco et al., 1975; Donahue et al., 2002; Inskip et al., 2008) as well as HzRGs (Chambers et al., 1987; Inskip et al., 2005).

There can also be 'negative' feedback from radio jets heating up cold gas and suppressing star formation (e.g., Best et al., 2005a; Hardcastle et al., 2013). The jets can also be responsible for expelling molecular gas from the host galaxy, depleting the necessary fuel to form stars (e.g., Feruglio et al., 2010; Dasyra & Combes, 2012; Tadhunter et al., 2014). Cosmological simulations often invoke negative feedback to quench star formation in massive galaxies, bringing the simulations in line with observations of 'red and dead' massive galaxies (e.g., Bower et al., 2006; Werner et al., 2014).

1.2.3 Open Questions

Although HzRGs have been the topic of intense multi-wavelength study, many questions still remain open (for a complete list see Miley & De Breuck, 2008). One of the biggest mysteries is why HzRGs have much steeper radio spectra than their low-redshift counterparts. Although this has been a topic of intense study (e.g., Athreya & Kapahi, 1998; Blundell et al., 1999; Klamer et al., 2006) it is still unclear if the dominant cause of the relation between spectral index and redshift is observational or due to different particle acceleration mechanisms in the relativistic plasma of the radio jets. Could steeper spectra be caused by interaction with a denser ambient environment? If so, what are the detailed processes by which the jets interact with their environments? How exactly does feedback between the host galaxy and the energetic processes associated with the radio jets impact the galaxy's evolution? The vigorous star formation and the jets themselves have to be fuelled, but not all gas phases present in HzRGs are well constrained. In particular, it is important to characterise the molecular and cold gas content of HzRGs.

This thesis aims to provide new low radio frequency information on the particle acceleration mechanisms present in HzRGs and lay the foundation for studying the cold gas content of HzRGs via observations of low frequency carbon radio recombination lines. The rest of this chapter will outline for the reader the relevant topics of active galactic nuclei and low frequency carbon radio recombination lines.

1.3 Active Galactic Nuclei

In 1963 the Dutch astronomer Maarten Schmidt observed the spectrum of the unresolved optical counterpart of the bright radio source 3C 273. The measured cosmological redshift $z = 0.158$ revealed that the compact optical source, identified as the nuclear region of a galaxy, was 100 times brighter than other luminous galaxies associated with radio galaxies that were known at the time. While searching for the optical counterparts to other radio sources in the Third Cambridge catalogue, many optical plates also showed objects with a similar optical properties but no radio counterpart. This led to the first identification of a class of quasi-stellar galaxies (now called quasars) by Sandage in 1965.

Today we understand that quasars are a subset of a larger class of galaxies which have an Active Galactic Nucleus (AGN). The excess energy in AGN is powered by gas drawn into the deep potential well created by a central super-massive black hole of masses millions to tens of billions times that of the Sun. Almost every massive galaxy has a super-massive black hole at its centre. The

observational characteristics that distinguish AGN from normal galaxies are varied, and can include radio emission, superlatively high luminosities, strong emission lines from ionised gas, detections from compact X-ray sources, and the presence of polarised light. Not every AGN exhibits the same characteristics, and even individual objects may show variability on observable time scales.

AGN can be broadly classed into two categories. The first category is typically referred to as 'high-excitation', 'quasar-mode', 'radiative-mode', or 'strong-lined' and these objects are governed by what is called cold-mode accretion. In this accretion mode the AGN activity is fuelled by a large central repository of cold gas (.e.g, Larson, 2010). A depiction of this type of AGN is shown in Figure 1.3. The super-massive black hole is thought to be surrounded by an accretion disk which produces optical through ultraviolet thermal emission in a region only a few parsecs across, giving rise to the compact 'quasi-stellar' appearance first noted by Schmidt. A hot corona above the accretion disk produces X-ray radiation via inverse Compton scattering. The strong radiation produced by the optical through X-ray light photoionizes the area directly surrounding the accretion disk. Outside this area is a dusty molecular torus that obscures the radiation from the accretion disk when viewed edge-on, but will re-radiate the absorbed emission in the mid-infrared. Near the accretion disk is gas with velocity dispersions of a few thousand kilometers per second, which produces broad emission lines (the broad line region). Slower, cooler gas that extends well beyond the torus produces narrow emission lines (the narrow line region). Radio jets are only present in a fraction of the sources.

In unification models, the viewing angle towards the AGN results in different observed features (e.g., Barthel, 1989; Antonucci, 1993; Urry & Padovani, 1995). When viewed edge-on the torus will obscure the emission from the accretion disk, causing the optical quasar to be hidden. The broad line region will also be hidden, and only narrow emission lines will be seen. AGN that are tilted so the observer sees inside the torus will be seen as classical optical quasars, and both broad and narrow lines will be present. If a radio jet is present the radio emission may be beamed towards the observer, causing apparent super-luminal motion (Barthel et al., 1989). The high occurrence of beamed radio emission in quasars has led to the wide acceptance of unified models of radio galaxies and quasars (Barthel, 1989).

The second category of AGN are termed 'low-excitation', 'radio-mode', 'radiatively inefficient', or 'weak-lined' AGN. In these objects the fuel source has been argued to be hot gas (e.g., Hardcastle et al., 2007), which is accreted via advection dominated accretion or radiatively inefficient accrection flows (e.g.,

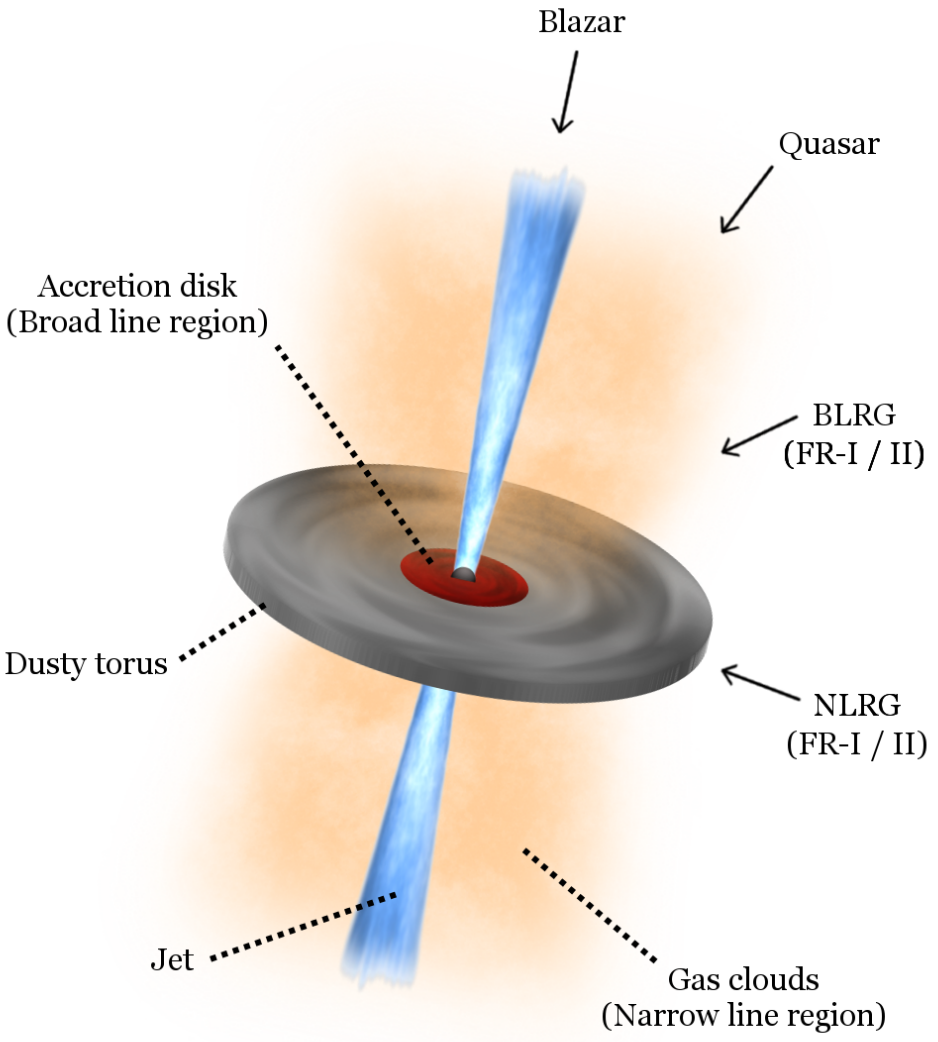

Figure 1.3: A diagram of a radio loud high-excitation AGN. The jet is not present in radio quiet AGN. The arrows indicate the type of object that is seen based on viewing angle. Image credit J. Harwood.

Narayan & Yi, 1994; Quataert, 2001; Ho, 2008). Almost all available energy from accretion is channelled into jets. Low excitation AGN lack the strong emission lines associated with the high-excitation AGN (e.g. Hine & Longair, 1979; Jackson & Rawlings, 1997), and evidence for an obscuring torus is not present (e.g., Whysong & Antonucci, 2004; Ogle et al., 2006). Observed X-ray emission is consistent with jets rather than accretion (Hardcastle et al., 2006; Evans et al., 2006), and the accretion disk is either missing or truncated. The types of galaxies that host low-excitation AGN are typically massive, red galaxies in dense environments (Best et al., 2005b).

Both high-excitation radio galaxies (HERGs) and low-excitation radio galaxies (LERGs) are found in radio surveys. LERGs comprise almost the entire population of low-luminosity radio AGN with powers $\lesssim 10^{25}\,\mathrm{W\,Hz^{-1}}$ at 1.4 GHz in the local Universe, while HERGs begin to dominate the population of radio AGN with powers $> 10^{26}\,\mathrm{W\,Hz^{-1}}$ (Best & Heckman, 2012). This is suggestive of the same type of power division between FR I and FR II sources, but not all HERGs have FR II morphology, and not all LERGs have FR I morphology. Best & Heckman (2012) found that HERGs and LERGs are better separated by their accretion rates, with Eddington accretion rates of 1-10 per cent for HERGs and less than 1 per cent for LERGs.

1.4 Low Frequency Carbon Radio Recombination Lines

1.4.1 The Cold Neutral Medium

The cycle of star formation plays a key part in shaping a galaxy's evolution. The interstellar medium (ISM) provides the fuel to make new stars and is the repository for the ejecta of old stars. The ISM is recycled through many different components, and the main components are summarised in Table 1.1. While many of these components have been well characterised, constraining the physical properties (n_e,T_e) of the cold neutral medium (CNM) has remained challenging. This cold, diffuse phase of the ISM has historically been studied via the spin-flip transition of neutral hydrogen that manifests as emission or absorption at 21 cm (1.4 GHz). Constraining the physical parameters of the CNM via H I observations is difficult, and limited to only certain conditions where additional information to separate the CNM from the warm neutral medium is avaliable (e.g., Heiles & Troland, 2003).

Carbon radio recombination lines (CRRLs) offer another means to observe the CNM. The ionisation potential of carbon is less than that of hydrogen and thus singly-ionised carbon can co-exist with neutral hydrogen. In low temperature and density conditions, electrons can recombine with C^+ to very high quan-

tum levels ($n \gtrsim 300$), producing recombination lines at low radio frequencies ($\nu \lesssim 240\,\mathrm{MHz}$).

1.4.2 Observing Carbon Radio Recombination Lines

CRRLs have been observed in our own Galaxy on scales of degrees along the Galactic plane (e.g., Erickson et al., 1995; Kantharia & Anantharamaiah, 2001), and on smaller scales in the direction of bright background sources such as H II regions (e.g., Golynkin & Konovalenko, 1991), Casseopeia A (e.g., Asgekar et al., 2013; Payne et al., 1989; Konovalenko & Sodin, 1981), and extragalactic sources (Oonk et al., 2014). Only hydrogen recombination lines have been detected at frequencies > 1 GHz in extragalactic sources, all of which are bright, nearby starburst galaxies (e.g., Shaver et al., 1977; Anantharamaiah et al., 1993; Rodriguez-Rico et al., 2004; Roy et al., 2008). These high-frequency extragalactic detections are all most likely associated with H II regions rather than the CNM.

Observing CRRLs at low frequencies has three main advantages. First, their optical depth will be higher which makes detection easier. In particular, the stimulation of the ground state of carbon ($^2\mathrm{P}_{1/2} \rightarrow {}^2\mathrm{P}_{3/2}$) can be coupled with the recombination of an electron to an extremely high quantum level. Second, the number of lines per unit frequency increases with decreasing frequency and wide bandwidth instruments can observe multiple CRRLs simultaneously. Over small enough ranges in frequency, the line profiles will be correlated, and stacking procedures can be used to procure a CRRL detection even when the lines are not detected individually. Even though CRRLs are more closely spaced at lower frequencies, they are intrinsically narrow lines and are unlikely to be blended even at the lowest observable frequencies. Third, low-frequency CRRLs are seen in absorption, opening the possibility of observing the CNM even in bright objects at high redshift (Shaver, 1978).

1.4.3 Theoretical Models

Once detected, comparison of the measured line profiles with detailed theoretical models can constrain the physical properties of the CNM (e.g., Shaver, 1975b; Payne et al., 1989, 1994). CRRLs come from singly ionised carbon with an electron recombining at a very high quantum level. Such a system can be approximated as a Rydberg atom. The optical depth of the CRRLs can be related to the 'departure coefficient' which describes the deviation of the level population from local thermodynamic equilibrium (LTE). Early models were developed for Rydberg atoms which were limited at the time to quantum levels

Table 1.1: General properties of different interstellar medium components (adapted from Cox, 2000).

Phase	State of H	Density [cm^{-3}]	Temperature [K]	Heating	Cooling
Molecular Clouds	H_2	> 100	10-20	Cosmic Rays	CO, FIR
H II Regions	H II	> 100	10^4	Photoionization	[O III], [O II], H recombination
Cold Neutral Medium	H	$0.01-1.0$	$10-300$	Photoelectrons from dust	[C II]
Warm Neutral Medium	H	$0.1-10$	≈ 8000	Photoelectrons from dust	[C II]
Warm Ionised Medium	H II	$0.3-10$	≈ 8000	Photoionization	Hα, [N II], [S II]
Hot Ionised Medium	H II	0.01	$> 10^{5.5}$	Shocks	X-rays

$n \lesssim 500$ (e.g., Seaton, 1964; Dupree, 1969; Shaver, 1975a; Salem & Brocklehurst, 1979; Storey & Hummer, 1991).

A major advancement in the last thirty years was the inclusion of the dielectronic recombination, a process by which the stimulation of the ground state of carbon is coupled with the recombination of an electron to very high quantum levels (e.g., Walmsley & Watson, 1982; Ponomarev & Sorochenko, 1992). Most recently, these models have been updated making use of advances in computing. Salgado et al. (2016a) improved the theoretical models in several ways, including: updated values for the necessary rates used to calculate the level populations; proper treatment of dielectronic recombination by explicitly computing level populations for l quantum levels; and calculations of level populations up to quantum levels up to $n = 10000$. These updated models are necessary to provide sound theoretical predictions for CRRL intensities, which originate in low temperature and low density gas (Salgado et al., 2016b). The theoretical models provide an excellent foundation for future studies of low-frequency CRRLs, and will be used in the coming years to characterise the CNM in the Galaxy as well as extragalactic sources.

1.5 Advances in Low Frequency Radio Astronomy

During the last fifty years, astronomers have pushed to higher frequencies (above 1 GHz) where better resolution and sensitivity were easier to achieve. Recently there has been a resurgence of interest in low-frequency radio astronomy. The upcoming Square Kilomtre Array (SKA; Schilizzi, 2005) will mark a new era for radio astronomy with unprecedented sensitivity at metre to centimetre wavelengths. Its development has led to a rapid growth in antenna design and improvements in interferometer back-ends. Several pathfinder arrays have been constructed, including the Australian SKA Pathfinder (ASKAP; Johnston et al., 2007), the South African SKA precurser MeerKAT (Gibbon et al., 2015). A system of low-frequency dipoles were installed at the primary foci of the Very Large Array (VLA) antennas and used to survey the sky north of -30 degrees declination at 74 MHz (Cohen et al., 2007).

Advances in computing have also allowed for significant improvements without replacing front end hardware. Updated backend instrumentation has transformed the VLA into the Karl G. Jansky VLA (VLA; Perley et al., 2004) with improvements in both its frequency coverage and sensitivity. Computing advances have also allowed for the correlation of signals from hundreds to thousands of individual elements. This has revolutionized low-frequency radio astronomy, and several dipole-array interferometers have been constructed, in-

cluding the Murchison Widefield Array (MWA; Tingay et al., 2013), the Long Wavelength Array (LWA; Taylor, 2007), and the Low Frequency Array (LOFAR; van Haarlem et al., 2013).

LOFAR is a new radio telescope with a revolutionary phased-array design that makes use of electronically pointed dipoles rather than traditional dish telescopes. The simple dipole antennas are grouped into stations. There are 37 stations concentrated in the Netherlands, and 12 stations spread across five other European countries. There are two different types of dipoles in each station. The High Band Array (HBA) operates at $110 - 240$ MHz and consists of thin metal dipoles supported by Styrofoam and protected from the weather. The Low Band Array (LBA) which is the focus of this thesis operates at $10 - 90$ MHz with a sharply peaked response making the array most sensitive around 60 MHz. Each LBA antenna consists of two simple wire dipoles (one for each linear polarisation) attached to the ground and supported at their apex in the center by a plastic pipe. The station locations are shown in Figure 1.4, along with a bird's eye view of a station, and a close up of the LBA dipoles.

The signals from each antenna are converted to digital and then the station is pointed electronically by introducing phase delays in the signal path before station summation. The digital nature of the signals allows multiple beams to be formed simultaneously, limited only by the total bandwidth of the instrument. When combined with its large instantaneous field of view, this makes LOFAR an extremely efficient survey instrument. Up to 96 MHz of bandwidth is available to be divided amongst different beams or concentrated in one beam for increased sensitivity. This bandwidth is divided into subbands, which can be sub-divided into channels of specified widths as small as 767.9 Hz in routine observations (making LOFAR an ideal instrument for observing CRRLs).

Most LOFAR observations use only the stations in the Netherlands, which provide fields of view of tens of square degrees and resolutions of a few arcseconds (HBA) to tens of arcseconds (LBA). The wide geographic distribution of international stations provides LOFAR with an effective collecting area more than a thousand kilometres across, allowing sub-arcsecond resolution to be achieved. This capability sets LOFAR uniquely apart from other low-frequency arrays, and enables exploration of entirely different science topics.

With new technological advances come new challenges. Low frequency radio telescopes operate in a regime where the ionosphere can have a large impact on observations, causing stationary radio sources to appear to move and/or scintillate in an image, directly comparable to the same problems due to seeing in the optical regime. With the wide fields of view afforded by low-frequency tele-

Figure 1.4: *Top:* The locations of LOFAR stations. The data in this thesis were taken before the stations in Poland were constructed, when the longest baseline was between Onsala and Nançay (1292 km). *Middle:* The LOFAR-UK station at Chilbolton. The LBA antennas are in the foreground with the HBA antennas clustered together under a weather-protective covering behind the LBA. *Bottom:* Dipoles from an LBA station within the central core of LOFAR, with the author in the picture for scale.

scopes, the assumption that a single correction is valid for the entire field of view breaks down, and new calibration techniques are necessary.

A substantial amount of progress has been made in calibration techniques since the early days of radio astronomy. From self-calibration on individual sources in small fields of view (e.g., Pearson & Readhead, 1984) to the development of field-based calibration (Cotton et al., 2004) using multiple sources in large fields of view, the scope of calibration techniques has expanded. This is particularly relevant for LOFAR, where the ionosphere, and to a lesser extent imperfect beam models, can cause direction-dependent distortions. Intema (2009,2014) developed the Source Peeling and Atmospheric Modelling (SPAM) technique to deal with ionospheric issues for the Giant Metrewave Radio Telescope, which operates at frequencies from 150 to 610 MHz. The most recent advancements for calibrating LOFAR data to make wide-field images have been SAGECal (Yatawatta et al., 2013; Kazemi et al., 2011) and facet calibration (van Weeren et al., 2016; Williams et al., 2016).

Using the full International LOFAR requires different calibration schemes, as it is challenging to combine signals from geographically isolated stations. Errors in station positions, different station clocks, and errors from propagation through different atmospheric conditions must all be accounted for. The ionosphere dominates the delay (how phase changes with frequency) errors in the low-frequency regime. The delay errors have ν^{-2} dependence on ionospheric conditions, making it even more challenging to calibrate data for the LBA than the HBA. With some modifications the global fringe-fitting algorithm described by Cotton (1995) has been successfully used for LOFAR HBA (Varenius et al., 2015; Moldón et al., 2015; Varenius et al., 2016).

Finally, LOFAR is pushing forward the development of fast algorithms to deal with large volumes of data, in preparation for the Tier 1 survey of the entire Northern sky (north of 0 degrees declination). One major improvement was the implementation of the Statistically Efficient and Fast Calibration (StEfCal; Salvini & Wijnholds, 2014) in the native LOFAR software. The use of Kalman filters is a promising step forward into the next generation of efficient calibration for the unique problems of low-frequency radio astronomy (Smirnov & Tasse, 2015).

1.6 This Thesis

HzRGs are spectacular objects with clear interaction between the radio jets and their host galaxies and environments. The goal of this thesis is to use low frequency radio astronomy tools to help answer the following questions:

- Are HzRGs fundamentally different objects than their low redshift counterparts?
- What are the mechanisms that cause the correlation between radio galaxy spectral index and redshift?
- What is the cold gas content in extragalactic radio sources, and how does it play a part in the cycle of star formation?

In particular, the tools used are catalogues from deep, wide-field LOFAR imaging; the highest resolution images at frequencies less than 100 MHz using the international LOFAR LBA stations; and finally, spectroscopic observations with both LOFAR and the Karl G. Jansky VLA (VLA).

Chapter 2 begins with a catalogue of LOFAR-detected radio sources from Williams et al. (2016). Cross-matching with the AGN and Galaxy Evolution Survey (AGES; Kochanek et al., 2012) multi-wavelength data provides spectroscopic redshifts for 60 radio sources above a power of $10^{25.5}\,\mathrm{W\,Hz^{-1}}$. Optical and near-infrared quasar identifications are used to separate the sample into radio galaxies and quasars. In orientation-only unification schemes, this is the difference between a viewing angle seeing the obscuring torus edge on (radio galaxy) or being able to see the accretion disk inside the torus (quasar). The sizes of the radio jets will be foreshortened in the latter case, and two samples are compared to test whether or not the difference in sizes is due to orientation effects. The quasar sizes are on average smaller than the radio galaxy sizes by a factor of 3.1 ± 1.0 for the LOFAR-detected radio sources, which is evidence for orientation-based unification.

Chapter 3 is a detailed study at 55 MHz of 4C 43.15, one of a sample of 10 high redshift radio galaxies that will be used to examine the spectral index−redshift correlation. This chapter makes use of traditional very long baseline interferometry (VLBI) techniques to make the highest resolution images below 100 MHz, achieving sub-arcsecond resolution with the International LOFAR. When coupled with archival VLA observations, the images of this $z = 2.4$ radio galaxy reveal a bridge of emission between the two FR II radio lobes. The morphology and spectral index properties of 4C 43.15 are similar to those seen in local radio galaxies. The integrated spectra of the radio lobes show a break at frequencies between 55 MHz and 1.4 GHz, with steepening at higher frequencies. This indicates that the original classification as an ultra steep spectrum radio galaxy was dependent on the fixed observing frequencies, which straddled the break in the spectrum.

The observed correlation between radio spectral index and redshift has been successfully used to find high redshift radio galaxies like the one studied in Chapter 3. However the cause of the relation is still unclear. **Chapter 4** investigates whether the relation between spectral index and redshift ($\alpha - z$) can arise simply due to the increased photon energy density of the cosmic microwave background (CMB), which increases as $(1+z)^4$. This causes increased synchrotron losses. This chapter uses a new approach of selecting archival data for ~50 radio galaxies at $z \leq 1$ with enough data for spectral modelling, and simulating radio spectra of radio galaxies at higher redshifts. This allows for the introduction of only the inverse Compton losses to see if this effect alone can reproduce the $\alpha - z$ relation. Observational selection effects are used so the simulated sample can be compared to an observed sample. We find that the observed relation can be entirely reproduced with only the increased synchrotron losses due to inverse Compton scattering of photons from the CMB at high redshift, without having to invoke any intrinsic α-power relationship or environmental effects.

Chapter 5 presents the first detection of extragalactic CRRLs, in nearby starburst galaxy M82. Starburst galaxies are undergoing intense, short-lived periods of star formation with star formation rates up to tens to hundreds of solar masses per year. Normal galaxies maintain star formation rates of $1-5$ solar masses per year. Starburst events are often found in disturbed galaxies where there is evidence of a merger. The M82 starburst was likely triggered by an interaction with M81 (Yun et al., 1993). The 8.5σ detection is achieved by stacking 22 α transitions ($\Delta n = 1$) in the range of 50−64 MHz using LOFAR LBA observations. The CRRLs are detected in absorption, and should be detectable if present in high redshift radio galaxies with similar flux densities. The line profile has a peak optical depth of 3×10^{-3} and a full width half maximum of $31\,\mathrm{km\,s^{-1}}$. The narrow line width suggests that the line is localized to a small region of M82, as other gas tracers like CO show widths of $\sim 200\,\mathrm{km\,s^{-1}}$. The centroid velocity suggests that the line is associated with the nuclear region. The line profile suggests that the CRRL originating gas is associated with the cold atomic gas in the direction of the nuclear region.

The CRRL detection described in Chapter 5 is not enough to constrain the models of gas temperature and density, and in **Chapter 6** spectroscopic observations with the VLA P-band are used to rectify this. The CRRLs in this frequency range (250−480 MHz) are expected to be in emission. We find a meaningful upper limit to the optical depth, and constrain the gas temperature and density using the previous detection and this new upper limit. We find that the gas tem-

perature and density are $T_e = 95^{+105}_{-85}$ K and $n_e = 0.030 \pm 0.005\,\mathrm{cm}^{-3}$. These gas temperatures are consistent with Galactic values for the cold neutral medium. We estimate an upper limit on the C II/H I ratio of 1.05×10^{-3}.

Chapter 7 describes the calculation of bound-bound Gaunt factors for quantum levels up to $n = 2000$. These factors are used to calculate oscillator strengths, one of the necessary quantities in the updated theoretical models of CRRLs Salgado et al. (2016a,b). A review is presented of various calculation methods, with particular attention given to the computational problems that led previous authors to use approximations with errors up to ~8 per cent. These new calculations have a relative error of 3×10^{-3} when compared with more detailed calculations for low quantum numbers using relativistic corrections. The values are useful for a wide range of physical applications, and are tabulated and published online.

The **Appendices** describe LOFAR commissioning work in support of this thesis, in particular Chapter 3. Appendix A covers simulations showing that bright, off-axis sources can have a large impact on baselines to International LOFAR stations. This is due to a lack of high-resolution models of these bright sources, which are necessary to remove their effects from the data. Appendix B describes challenges faced and their resolution when using the 'Station Adder' algorithm used to combine visibilities on particular baselines in Chapter 4. An additional improvement of ~1 per cent in the image noise was found to be be achieved when using the weighted geometric average of data coordinates, and this improvement was added to the LOFAR *new default pre-processing pipeline* (NDPPP) software.

1.7 The Future is Bright at Low Frequencies

Low-frequency radio astronomy is a rapidly growing field. Even when new instruments like the SKA are fully operational, LOFAR will remain a unique and powerful instrument. In particular, there is no planned instrument that will match the frequency coverage of the LBA (10–90 MHz) and the exquisite subarcsecond resolution achievable by using International LOFAR.

Chapter 4 laid out the method for using VLBI techniques at frequencies ~60 MHz. This provides one data point for one source; the next step is to apply this method to observations of other HzRGs. VLBI observations with the HBA will provide another measurement at frequencies around 150 MHz, which is critical to anchor spectral fitting to determine properties of HzRGs. It will be particularly interesting to determine the spectral ages and how they evolve along the jet axes, and to determine the particle acceleration mechanisms present

where the jets terminate. A sample of 10 sources is enough to identify trends for the larger population of HzRGs, which will guide future studies.

The potential to probe the CNM in HzRGs is also thrilling. The detection of CRRLs in Chapter 5 shows that this can be done. HzRGs are known to contain extended gas in several phases (Miley & De Breuck, 2008), and are ideal candidates for CRRL searches. Detections would provide a unique tracer for of the cold gas in HzRGs.

There are many other science cases that become possible with the high resolution capabilities of LOFAR. The physics of hot-spots in FR II radio galaxies can be studied in exquisite detail. High resolution images of radio sources will allow star-forming galaxies and AGN to be distinguished on the basis of morphology. Populations of radio-loud AGN with resolved jets can be studied out to redshifts of $\sim$2 with the LOFAR Tier 1 survey depths, to see if their evolution evolves with time and/or environment.

One of the most compelling advantages of LOFAR is its survey efficiency. The LOFAR Tier 1 Survey will nicely fill in the $P-z$ diagram for radio galaxies and quasars, providing robust statistics to disentangle orientation effects from physical properties of radio-loud AGN and quasars. This requires supporting spectroscopic redshifts and host galaxy classification, which will be accomplished over the next few years for hundreds of thousands of LOFAR-detected sources using the William Herschel Telescope Enhanced Area Velocity Explorer (WEAVE). The combination of LOFAR data with optical information will provide a powerful tool that will have a lasting impact on the field of galaxy evolution.

CHAPTER 2

Investigating the Unification of LOFAR-detected Sources in the Boötes Field

"There are some oddities in the perspective with which we see the world. The fact that we live at the bottom of a deep gravity well, on the surface of a gas-covered planet going around a nuclear fireball 90 million miles away and think this to be normal is obviously some indication of how skewed our perspective tends to be."
−Douglas Adams−

Low radio frequency surveys are important for testing unified models of radio-loud quasars and radio galaxies. The steep-spectrum isotropic radio emission of these sources allows for orientation-free sample selection at low radio frequencies. Sources similar in size but differently oriented will show different projected linear sizes, and measuring these projected sizes gives the orientation of a source with respect to the line of sight. We use a new radio survey of the Boötes field at 150 MHz made with the Low Frequency Array (LOFAR) to select a sample of radio sources, and identify radio galaxies and quasars using cross-matched multi-wavelength information from the AGN and Galaxy Evolution Survey (AGES), which also provides spectroscopic redshifts. Within the LOFAR sample we find that radio sources with steep spectra have projected linear sizes that are on average 4.4 ± 1.4 times larger than those with flat spectra. We also find that the projected linear sizes of radio galaxies are on average 3.1 ± 1.0 times larger than those of quasars. We combine these results with two previous surveys and find that the linear size of sources is dependent on redshift but not on power. We also find that the linear size ratio of radio galaxies to quasars does not evolve with either redshift or power. The quasar fraction at low redshifts is ~ 0.2 and is positively correlated with the linear size ratio at higher redshifts. We conclude that the data are consistent with an orientation-based unification scheme.

Morabito, L. K., Williams, W. L., Saxena, A., Duncan, K., Röttgering, H. J. A., et al.
In preparation

2.1 Introduction

Active galactic nuclei (AGN) produce high nuclear luminosities that cannot be explained by star formation alone. They are believed to be powered by central super-massive black holes. AGN can exhibit a wide variety of observational characteristics, including high luminosities in the optical and near-IR, strong emission lines from ionised gas, and high mid-IR luminosities. AGN which have strong emission lines in their spectra are classified as Type 1 or Type 2 based on the emission line properties. Type 1 AGN show broad and narrow emission lines while Type 2 AGN show only narrow emission lines.

Under the current unification paradigm (Antonucci, 1993; Urry & Padovani, 1995) Type 1 and Type 2 AGN exhibit different observed characteristics due to the presence of a dusty structure or torus that will obscure the accretion disk and broad line region depending on viewing angle to the AGN. Those AGN which exhibit broad emission lines are associated with bright optical point sources, leading to the term 'quasi-stellar object' or quasar. Type 1 AGN are oriented such that the optical quasar and broad line emission regions are seen directly without obscuration from the torus. Type 2 AGN are oriented such that the broad line emission region and optical quasar are obscured by the dusty torus, and not directly visible.

About 10 per cent of AGN exhibit extended powerful radio emission in the form of jets that extend far beyond the host galaxy and can provide an indication of orientation. Low radio frequency surveys are important for selecting these objects in an orientation-independent way, as high-frequency surveys are biased towards core-dominant objects where the jets are pointed towards the observer.

Radio-loud AGN comprise two populations, believed to be powered by different accretion methods. Radio galaxies that exhibit strong emission lines in the optical regime are referred to as high-excitation radio galaxies (HERGs). HERGs can be either Type 1 or Type 2 AGN. The AGN in HERGs are thought to be powered via a geometrically thin and optically thick accretion disk (Shakura & Sunyaev, 1973). The accretion disk is believed to be fed by large central repositories of cold gas (e.g., Larson, 2010), which has led to the name 'cold-mode' accretion (Best et al., 2005b).

The second type of radio-loud AGN lack the strong emission lines seen in HERGs, and are thus termed low-excitation radio galaxies (LERGs). They also lack evidence for a dusty torus in their infrared emission (e.g., Tasse et al., 2008; Ogle et al., 2006; Whysong & Antonucci, 2004), as well as evidence for a full accretion disk (e.g., Hardcastle et al., 2006; Evans et al., 2006). LERGs are thought to be powered by 'hot-mode' accretion processes, where hot gas is

accreted via advection-dominated accretion or radiatively inefficient accretion flows (e.g., Narayan & Yi, 1994; Quataert, 2001; Ho, 2008). For these reasons the non-radio spectral energy distributions of LERGs are not expected to show strong orientation effects. Best & Heckman (2012) showed that LERGs dominate the population of low-power ($P_{1.4\mathrm{GHz}} \lesssim 10^{25}\,\mathrm{W\,Hz^{-1}}$) sources at least in the local universe, and tend to be associated with edge-dimmed radio jets of Fanaroff-Riley Class I objects (FRI; Fanaroff & Riley, 1974).

The discovery of super-luminal motion in radio jets was strong evidence that some radio sources have their jets aligned close (within ~ 15 degrees) to the line of sight (Barthel et al., 1989). Radio sources with beamed flat-spectrum cores consistent with super-luminal motion should have smaller projected sizes on average than steep-spectrum radio sources with jets oriented further from the line of sight. For HERGs this scenario can be related to the difference between radio galaxies and quasars to the obscuring torus being viewed edge on in radio galaxies, hiding the optical quasar emission. Radio galaxies will therefore have radio jets preferentially oriented closer to the plane of the sky, while quasars will have radio jets closer to the line of sight.

Barthel (1989) used the 3CRR survey of radio sources at 178 MHz (Laing et al., 1983) to study the projected linear sizes for 42 radio sources with optical identifications for $0.5 \leq z \leq 1$. Barthel found that there was a division between radio sources: those associated with quasars were on average 2.2 times smaller than the other radio sources. The 3CRR sample is now 100 per cent spectroscopically complete, and classifications based on emission line ratios have been used to identify HERGs (which are expected to show orientation effects) and LERGs (which are not expected to show orientation effects). The high limiting flux density of the survey means that only 13 per cent have been found to be LERGs (Willott et al., 1999), and are therefore were not a large contaminant in studies previous to this classification.

Follow up studies have tended to confuse the issue. A reassessment of the 3CRR sample found systematically larger sizes of radio-loud AGN (hereafter radio galaxies) compared to radio-loud quasars only for redshifts above 0.5. For lower redshifts, radio galaxies were on average larger than radio-loud quasars but only when their cumulative linear sizes were above $\lesssim 400$ kpc Singal (2014). Singal & Singh (2013) also studied the linear sizes of a 98 per cent spectroscopically complete sample selected at 408 MHz (Best et al., 1999), finding that only at redshifts larger than 1 were the linear sizes of radio galaxies systematically larger than those of quasars. The authors made no attempt to remove LERGs from the sample, but argued that they would have to be a large part of the sam-

ple to change the results. However these studies still only cover a small part of the power−redshift ($P-z$) diagram, and it is important to collect more information to investigate this further.

In this study we use a new low frequency radio survey of the Boötes field (Williams et al., 2016) with the Low Frequency Array (LOFAR; van Haarlem et al., 2013) to investigate the unification of radio sources in two ways. First, we look at the difference in projected linear sizes of flat- and steep-spectrum sources, without any classification from other wavelengths. Second, we investigate the difference in projected linear sizes of cold-mode accretion sources by splitting our sample of HERGs into *quasars* and *radio galaxies* using available multi-wavelength data including spectroscopic redshifts and quasar classifications from the AGN and Galaxy Evolution Survey (AGES; Kochanek et al., 2012). It is difficult to measure properly the sizes of edge-dimmed FR I sources, and we make a power cut at $P_{150\mathrm{MHz}} > 10^{25.5}\,\mathrm{W\,Hz^{-1}}$ to exclude these sources as well as star-forming galaxies at lower powers (Saxena et al., in preparation). This means our sample is likely to be dominated by HERGs, although it is difficult to determine this based on broad-band photometry alone (Janssen et al., in preparation).

The new LOFAR catalogue contains over 6,000 radio sources to an rms depth of $\sim 120-150\,\mu\mathrm{Jy\ beam^{-1}}$ at 150 MHz. While previous samples used to test orientation-based unification probed high luminosity sources over large areas of the sky, the deep LOFAR data probes a large number of fainter sources over a smaller area. This adds a substantial number of sources to the P−z diagram at lower powers across all redshifts.

Section 2.2 first describes the LOFAR survey, the multi-wavelength data, and the selection of quasars and radio galaxies. Results from the LOFAR survey are presented in Section 2.3. The LOFAR results combined with two previous samples are presented in Section 2.4. Discussion and conclusions follow in Sections 2.5 and 2.6. Throughout the paper we assume a ΛCDM concordance cosmology with $H_0 = 67.8\ \mathrm{km\,s^{-1}\,Mpc^{-1}}$, $\Omega_\mathrm{m} = 0.308$, and $\Omega_\Lambda = 0.692$, consistent with Planck Collaboration et al. (2015). Spectral index is defined as α with flux density $S \propto \nu^\alpha$.

2.2 The Boötes Field Data

In this section, we first present the pre-existing multi-wavelength data, the new LOFAR Boötes survey, and then the cross-matching of the radio and multi-wavelength data and measurement of angular radio sizes.

2.2.1 AGES: Multi-wavelength Data

The NOAO Deep Wide-Field Survey (NDWFS; Jannuzi & Dey, 1999) covers 9 deg square of the Boötes field with deep optical to near-infrared data (B_W, R, I, J, K). Ancillary data at longer wavelengths covers the near to mid-infrared (IRAC 3.6, 4.5, 5.8, and 8.0μm, and MIPS 24μm). Kochanek et al. (2012) used the combination of all 10 bands and complementary ultraviolet, radio, and X-ray data to construct a well defined sample of galaxies and AGN for a targeted spectroscopic survey. This AGN and Galaxy Evolution Survey (AGES) covers 7.7 deg square of the Boötes field and provides spectroscopic redshifts for 18,163 galaxies (to I =20 mag) and 4,764 AGN candidates (to I =22.5 mag) measured with the Hectospec instrument on the MMT. The NDWFS contains more than 2 million optical sources, and Kochanek et al. (2012) aimed to provide a complete sample of AGN and a statistically robust (via random sparse sampling) sample of normal galaxies. For this paper we are interested only in the AGN sample.

All AGN candidates in Kochanek et al. (2012, hereafter K12) were targeted for spectroscopic observations. From 8977 AGN candidates, spectra were taken for 7102 and redshifts obtained for 4764 (after excluding Galactic stars, which made up 9 per cent of successful redshifts). Spectroscopic information is therefore available for $\sim$ 53 per cent of AGN in AGES. For the sources with spectroscopic information, K12 also provide five different AGN classifications that rely on different bands of the multi-wavelength data (described in detail in K12). AGN can be selected based on compact, bright optical morphology, complex near-IR selections (based on Stern et al., 2005), bright mid-IR luminosities, the presence of X-ray point sources, and radio detections at 1.4 GHz.

To divide the LOFAR-detected sources into quasars and radio galaxies, we identify quasars as those objects satisfying the optical and/or mid-IR colour criteria (in line with above), and the rest of our sample is therefore defined as radio galaxies. We check that all of the radio galaxies satisfy the mid-IR 24 μm criteria (as above), which indicates the presence of a dusty torus (and these sources are therefore not likely to be LERGs).

2.2.2 AGES/LOFAR sample completeness

We wish to determine if the results of this study will be biased by only using sources with spectroscopic information. To do this we examine the radio angular size and redshift distributions for the 1433 sources which have $I \leq 22.5$. We compare the distributions for sources with spectroscopic redshifts (from AGES) and sources which have photometric redshifts (from Duncan et al., in preparation). These are shown in Fig. 2.1. Overall, the histograms have similar distribu-

tions, except for an excess in the photometric redshift distribution for $1.4 \lesssim z \lesssim 2$ ($0.15 \lesssim \log(1+z) \lesssim 0.3$. Examining the distributions of spectroscopic redshifts for radio galaxies and qausars shows that the two populations have similar distributions. The discrepancy between spectroscopic and photometric redshifts must therefore come from the other cross-matched galaxies in the sample, which are generally at lower powers and excluded from our analysis. This indicates that our results will not be biased towards certain spectral types by limiting the sample to only sources with spectroscopic redshifts.

We find that the distributions of the radio angular size, which is the parameter we are interested in for this study, are quite similar (see right panel of Fig. 2.1). We thus conclude that we are not missing populations of systematically smaller or larger objects, and do not expect our results to change if the sample were expanded.

2.2.3 LOFAR Boötes Survey

The catalogue from Williams et al. (2016) contains a total of 6,275 radio sources within 19 deg^2. The rms varies over the field of view, and sources with peak fluxes exceeding a threshold of 5σ above the local rms were included in the final catalogue. The rms is less than $120\,\mu$Jy beam^{-1} at the centre and more than 50 per cent of the field of view has rms noise less than $180\,\mu$Jy beam^{-1}. The average rms noise at the edges of the optical coverage is approximately $150\,\mu$Jy beam^{-1}. The resolution of the LOFAR image is 5.6×7.4 arcsec, with average positional accuracy of ~0.4 arcsec.

The sources in the catalogue are divided into classes based on radio morphology. Here we consider only single sources or extended sources with a radio core (VClass 1/11) and double sources with no obvious radio core (VClass 2/21). These will be mostly FR II, FR I, or unresolved sources. We make a power cut at $10^{25.5}\,\mathrm{W\,Hz^{-1}}$ to exclude lower power sources which are either star forming galaxies or more likely to have FR I morphology. Since FR I sources are dimmer at the edges, their linear sizes are not well defined. The other morphological classifications only make up 0.1 per cent of the catalogue, and are either diffuse or complex, and not expected to be the radio sources in which we are interested.

Radio Luminosity Functions

We compare the radio luminosity functions (RLFs) for our sample with model RLFs from Rigby et al. (2011). The observed RLF for the LOFAR sample with $P_{150} \geq 10^{25.5}\,\mathrm{W\,Hz^{-1}}$ has similar behaviour to the model RLF, i.e. the trends in space density are the same, suggesting that the sample is representative of the

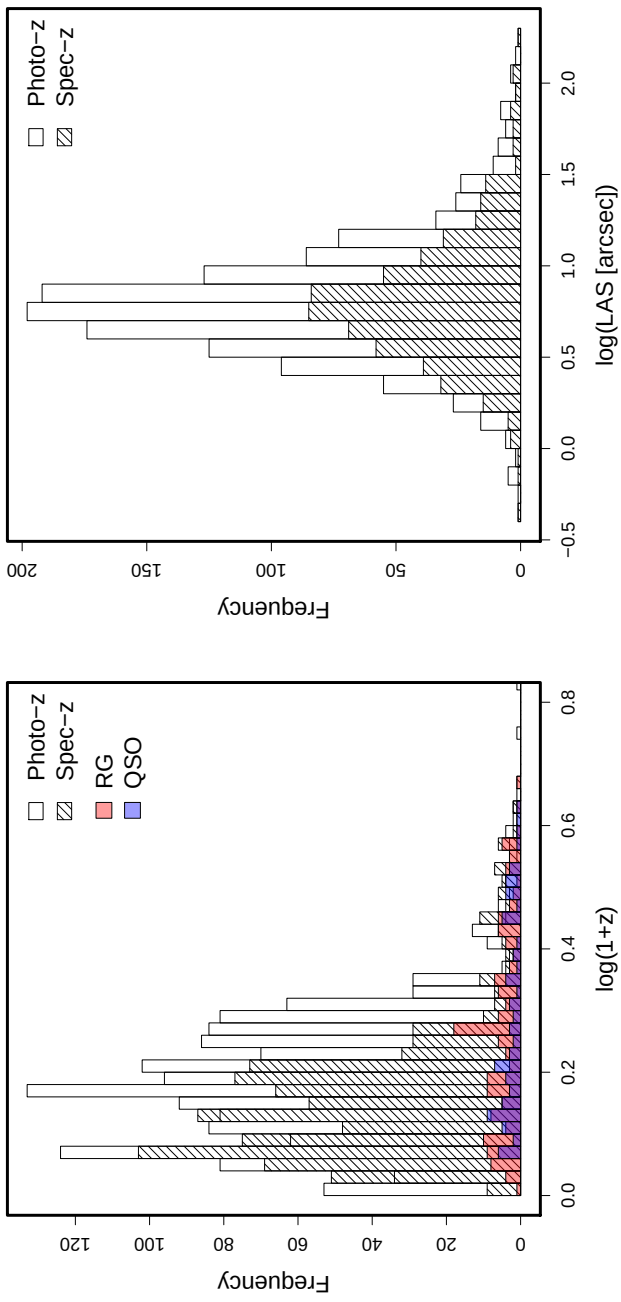

Figure 2.1: Comparison of redshift and radio angular size distributions for AGN from AGES which have $I \leq 22.5$ and LOFAR-detected radio emission. *Left:* Distribution of redshifts for sources with photometric redshifts (unfilled histogram) and spectroscopic redshifts (hatched histogram). *Right:* Distribution of radio largest angular size (LAS) for sources with photometric redshifts (unfilled histogram) and spectroscopic redshifts (hatched histogram).

entire population. Introducing higher power cuts in the LOFAR sample changes the RLF, and the space density of radio sources in the LOFAR sample drops off sharply above $z = 2$. We therefore do not consider higher power cuts in this analysis.

Cross-Matching and Measuring Sizes

Within the AGES footprint there are 3584 LOFAR detected sources. From a catalogue built from NDWFS multi-wavelength data (Brown et al., 2007, 2008), Williams (2015) identified 3106 galaxies to be associated with the radio sources. We cross-matched the optical positions of these galaxies with sources in the AGES catalogue within $1''$using TOPCAT (Taylor, 2005) and found 1106 sources with spectroscopic redshifts.

There are 60 sources with spectroscopic redshifts and $P_{150} \geq 10^{25.5}\,\mathrm{W\,Hz^{-1}}$. The angular sizes of these 60 sources were measured as the diameter of the smallest circle enclosing the source at a level of 5σ above the local rms. The centre of the circle may not correspond to the optical source. The size bent sources may be underestimated since we do not measure along the jets. As this fraction is small, this will have a negligible impact on the overall trends.

2.3 LOFAR Results

In this section we present the results for the LOFAR sample. First we investigate the linear sizes of flat and steep-spectrum radio sources, without any further knowledge of the type of host galaxy. We then investigate whether the linear sizes of quasars and radio galaxies, as identified from the multi-wavelength data, are different. This equates to a test of unification through orientation of HERGs, which are powered by cold-mode accretion. In all cases we use only the 60 sources with $P_{150} \geq 10^{25.5}\,\mathrm{W\,Hz^{-1}}$.

2.3.1 Flat vs. steep-spectrum Sources

First we test whether there is a systematic difference in projected linear sizes of flat- and steep-spectrum sources. Using the complementary 1.4 GHz data from a deep Westerbork survey of the Boötes field (de Vries et al., 2002), we calculated the spectral index between 150 MHz and 1.4 GHz and found 11 flat-spectrum objects with $\alpha > -0.5$ (18 per cent). Fig. 2.2 shows the cumulative linear sizes of the flat and steep-spectrum objects and the distribution of sources in the $P - z$ plane. The average redshifts of the two types of sources are $\bar{z} = 1.23$ for the steep-spectrum sources and $\bar{z} = 1.81$ for the flat-spectrum sources. The

difference in angular distance D_A at these two redshifts could make one group of sources appear systematically larger or smaller, so we use the ratio of $D_A(z = 1.81)/D_A(z = 1.23) = 1.01$ to correct the sizes of the steep-spectrum sources so they are comparable to those of the flat-spectrum sources. The projected linear sizes of steep-spectrum sources are on average 4.4±1.4 times larger than those of the flat-spectrum sources.

2.3.2 Quasars vs. Radio Galaxies

Next we test whether there is a systematic difference in the projected linear sizes of radio galaxies and quasars. We identify the quasars and radio galaxies using the AGES criteria as described in Section 2.2.1. The final sample has 44 radio galaxies and 16 quasars above a power cut of $10^{25.5}\,\mathrm{W\,Hz^{-1}}$, with average redshifts of $z = 1.16$ and $z = 1.84$. The cumulative linear sizes and distribution in the $P - z$ plane are shown in Fig. 2.3. The linear sizes of the radio galaxies are corrected for the ratio of $D_A(z = 1.84)/D_A(z = 1.16)$ so the sizes of one sample will not appear systematically larger or smaller. The radio galaxies have projected linear sizes that are 3.1±1.0 times larger than those of quasars.

2.4 Comparison with Previous Samples

In this section we first describe two previous samples that have been used to test the unification of radio galaxies and quasars. We then take these two samples and the new LOFAR sample and divide each into two redshift bins to study the properties of the projected linear sizes of radio galaxies and quasars using all available data.

2.4.1 3CRR Sample

Barthel (1989) used the 3CRR catalogue (Laing et al., 1983) to show the smaller cumulative linear sizes of quasars when compared to radio galaxies within the redshift range $0.5 < z < 1$. Since then, much more detailed optical information has become available. The 3CRR sample is now 100 per cent spectroscopically complete. In addition, near infrared spectroscopy allowed for the identification of HERGs and LERGs, using the equivalent width of [O III] and the ratio of [O II]/[O III] (Willott et al., 1999; Grimes et al., 2004). We use the sample from Willott et al. (1999)[1], which has HERG and LERG classifications as well as spectroscopic redshifts and largest angular sizes. We remove LERGs from the sample. The final number of sources is 170, of which 111 are radio galaxies and

[1] Available at http://astroherzberg.org/people/chris-willott/research/3crr/

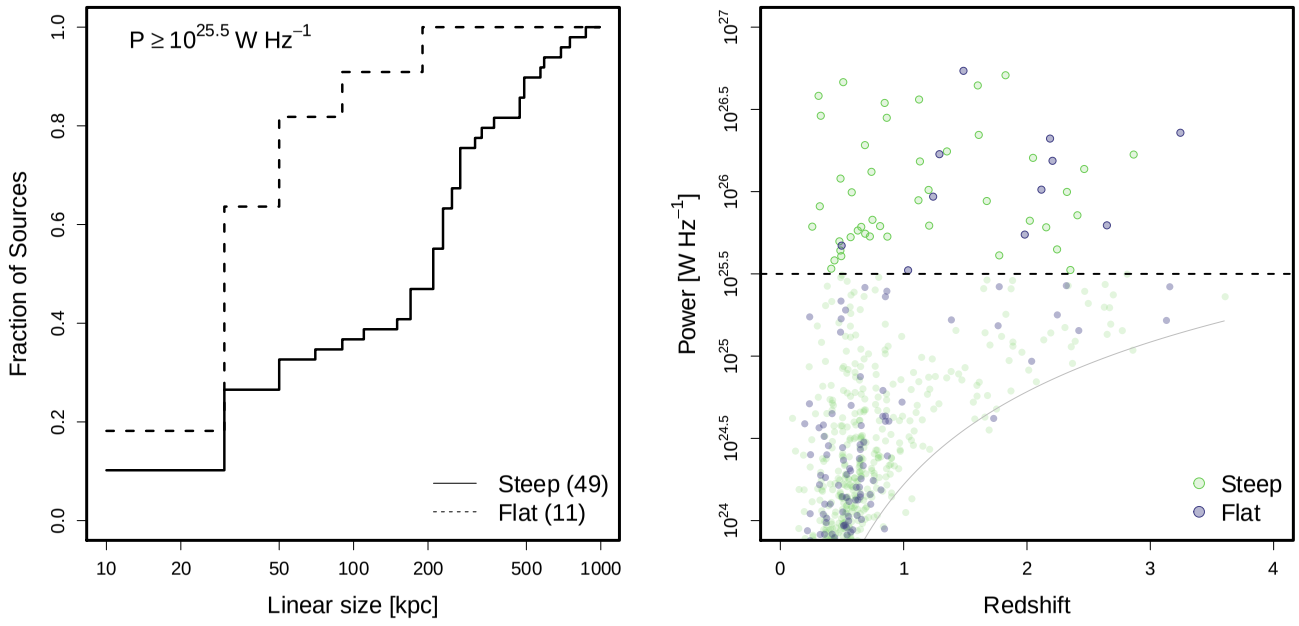

Figure 2.2: *Left:* Cumulative linear sizes for flat-spectrum and steep-spectrum radio sources are shown by the solid and dashed lines, respectively. The number of sources in each sample is indicated in parentheses in the legends. *Right:* The $P-z$ diagram. The horizontal dashed line indicates the power cut of $10^{25.5}\,\mathrm{W\,Hz^{-1}}$. The light gray line shows the flux limit for the survey.

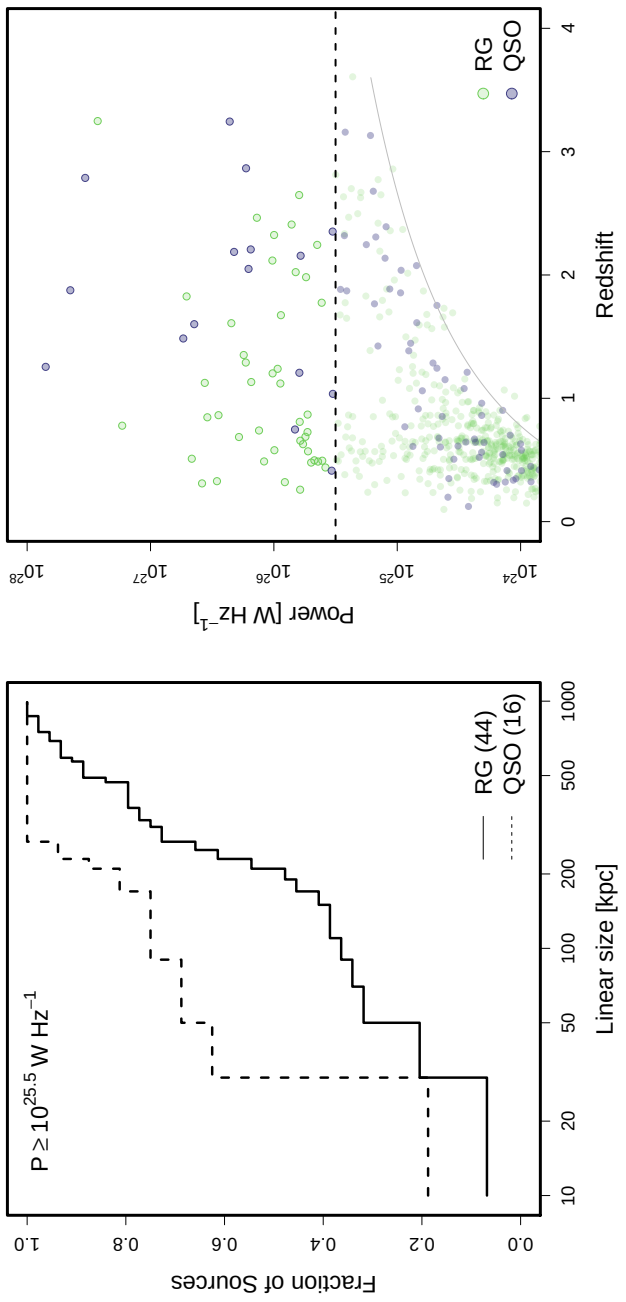

Figure 2.3: *Left:* Cumulative linear sizes for radio galaxies (RG) and quasars (QSO) are shown by the solid and dashed lines, respectively. The number of sources in each sample is indicated in parentheses in the legends. *Right:* The $P - z$ diagram. The horizontal dashed line indicates the power cut of $10^{25.5}\,\mathrm{W\,Hz^{-1}}$. The light gray line shows the flux limit for the survey.

59 are quasars. The mean redshifts are $z = 0.49$ for radio galaxies and $z = 0.82$ for quasars.

2.4.2 Molonglo Radio Catalogue Sample

We use Molonglo Radio Catalogue (MRC) 1 Jy Radio Source Survey (Kapahi et al., 1998a), and a complete quasar subset (Kapahi et al., 1998b; Baker et al., 1999). For this sample there are 349 object which have spectroscopic redshifts and measured angular sizes. This sample does not provide HERG/LERG identification, and the inclusion of LERGs may add radio sources with random orientation (i.e., not preferentially in the sky) to the sample. Since LERGs either lack or have a truncated accretion disk, they are less likely to be classified as quasars and therefore will slightly decreasing the average sizes of radio galaxies. There are 264 radio galaxies and 88 quasars. The radio galaxies have a mean redshift of $z = 0.75$ and the quasars have a mean redshift of $z = 1.13$. The average size of radio galaxies for the complete MRC sample is only 145 kpc, which is notably lower than the average radio size of sources in the LOFAR or 3CRR sample, and even smaller than the average size of quasars in the entire MRC sample.

2.4.3 Results

Each sample covers a different portion of the $P - z$ plane and we treat them separately, dividing each sample into low and high redshift bins. We determined the dividing redshift for each sample such that about half of the sample lies in each redshift bin, but without letting the number of quasars drop below 5 in a bin. The dividing redshifts used were: $z = 1.5$ (LOFAR), $z = 1$ (MRC), and $z = 0.5$ (3CRR). In each bin, we count the number of radio galaxies and quasars, and measure the mean values of power, redshift, and linear sizes for each type of source. These are listed in Tab. 2.1. We use the linear sizes to calculate the ratio of projected linear sizes of radio galaxies to quasars. The number of total sources in a bin and the number of quasars in that bin are used to calculate the quasar fraction. The uncertainties were determined via standard error propagation methods, except for the case of the quasar fractions for the LOFAR sample, where we used small-number counting uncertainties following the prescription in Gehrels (1986). We assume that the error in spectroscopic redshift is negligible compared to the other measurement errors, and set this to zero.

We first examine the measured properties of radio galaxies and quasars by looking at how their linear sizes correlate with both power and redshift. This is shown in Fig. 2.5. There is no clear correlation between linear size and power.

Table 2.1: A summary of the different radio samples. The first line for each sample shows the parameters for the entire sample.

		Radio galaxies					Quasars		
	z range	No.	Mean z	Mean Linear Size [kpc]	D_A Correction	Corrected Linear Size [kpc]	No.	Mean z	Mean Linear Size [kpc]
LOFAR	≤ 3.25	44	1.16	228	1.02	233	16	1.84	76
	$0 < z \leq 1.5$	31	0.73	332	1.00	333	6	1.02	116
	$1.5 < z$	13	2.18	72	1.00	72	10	2.33	52
3CRR	≤ 2.01	111	0.49	300	1.25	375	59	0.82	196
	$0 < z \leq 0.5$	67	0.17	570	1.06	603	18	0.23	320
	$0.5 < z$	44	0.99	228	1.06	241	41	1.08	141
MRC	≤ 3.16	264	0.78	145	1.10	160	88	1.13	180
	$0 < z \leq 1$	199	0.43	223	1.02	227	48	0.66	242
	$1 < z$	65	1.73	86	1.02	88	40	1.69	105

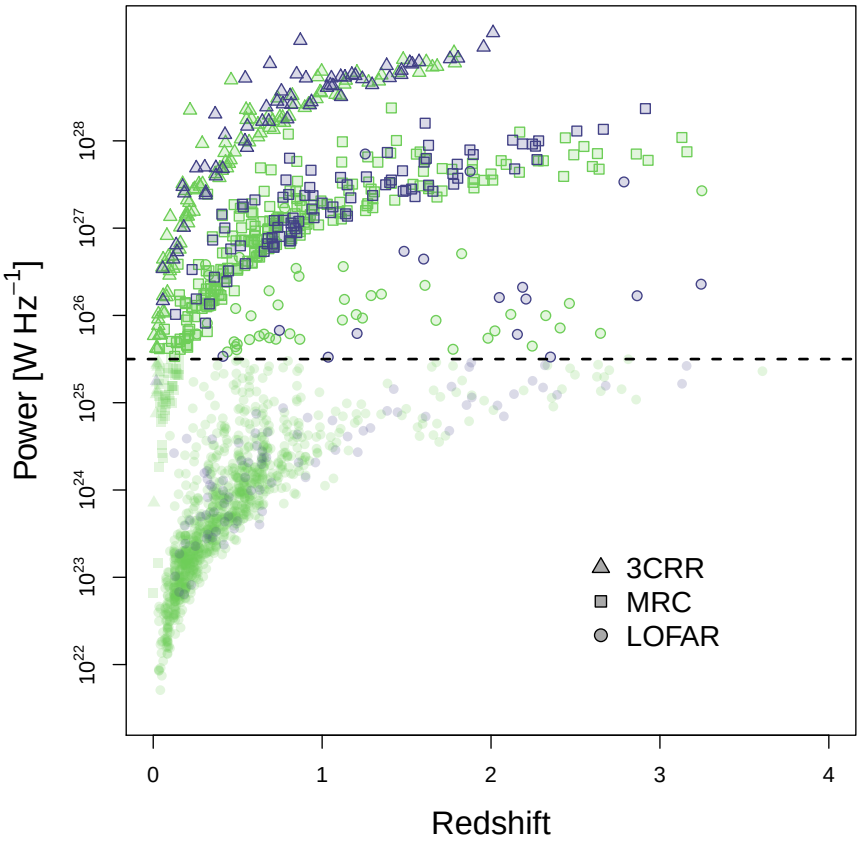

Figure 2.4: Power vs. redshift for the two samples described in this section plus the LOFAR sample. Only sources with spectroscopic redshifts are used, and above powers of $P_{150} > 10^{25.5}\,\mathrm{W\,Hz^{-1}}$ at 150 MHz. Spectral index information was used to convert measured power to P_{150} for the MRC and 3CRR samples. Green points represent radio galaxies and purple points represent quasars.

There does appear to be a correlation between linear size and redshift, with smaller objects found at higher redshifts. The anti-correlation of angular size with redshift is consistent with previous studies (Ker et al., 2012; Neeser et al., 1995; Wardle & Miley, 1974; Miley, 1968) which also find more compact radio sources at higher redshifts.

To quantify the dependence of size on redshift we use the same Partial-rank analysis as described in Section 2.3 of Neeser et al. (1995). Assuming a functional form of size $D \propto (1+z)^{-n}$ where n is the 'evolution strength,' we let n vary in steps of 0.001 over the range $0 \leq n \leq 3$. For each value of n we multiplied the source sizes by $(1+z)^n$ and calculated the Partial-rank statistic for D, z given P. The value of n that produced a statistic of 0 was taken as the evolution strength, and the upper and lower errors correspond to where the statistic was ± 1. We find evolution strengths of $n = 1.988^{+0.252}_{-0.270}$ for all radio galaxies and quasars considered together, $n = 2.051^{+0.391}_{-0.436}$ for radio galaxies, and $n = 1.773^{+0.288}_{-0.275}$ for quasars. These values all agree within the uncertainties, indicating that quasars and radio galaxies have the same evolution strength. The values are also in excellent agreement with Neeser et al. (1995), who find an evolution strength for galaxies and quasars of $n = 1.71^{+0.40}_{-0.48}$ for a flat universe.

We repeat the same exercise but looking at the Partial-rank statistic for D, P given z. Using the functional form $D \propto P^m$, we multiply the sources sizes by P^{-m} and vary m in steps of 5×10^{-5} from -1 to 1. The values of m that produce statistics of 0 are consistent with $m = 0$ for all samples. Specifically, for all sources we find $m = (1.5^{+3}_{-1.5}) \times 10^{-4}$, for radio galaxies we find $m = (2^{+2.5}_{-2}) \times 10^{-4}$, and for quasars we find $m = (5 \pm 5) \times 10^{-5}$. We therefore conclude that there is no intrinsic relationship between power and size.

We next investigate how the ratio between radio galaxy and quasar linear sizes evolves with power and with redshift, see Fig. 2.6. The 3CRR and LOFAR samples show size ratios larger than unity: the 3CRR sample has size ratios of 1.89 ± 0.41 (low z) and 1.71 ± 0.34 (high z) and the LOFAR sample has size ratios of 2.88 ± 0.97 (low z) and 1.38 ± 0.81 (high z). The MRC sample shows size ratios consistent with unity, with 0.93 ± 0.15 (low z) and 0.84 ± 0.21 (high z). There is no clear trend with either redshift or power. This indicates that the linear size ratio remains the same for a large range of powers and out to higher redshifts. The fact that the linear size ratio does not clearly evolve with either power or redshift implies that the populations of radio galaxies and quasars *always* have the same relative sizes.

Finally we investigate how the quasar fraction depends on the radio galaxy to quasar linear size length ratio. The results are shown in Fig. 2.7. There are

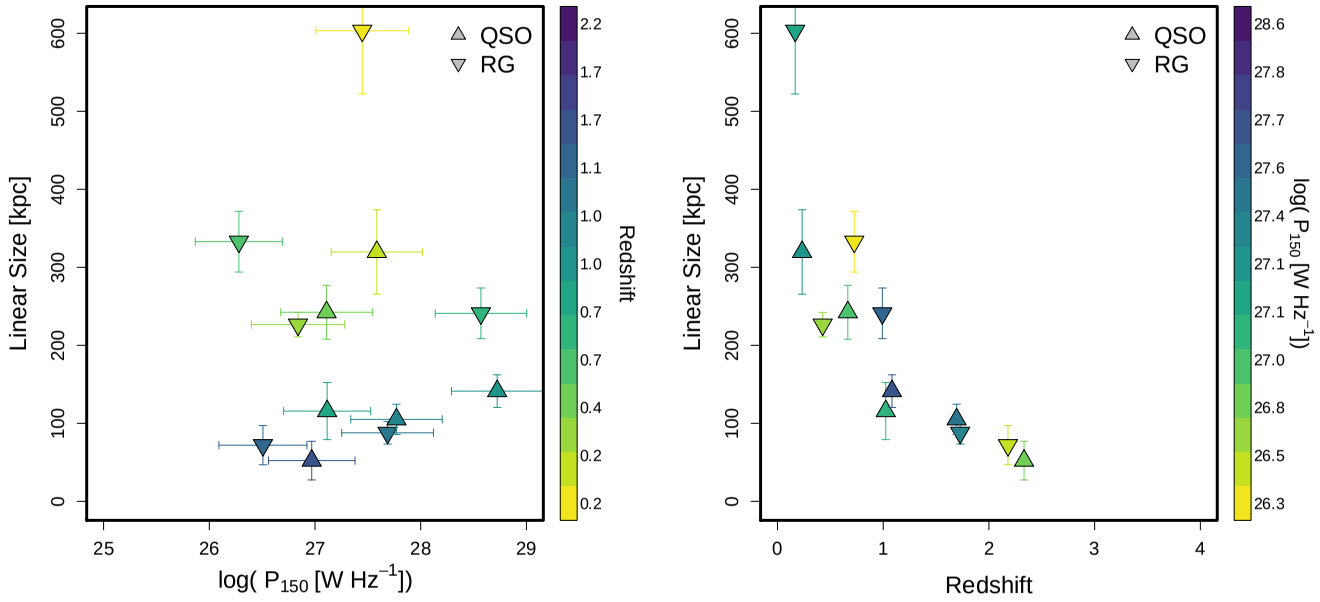

Figure 2.5: The linear sizes of quasars (triangles) and radio galaxies (inverted triangles) plotted against power ($left$) and ($redshift$). The points are coloured according to the colour bar to the right of each plot and show the redshift ($left$) and power ($right$).

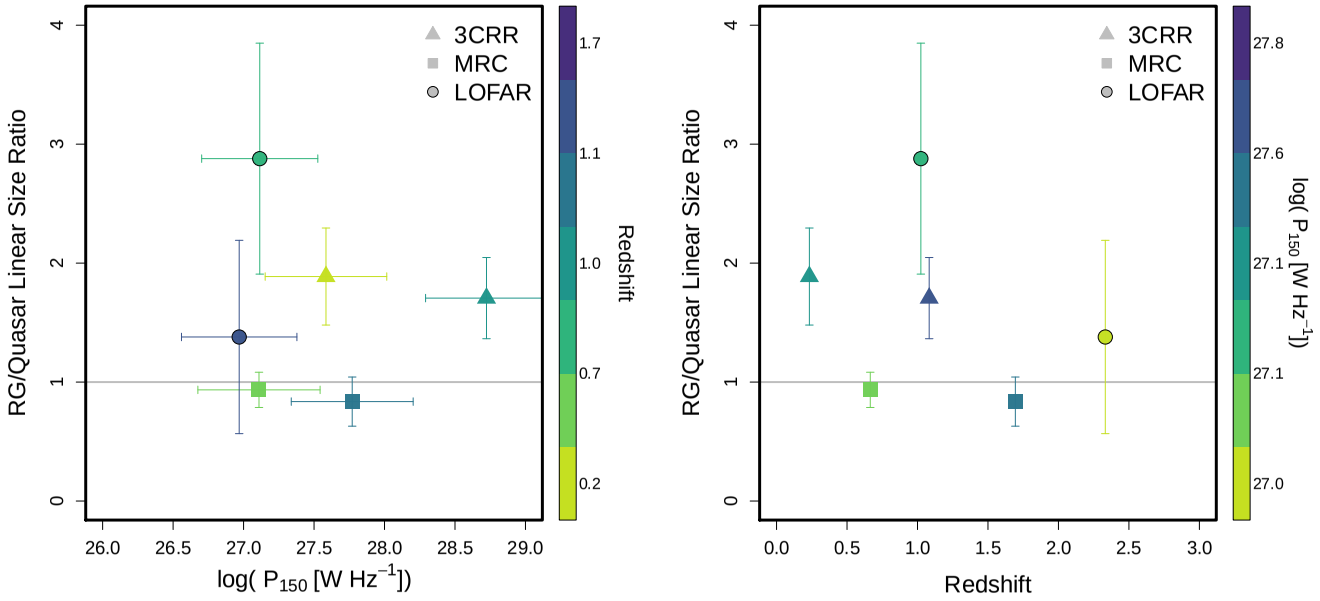

Figure 2.6: The radio galaxy to quasar linear size ratios plotted against power (*left*) and redshift (*right*). The symbol shapes represent the sample, with squares for the MRC, triangles for the 3CRR, and circles for the LOFAR samples. The colour axes are redshift (*left*) and power (*right*). The horizontal gray lines indicate where the linear size ratio is unity.

two groups of points in this plot, one group at quasar fractions of ~ 0.2 and one group at fractions of ~ 0.6 and above. The group of points with quasar fractions of ~ 0.2 corresponds to the lower redshift bins for all samples, while the second group of points corresponds to the higher redshift bins. For the low-redshift bins, the quasar fraction does not appear to evolve with the linear size ratio. For the high-redshift bins, the quasar fraction is correlated with the linear size ratio, and increases from 0.6 to almost unity.

2.5 Discussion

For the discussion, we first consider how the radio data can be interpreted given an orientation-based unification scenario. We then discuss the possibilities if evolution rather than orientation is the dominant effect that explains the data.

2.5.1 Orientation Interpretation

First we consider a scheme where the observed fraction of quasars depends *only* on viewing angle, which is supported by other observational evidence. For example, Antonucci & Ulvestad (1985) used high-resolution observations of blazars to show that they are consistent with being normal radio galaxies viewed along the jet axis. Observed differences in depolarisation of radio lobes (the Laing-Garrington effect) also indicate orientation effects, as the approaching (receding) jet will appear less (more) depolarised due to differential Faraday rotation in the ambient medium along the line of sight (Garrington et al., 1988). In some cases, this can cause sources close to the line of sight (i.e., quasars) to appear one-sided as the receding jet drops below the sensitivity limit. If we assume that all quasars in our LOFAR sample are one-sided and multiply their sizes by a factor of two to account for this, we still find a linear size ratio of radio galaxies to quasars of 1.53 ± 0.48. This is still above unity and therefore consistent with an orientation scheme. This is the *smallest* that the ratio could possibly be, as some quasars have clearly resolved double structure.

The radio orientation is clearly linked to the orientation of the torus/accretion disk, as shown by the detection of significant optical polarisation aligned with the radio jets in nearby galaxies (e.g., Schmidt & Smith, 2000; Antonucci, 1982). The observed properties of strong line AGN (HERGs) at wavelengths other than radio are consistent with orientation schemes, mostly due to the presence of a dusty obscuring structure. For example, the presence of broad lines in polarised light of Type 1 AGN (narrow line galaxies) is powerful evidence for hidden quasars whose light is reflected outside of the obscuring structure (e.g., Cohen et al., 1999; Ogle et al., 1997; Antonucci, 1984).

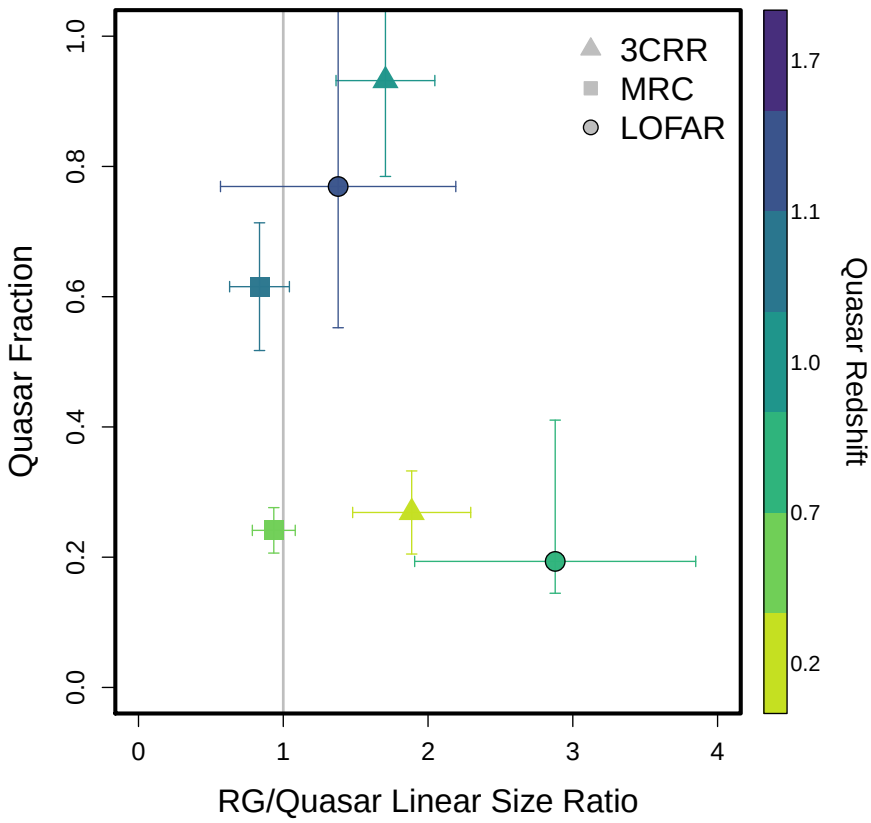

Figure 2.7: The quasar fraction vs. radio galaxy to quasar linear size ratio. Each sample is represented by symbols of different shapes as indicated in the legend. The gray line shows where the ratio between linear sizes of radio galaxies and quasars is unity. The color axis shows redshift.

The unification of observable characteristics of HERGs via orientation predicts several key observable characteristics with which we can compare our results. First, the projected linear sizes of quasars should on average be smaller than the projected linear sizes of radio galaxies. The new LOFAR data are consistent with this, as we found a linear size ratio of 3.1 ± 1.0 (for radio galaxies to quasars). For a population of randomly oriented sources, we can calculate the angle (between 0 and 90 degrees) which would define the division between the two populations. For the LOFAR sample this is $42.8^{+5.4}_{-6.0}$ degrees, which is in agreement with the value of 44.4 degrees found for the original 3CRR sample (Barthel, 1989). That would mean that quasars have their radio jets oriented between 0 degrees (line of sight) and 42.8 degrees, while radio galaxies have jets oriented between 42.8 degrees and 90 degrees (plane of sky).

Second, beamed radio sources with flat spectra should be oriented close to the line of sight, and therefore also be smaller on average than steep-spectrum sources. The LOFAR data is also consistent with this scenario, and the linear size ratio is 4.4 ± 1.4, even larger than the linear size ratio for radio galaxies/quasars. The angle of division between flat and steep spectrum sources is $35.2^{+5.2}_{-5.9}$ degrees. This is consistent with the idea that flat-spectrum sources are mostly beamed radio jets that are oriented close to the line of sight.

Finally, the quasar fraction should be directly correlated with the linear size ratio if *only* orientation is responsible for whether or not we observe a quasar. When dividing the samples into low and high redshift bins, we find that the quasar fraction remains constant with increasing linear size ratios for the low redshift bins, and increases for the high redshift bins. Since the 3CRR and MRC samples are virtually spectroscopically complete, and we have shown in Section 2.2 that we do not believe to be missing a substantial population of sources from the LOFAR sample, the correlation of quasar fraction with linear size at high redshift appears to be real, which is consistent with being due to orientation. Reducing the uncertainties on the LOFAR data point will help unambiguously determine if the low-redshift data is consistent with a constant or increasing quasar fraction.

Overall, we find that the results are consistent with an orientation-based unification scenario. The LOFAR and 3CRR samples show similar trends, while the MRC sample does not show systematically different sizes for quasars and radio galaxies.

2.5.2 Evolutionary Interpretation

Another possibility is that radio galaxies and quasars are linked through an evolutionary scheme rather than by orientation alone. In such a scheme, radio jets would be triggered when quasars become active. The radio jets would grow and finally when the quasar reaches an inactive state the source would be classified as a radio galaxy. The measured quasar fraction in this case would be interpreted as the fraction of time a source spends as an active quasar. In the LOFAR sample the sizes of radio galaxies are on average larger than the sizes of quasars, which is consistent with this evolutionary scheme. However, evolution alone cannot explain observational effects like the Laing-Garrington effect or the presence of scattered quasar light in radio galaxies (e.g., Jackson et al., 1998).

If an evolutionary scheme holds, the fact that higher quasar fractions are seen for the higher redshift bins would mean that either higher redshift sources spend a longer portion of their lives as quasars before becoming radio galaxies, or that there are simply far more young quasars than old radio galaxies at high redshift. If it is true that higher redshift sources spend longer portions of their lives as quasars, the radio jets would have to grow more slowly to be consistent with Fig. 2.6, where we see no change in the linear size ratio with redshift. Slower growth of radio jets could be due to the higher density ambient medium expected at high redshift, but it would not change the amount of time that a quasar is active. The data is therefore inconsistent with this scenario. If there are simply more young quasars at higher redshift, we would expect to see larger linear size ratios between quasars and radio galaxies at high redshift, which is again inconsistent with our results. This could possibly be rectified if *all* sources at high redshift were younger than those at low redshift, but a scenario where this would be the case is hard to imagine.

2.6 Conclusions

In this paper we used a new LOFAR survey of the Boötes field to show that the projected linear sizes of steep-spectrum radio sources are on average 4.4 ± 1.4 times larger than those of flat-spectrum radio sources. This is consistent with an orientation scheme for radio jets, where beamed flat-spectrum radio sources lie closer to the line of sight and therefore have smaller projected sizes.

We have also shown for radio galaxies and quasars in the LOFAR survey, as identified by AGES criteria, the projected linear sizes of radio galaxies are on average 3.1 ± 1.0 times larger than those of quasars. This is also consistent with an orientation scheme, where the presence of a dusty obscuring torus prevents the identification of a quasar unless the radio jets are preferentially aligned

closer to the line of sight.

When combining the new LOFAR measurements with two previous surveys and separating each sample into low and high redshift bins, we find no clear trend between the linear size ratio of radio galaxies to quasars and either power or redshift. This suggests that the populations of radio galaxies and quasars *always* have the same relative sizes. For the low redshift bins, we find that the quasar fraction remains ~ 0.2 even as the linear size ratio changes, although the uncertainties are still large. The MRC sample also consistently measures a linear size ratio of unity, and more data is necessary to resolve the inconsistency of the 3CRR/LOFAR measured size ratios and the MRC measured size ratio.

We conclude that the data presented here are consistent with an orientation-based unification scheme. We have found that on average the projected sizes of radio galaxies are larger than quasars for both the LOFAR and 3CRR samples, and that this does not depend on power or redshift.

Ultimately the LOFAR Tier 1 survey will cover the Northern sky above declination 0 degrees, providing millions of radio sources. Spectroscopic redshifts and host galaxy identifications will be provided by a survey with the William Herschel Telescope Enhanced Area Velocity Explorer (WEAVE) which goes online March 2018. The WEAVE-LOFAR survey (Smith et al., in preparation, Smith, 2015) is dedicated to providing this information for $\sim 10^6$ LOFAR-detected sources in the Tier 1 survey. Ultimately with this information we will be able to break the degeneracy between orientation and evolutionary effects in unification schemes.

Acknowledgements

LKM acknowledges financial support from NWO Top LOFAR project, project n. 614.001.006.

CHAPTER 3

LOFAR VLBI Studies at 55 MHz of 4C 43.15, a z=2.4 Radio Galaxy

"Let us think the unthinkable, let us do the undoable. Let us prepare to grapple with the ineffable itself, and see if we may not eff it after all."
−Douglas Adams−

The correlation between radio spectral index and redshift has been exploited to discover high redshift radio galaxies, but its underlying cause is unclear. It is crucial to characterise the particle acceleration and loss mechanisms in high redshift radio galaxies to understand why their radio spectral indices are steeper than their local counterparts. Low frequency information on scales of ∼ 1 arcsec are necessary to determine the internal spectral index variation. In this paper we present the first spatially resolved studies at frequencies below 100 MHz of the $z = 2.4$ radio galaxy 4C 43.15 which was selected based on its ultra-steep spectral index ($\alpha < -1$; $S_\nu \sim \nu^\alpha$) between 365 MHz and 1.4 GHz. Using the International Low Frequency Array (LOFAR) Low Band Antenna we achieve sub-arcsecond imaging resolution at 55 MHz with VLBI techniques. Our study reveals low-frequency radio emission extended along the jet axis, which connects the two lobes. The integrated spectral index for frequencies < 500 MHz is -0.83. The lobes have integrated spectral indices of -1.31±0.03 and -1.75±0.01 for frequencies ≥ 1.4 GHz, implying a break frequency between 500 MHz and 1.4 GHz. These spectral properties are similar to those of local radio galaxies. We conclude that the initially measured ultra-steep spectral index is due to a combination of the steepening spectrum at high frequencies with a break at intermediate frequencies.

Morabito, L. K., Deller, A. T., Röttgering, H. J. A., Miley, , G., Varenius, E., Shimwell, T. W., Moldón, J., Jackson, N., Morganti, R., van Weeren, R. J., Oonk, J. B. R.
2016, MNRAS, 461, 2676

3.1 Introduction

High redshift radio galaxies (HzRGs) are rare, spectacular objects with extended radio jets whose length exceeds scales of a few kiloparsecs. The radio jets are edge-brightened, Fanaroff-Riley class II (FR II; Fanaroff & Riley, 1974) sources. Found in overdensities of galaxies indicative of protocluster environments (e.g., Pentericci et al., 2000b), HzRGs are among the most massive galaxies in the distant universe and are likely to evolve into modern-day dominant cluster galaxies (Miley & De Breuck, 2008; Best et al., 1997a). They are therefore important probes for studying the formation and evolution of massive galaxies and clusters at $z \geq 2$.

One of the most intriguing characteristics of the relativistic plasma in HzRGs is the correlation between the steepness of the radio spectra and the redshift of the associated host galaxy (Tielens et al., 1979; Blumenthal & Miley, 1979). Radio sources with steeper spectral indices are generally associated with galaxies at higher redshift, and samples of radio sources with ultra-steep spectra ($\alpha \lesssim -1$ where the flux density S is $S \propto \nu^{\alpha}$) were effectively exploited to discover HzRGs (e.g., Röttgering et al., 1994; Chambers et al., 1990, 1987).

The underlying physical cause of this relation is still not understood. Three causes have been proposed: observational biases, environmental influences, and internal particle acceleration mechanisms that produce intrinsically steeper spectra.

Several observational biases can impact the measured relation. Klamer et al. (2006) explored the radio "k-correction" using a sample of 28 spectroscopically confirmed HzRGs. The authors compared the relation between spectral index and redshift as measured from the observed and rest frame spectra, and found that the relation remained unchanged. Another bias could come from the fact that jet power and spectral index are correlated. This manifests in an observed luminosity−redshift correlation: brighter sources (which tend to be at higher redshifts) are more likely to have higher jet power, and therefore steeper spectral indices. For flux density limited surveys this leads to a correlation between power and redshift, and surveys with higher flux density limits have a tighter power−redshift correlation (Blundell et al., 1999).

Environmental effects could also impact the relation. The temperature of the circumgalactic medium is expected to be higher at higher redshifts. It is also known that the linear sizes of radio sources decrease with redshift (e.g., Miley, 1968; Neeser et al., 1995) which is interpreted as lower expansion speeds due to higher surrounding gas densities at higher redshifts. Athreya & Kapahi (1998) point out that the expanding radio lobes therefore have to work against higher

density and temperature. This would slow down the propagation of the jet into the medium, increasing the Fermi acceleration and thus steepening the spectral index. The power−redshift correlation in this case would be caused by a change in environment with redshift.

The final option is that the steeper spectrum is indicative of particle acceleration mechanisms different from those in local radio galaxies. One global difference between low and high redshift sources is that the CMB temperature is higher, and could provide more inverse Compton losses at high frequencies from scattering with CMB photons. Internally to a radio galaxy, spectral indices are seen to evolve along the radio jet axis, with hot spots dominant at high frequencies, and diffuse lobe emission is dominant at low frequencies (e.g. Cygnus A; Carilli et al., 1991). Recently McKean et al. (2016) observed a turnover in the spectra of the hot spots detected with LOFAR around 100 MHz. The authors were able to rule out a cut off in the low-energy electron distribution, and found that both free-free absorption or synchrotron self-absorption models provided adequate fits to the data, albeit with unlikely model parameters. To determine the particle acceleration mechanisms it is crucial to make observations at 100 MHz and below with sufficient resolution to determine the internal variation of the low-frequency spectra. This can then be compared to archival observations with similar or higher resolution at frequencies above 1 GHz, where the internal structure of HzRGs have been well studied (e.g., Carilli et al., 1997; Pentericci et al., 2000a). All current low frequency information that does exist comes from studies in which HzRGs are unresolved.

Typical angular sizes of HzRGs with $z \gtrsim 2$ are about 10 arcsec (Wardle & Miley, 1974), driving the need for resolutions of about an arcsecond to determine the distribution of spectral indices among spatially resolved components of HzRGs. The unique capabilities of the Low Frequency Array (LOFAR; van Haarlem et al., 2013) are ideally suited for revealing these distributions at low frequencies. Covering the frequency bands of 10–80 MHz (Low Band Antenna; LBA) and 120–240 MHz (High Band Antenna; HBA), LOFAR can characterize HzRG spectra down to rest frequencies of ∼ 100 MHz. The full complement of stations comprising International LOFAR (I-LOFAR) provides baselines over 1000 km, and sub-arcsecond resolution is achievable down to frequencies of about 60 MHz.

At such low radio frequencies, very long baseline interferometry (VLBI) becomes increasingly challenging, as signal propagation through the ionosphere along the different sightlines of widely separated stations gives rise to large differential dispersive delays. These vary rapidly both in time and with direction

on the sky, requiring frequent calibration solutions interpolated to the position of the target. Previous works have focused on observations at ~ 150 MHz where I-LOFAR is most sensitive and the dispersive delays are less problematic (Varenius et al., 2015, Varenius et al., A&A submitted). The ν^{-2} frequency dependence of the ionospheric delays means they are six times larger at 60 MHz than at 150 MHz, reducing the bandwidth over which the assumption can be made that the frequency dependence is linear. Combined with the lower sensitivity of I-LOFAR in the LBA band and the reduction in the number of suitable calibration sources due to absorption processes in compact radio sources below 100 MHz, this makes reducing LBA I-LOFAR observations considerably more challenging than HBA observations. Accordingly, the LBA band of I-LOFAR has been less utilised than the HBA. Previous published LBA results have been limited to observations of 3C 196 (Wucknitz, 2010) and the Crab nebula (unpublished) during LOFAR commissioning, when the complement of operational stations limited the longest baseline to ~600 km.

Here we use I-LOFAR to study the spatially resolved properties of 4C 43.15 (also B3 0731+438) at $z = 2.429$ (McCarthy, 1991). This object is one of a sample of 10 that comprise a pilot study of the ultra-steep spectra of HzRGs. We selected 4C 43.15 for this study based on data quality, the suitability of the calibrator, and the simple double-lobed, edge-brightened structure of the target seen at higher frequencies. The overall spectral index of 4C 43.15 between 365 MHz (Texas Survey of Radio Sources; Douglas et al., 1996) and 1400 MHz (from the Green Bank 1.4 GHz Northern Sky Survey; White & Becker, 1992) is $\alpha = -1.1$, which places it well within the scatter on the $\alpha - z$ relation, seen in Figure 1 of De Breuck et al. (2000). 4C 43.15 has been well studied at optical frequencies, and exhibits many of the characteristics of HzRGs (e.g., an extended Lyman-α halo; Villar-Martín et al., 2003).

Here we present images of 4C 43.15 made with the LBA of I-LOFAR at 55 MHz. These are the first images made with the full operational LBA station complement of I-LOFAR in 2015, and this study sets the record for image resolution at frequencies less than 100 MHz. We compare the low frequency properties of 4C 43.15 with high frequency archival data from the Very Large Array (VLA) to measure the spectral behaviour from 55 – 4860 MHz. We describe the calibration strategy we designed to address the unique challenges of VLBI for the LBA band of I-LOFAR. The calibration strategy described here provides the foundation for an ongoing pilot survey of ten HzRGs in the Northern Hemisphere with ultra steep ($\alpha < -1$) spectra.

In § 3.2 we outline the observations and data pre-processing. Section 3.3 de-

scribes the LBA calibration, including the VLBI techniques. The resulting images are presented in § 3.4 and discussed in § 3.5. The conclusions and outlook are summarised in § 3.6. Throughout the paper we assume a ΛCDM concordance cosmology with $H_0 = 67.8\ \mathrm{km\,s^{-1}\,Mpc^{-1}}$, $\Omega_\mathrm{m} = 0.308$, and $\Omega_\Lambda = 0.692$, consistent with Planck Collaboration et al. (2015). At the distance of 4C 43.15, $1''$ corresponds to 8.32 kpc.

3.2 Observations and pre-processing

In this section we describe the observations, pre-processing steps and initial flagging of the data.

As part of project LC3_018, the target 4C 43.15 was observed on 22 Jan 2015 with 8.5 hr on-source time. Using two beams we conducted the observation with simultaneous continuous frequency coverage between 30 and 78 MHz on both the target and a flux density calibrator. Designed with calibration redundancy in mind, the observation started with 3C 147 as the calibrator and switched to 3C 286 halfway though the observation. Although 3C286 was included for calibrator redundancy, it was later realised that the large uncertainties of the current available beam models prevent accurate calibration transfer to the target at this large angular separation. The observations are summarized in Table 3.1.

All 46 operational LBA stations participated in the observation, including 24 core stations, 14 remote stations, and 8 international stations. The international stations included 5 in Germany (DE601-DE605) and one each in Sweden (SE607), France (FR606), and the United Kingdom (UK608). While all stations have 96 dipoles, the core and remote stations are limited by electronics to only using 48 dipoles at one time. The observation was made in the LBA_OUTER configuration, which uses only the outermost 48 dipoles in the core and remote stations. This configuration reduces the amount of cross-talk between closely spaced dipoles and gives a smaller field of view when compared with other configurations. The international stations always use all 96 dipoles, and thus have roughly twice the sensitivity of core and remote stations. The raw data were recorded with an integration time of 1 s and 64 channels per 0.195 MHz subband to facilitate radio frequency interference (RFI) excision.

3.2.1 Radio Observatory Processing

All data were recorded in 8-bit mode and correlated with the COBALT correlator to produce all linear correlation products (XX, XY, YX, YY). After correlation

the data were pre-processed by the Radio Observatory. Radio frequency interference was excised using AOFlagger (Offringa, 2010) with the default LBA flagging strategy. The data were averaged to 32 channels per subband (to preserve spectral resolution for future studies of carbon radio recombination lines) and 2 second integration time (to preserve information on the time-dependence of phases) before being placed in the Long Term Archive (LTA). The data were retrieved from the LTA and further processed on a parallel cluster kept up to date with the most current stable LOFAR software available at the time (versions 2.9 – 2.15).

3.3 Data Calibration

In this section we describe in detail the steps taken to calibrate the entire LBA, including international stations, paying particular attention to how we address the unique challenges at low frequencies. Figure 3.1 shows a block diagram overview of the calibration steps.

3.3.1 Initial flagging and data selection

Our first step after downloading the data from the LTA was to run AOFlagger again with the LBA default strategy. Typically 0.5 to 2 per cent of the data in each subband were flagged. An inspection of gain solutions from an initial gain calibration of the entire bandwidth on 3C 147 showed that the Dutch remote station RS409 had dropped out halfway through the first observing block, and we flagged this station and removed it from the dataset. We further excised one core station (CS501) and one remote station (RS210) after manual inspection.

We determined the normalised standard deviation per subband from the calibrator data and used this information to select the most sensitive subbands close to the peak sensitivity of the LBA. Outside these subbands the normalised standard deviation rapidly increases towards the edges of the frequency range. The total contiguous bandwidth selected was 15.6 MHz with a central frequency of 55 MHz. During this half of the observation, the standard calibrator 3C 147 was always less than 20 degrees different in elevation from the target, and the absolute flux density errors are expected to be less than 20 per cent. This is important for two reasons. First, amplitude errors from beam correction models are reduced when objects are close in elevation. The second reason is that we transfer information derived from the calibrator phases (see § 3.3.10 for full details) to the target. This information is valid for a particular direction on the sky, and transferral over very large distances will not improve the signal to noise ratio for the target data. For the second half of the observation, 3C 286 was more than

Table 3.1: Observations. The bandwidth for all targets was 48 MHz, split into 244 subbands of 0.195 kHz width. Overlapping times are due to the use of simultaneous beams. Right ascension is hh:mm:ss.ss, and declination is dd:mm:ss.ss.

Obs. ID	Object	Type	RA	Dec	Date start	UT start	UT stop	exposure
L257205	3C 147	Calibrator	05:42:36.26	+49:51:07.08	22-Jan-2015	18:32:33	22:47:32	4.25 hr
L257207	4C 43.15	Target	07:35:21.89	+43:44:20.20	22-Jan-2015	18:32:33	22:47:32	4.25 hr
L257209	3C 147	Calibrator	05:42:36.26	+49:51:07.08	22-Jan-2015	22:48:33	23:03:32	0.25 hr
L257211	3C 286	Calibrator	13:31:08.28	+30:30:32.95	22-Jan-2015	22:48:33	23:03:32	0.25 hr
L257213	3C 286	Calibrator	13:31:08.28	+30:30:32.95	22-Jan-2015	23:04:33	03:19:32	4.25 hr
L257215	4C 43.15	Target	07:35:21.89	+43:44:20.20	22-Jan-2015	23:04:33	03:19:32	4.25 hr

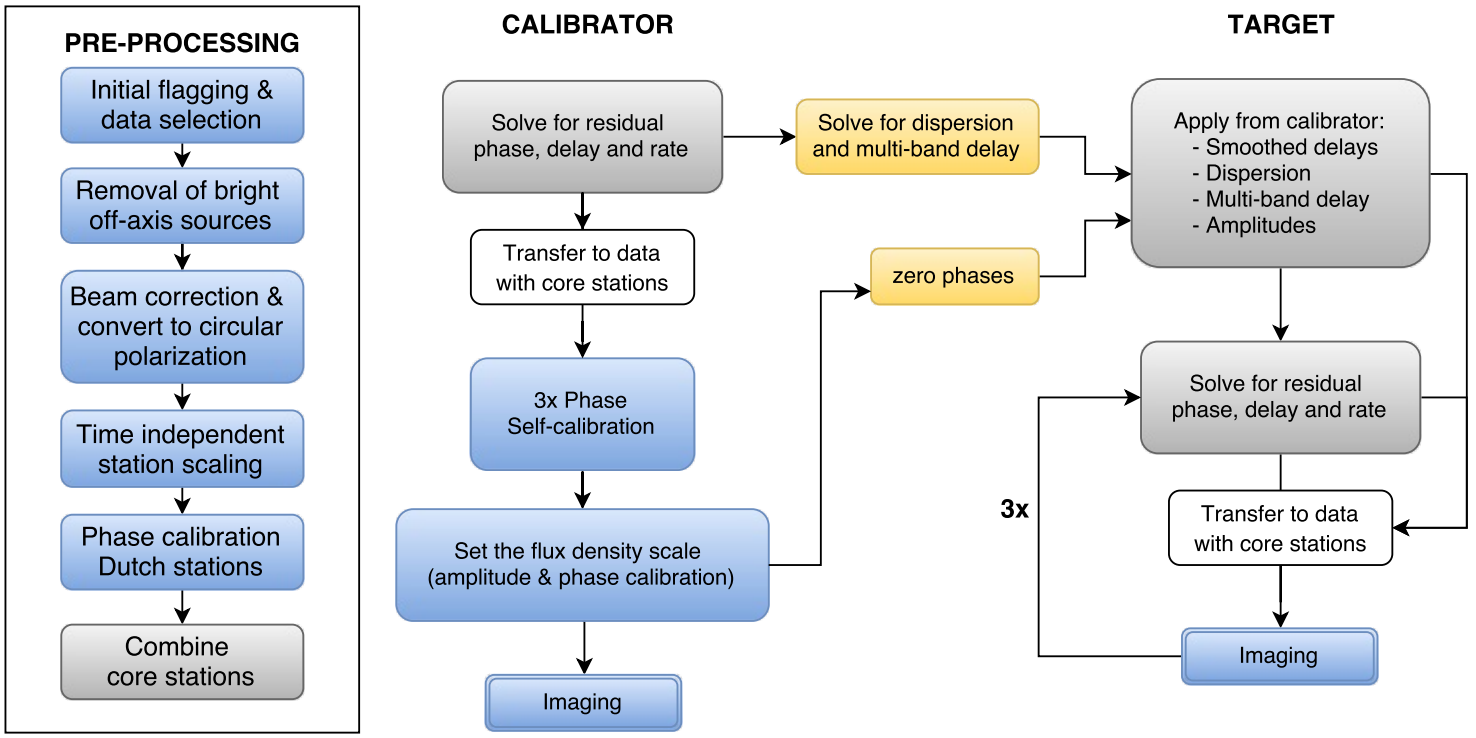

Figure 3.1: A block diagram overview of the calibration steps. Blue blocks represent operations on data sets with core stations, while gray blocks represent operations on data sets where the core stations have been combined into the 'super' station (see § 3.3.6 for details on station combination). Yellow blocks represent operations on solution tables rather than data.

20 degrees distant from 4C 43.15 for most of that observation block, requiring more advanced calibration which is beyond the scope of this paper, and would only provide $\sqrt{2}$ noise improvement. The second half of the observation was therefore not used for the data analysis in this paper.

3.3.2 Removal of bright off-axis sources

Bright off-axis sources contribute significantly to the visibilities. At low frequencies, this problem is exacerbated by LOFAR's wide field of view and large primary beam sidelobes. There are several sources that have brightnesses of thousands to tens of thousands of Janskys within the LBA frequency range, and they need to be dealt with. We accomplished the removal of bright off-axis sources using a method called demixing (van der Tol et al., 2007), where the data are phase-shifted to the off-axis source, averaged to mimic beam and time smearing, and calibrated against a model. All baselines were demixed, although simulations performed as part of commissioning work showed that the source models have insufficient resolution to correctly predict the compact bright sources to which the longest baselines would be sensitive (see Appendix B of this thesis for more details). Such sources produce strong beating in the amplitudes of the visibilities, which is visible by eye. A careful visual inspection ensured that this was not a problem for these data. Using the calibration solutions, the *uncorrected* visibilities for the source are subtracted. After examination of the bright off-axis sources above the horizon and within 90° of the target and calibrator (such a large radius is necessary in case there are sources in sidelobes), we demixed Cassiopeia A and Taurus A from our data. After demixing the data were averaged to 16 channels per subband to reduce the data volume, and the AOFlagger was run again with the default LBA flagging strategy. Typical flagging percentages were 2–4 per cent. The combined losses from time (2 sec) and bandwidth (4 channels per 195 kHz subband) smearing on the longest baseline are 5 per cent at a radius of 95 arcsec (Bridle & Schwab, 1999). Higher frequency observations of 4C 43.15 show its largest angular size to be 11 arcsec, well within this field of view.

3.3.3 LOFAR beam correction and conversion to circular polarization

At low frequencies, differential Faraday rotation from propagation through the ionosphere can shift flux density from the XX and YY to the cross hand polarizations. An effective way to deal with this is to convert from linear to circular polarization, which shifts the impact of differential Faraday rotation to only a L-R phase offset in the resulting circular polarization. Since the conversion from

linear to circular polarization is beam dependent, we first removed the beam. We used MSCORPOL (version 1.7)[1] to accomplish both removal of beam effects and conversion to circular polarization. This software performs a correction for the geometric projection of the incident electric field onto the antennas, which are modelled as ideal electric dipoles. One drawback of MSCORPOL is that it does not yet include frequency dependence in the beam model, so we also replicated our entire calibration strategy but correcting for the beam with the LOFAR *new default pre-processing pipeline* (NDPPP), which has frequency-dependent beam models, rather than MSCORPOL. We converted the NDPPP beam-corrected data to circular polarization using standard equations, and followed the same calibration steps described below. We found that data where the beam was removed with MSCORPOL ultimately had more robust calibration solutions and better reproduced the input model for the calibrator. Therefore we chose to use the MSCORPOL beam correction.

3.3.4 Time-independent station scaling

The visibilities for the international stations must be scaled to approximately the right amplitudes relative to the core and remote stations before calibration. This is important because the amplitudes of the visibilities are later used to calculate the data weights, which are used in subsequent calibration steps, see § 3.3.7. To do this we solved for the diagonal gains (RR,LL) on all baselines using the Statistical Efficient Calibration (StEfCal; Salvini & Wijnholds, 2014) algorithm in NDPPP. One solution was calculated every eight seconds per 0.915 MHz bandwidth (one subband). The StEfCal algorithm calculates time and frequency independent phase errors, and does not take into account how phase changes with frequency (the delay; $d\phi/d\nu$) or time (the rate; $d\phi/dt$). If the solution interval over which StEfCal operates is large compared to these effects, the resulting incoherent averaging will result in a reduction in signal to noise. Since the incoherently averaged amplitudes are adjusted to the correct level, the coherence losses manifest as an increase of the noise level. Using the maximal values for delays and rates found in § 3.3.7 to calculate the signal to noise reduction (from Eqn. 9.8 and 9.11 of Moran & Dhawan, 1995), we find losses of 6 and 16 per cent for delays and rates, respectively.

The calibrator 3C 147 flux density was given by the model from Scaife & Heald (2012). 3C 147 is expected to be unresolved or only marginally resolved and therefore expeted to provide an equal amplitude response to baselines of

[1] MSCORPOL was developed by T. D. Carozzi and is available at: https://github.com/2baOrNot2ba/mscorpol

any length. We use this gain calibration for two tasks: (i) to find an overall scaling factor for each station that correctly provides the relative amplitudes of all stations; and (ii) to identify bad data using the LOFAR Solution Tool[2]. About 20 per cent of the solutions were flagged either due to outliers or periods of time with loss of phase coherence, and we transferred these flags back to the data. To find the time-independent scaling factor per station, we zeroed the phases and calculated a single time-averaged amplitude correction for each antenna. These corrections were applied to both calibrator and target datasets.

3.3.5 Phase calibration for Dutch stations

We solved for overall phase corrections using only the Dutch array but filtering core – core station baselines, which can have substantial low-level RFI and are sensitive to extended emission. The phase calibration removes ionospheric distortions in the direction of the dominant source at the pointing centre. We performed the phase calibration separately for 3C 147 and 4C 43.15 using appropriate skymodels. 3C 147 is the dominant source in its field, and we use the Scaife & Heald (2012) point source model. 4C 43.15 has a flux density of at least 10 Jy in the LBA frequency range. We used an apparent sky model of the field constructed from the TGSS Alternative Data Release 1 (Intema et al., 2016), containing all sources within 7 degrees of our target and with a flux density above 1 Jy.

3.3.6 Combining core stations

After phase calibration of the Dutch stations for both the calibrator and the target, we coherently added the visibilities from the core stations to create a 'super' station. This provides an extremely sensitive 'super' station with increased signal to noise on individual baselines to anchor the I-LOFAR calibration (described further in § 3.3.7). All core stations are referred to a single clock and hence should have delays and rates that are negligibly different after phase calibration is performed. The station combination was accomplished with the Station Adder in NDPPP by taking the weighted average of all visibilities on particular baselines. For each remote and international station, all visibilities on baselines between that station and the core stations are averaged together taking the data weights into account. The new u, v, w coordinates are calculated as the weighted geometric center of the u, v, w coordinates of the visibilities being

[2]The LOFAR Solution Tool (LoSoTo) was developed by Francesco de Gasperin and is available at: https://github.com/revoltek/losoto

combined[3]. Once the core stations were combined, we created a new data set containing only the 'super' station and remote and international stations. The dataset with the uncombined core stations was kept for later use. The final averaging parameters for the data were 4 channels per subband for 3C 147, and 8 channels per subband for 4C 43.15. After averaging the data were again flagged with the AOFlagger default LBA flagging strategy, which flagged another 1 – 2 per cent of the data.

3.3.7 Calibrator residual phase, delay, and rate

The international stations are separated by up to 1292 km and have independent clocks which time stamp the data at the correlator. There are residual non-dispersive delays due to the offset of the separate rubidium clocks at each station. Correlator model errors can also introduce residual non-dispersive delays up to ~ 100ns. Dispersive delays from the ionosphere make a large contribution to the phase errors. Given enough signal to noise on every baseline, we could solve for the phase errors over small enough time and bandwidth intervals that the dispersive errors can be approximated as constant. However, a single international-international baseline is only sensitive to sources of ~ 10Jy over the resolution of our data ($\Delta\nu = 0.195\,\mathrm{MHz}$, 2 sec). Larger bandwidth and time intervals increase the signal to noise ratio, and the next step is to model the dispersive delays and rates with linear slopes in frequency and time. This can be done using a technique known as fringe-fitting (e.g., Cotton, 1995; Thompson et al., 2001). A global fringe-fitting algorithm is implemented as the task FRING in the Astronomical Image Processing System (AIPS; Greisen, 2003). We therefore converted our data from measurement set to UVFITS format using the task MS2UVFITS and read it into AIPS. The data weights of each visibility were set to be the inverse square of the standard deviation of the data within a three minute window.

The ionosphere introduces a dispersive delay, where the phase corruption from the ionosphere is inversely proportional to frequency, $\phi_{\mathrm{ion}} \propto \nu^{-1}$. The dispersive delay is therefore inversely proportional to frequency squared, $d\phi/d\nu \propto -\nu^{-2}$. Non-dispersive delays such as those introduced by clock offsets are frequency-independent. The ionospheric delay is by far the dominant effect. For a more in-depth discussion of all the different contributions to the delay at

[3]We found an extra 1 per cent reduction in noise for the calibrator when using the weighted geometric center of the u, v, w coordinates, rather than calculating the u, v, w coordinates based on the 'super' station position. This has been implemented in NDPPP (LOFAR software version 12.2.0). *This is described in Appendix A of this thesis.*

150 MHz for LOFAR, see Moldón et al. (2015). The delay fitting-task FRING in AIPS fits a single, non-dispersive delay solution to each so-called *intermediate frequency* (IF), where an IF is a continuous bandwidth segment. With I-LOFAR data, we have the freedom to choose the desired IF bandwidth by combining any number of LOFAR subbands (each of width 0.195 MHz). This allows us to make a piece-wise linear approximation to the true phase behaviour. Making wider IFs provides a higher peak sensitivity, but leads to increasingly large deviations between the (non-dispersive only) model and the (dispersive and non-dispersive) reality at the IF edges when the dispersive delay contribution is large. As a compromise, we create 8 IFs of width 1.95 MHz each (10 LOFAR subbands), and each IF is calibrated independently. We used high resolution model of 3C 147 (from a previous I-LOFAR HBA observation at 150 MHz) for the calibration, and set the total flux density scale from Scaife & Heald (2012). The solution interval was set to 30 seconds, and we found solutions for all antennas using only baselines with a projected separation $> 10\mathrm{k}\lambda$, effectively removing data from all baselines containing only Dutch stations. The calibration used the 'super' station as the reference antenna.

The search windows were limited to $5\,\mu$s for delays and 80 mHz for rates. Typical delays for remote stations were 30 ns, while international station delays ranged from 100 ns to $1\,\mu$s. The delay solutions showed the expected behaviour, with larger offsets from zero for longer baselines, and increasing magnitudes (away from zero) with decreasing frequency. Rates were typically up to a few tens of mHz for remote and international stations.

3.3.8 Calibrator phase self-calibration

The combined 'super' station, while useful for gaining signal to noise on individual baselines during fringe-fitting, left undesirable artefacts when imaging. This can occur if the phase-only calibration prior to station combination is imperfect. The imperfect calibration will result in the 'super' station not having a sensitivity equal to the sum of the constituent core stations. The 'super' station also has a much smaller field of view than the other stations in the array. Therefore we transferred the fringe-fitting solutions to a dataset where the core stations were not combined.

Before applying the calibration solutions we smoothed the delays and rates with solution intervals of 6 and 12 minutes, respectively, after clipping outliers (solutions more than 20 mHz and 50 ns different from the smoothed value within a 30 minute window for rates and delays, respectively). The smoothing intervals were determined by comparing with the unsmoothed solutions to find the small-

est time window that did not oversmooth the data. We applied the solutions to a dataset where the core stations were not combined. The data were then averaged by a factor of two in time prior to self-calibration to 4 second integration times. We performed three phase-only self-calibration loops with time intervals of 30 seconds, 8 seconds, and 4 seconds. Further self-calibration did not improve the image fidelity or reduce the image noise.

3.3.9 Setting the flux density scale

After applying the final phase-only calibration, we solved for amplitude and phase with a 5 minute solution interval, as the amplitudes vary slowly with time. The amplitude solutions provide time-variable *corrections* to the initial default station amplitude calibration. Fig. 3.2 shows the amplitude solutions per station for an IF near the centre of the band.

The amplitude solutions show some small-scale variations in time, but are stable to within 20 per cent of the median value over the entirety of the observation. We therefore adopt errors of 20 per cent for the measurements presented here. Several effects could be responsible for the variations in time such as imperfect beam or source models, or ionospheric disturbances. Currently we are not able at this time to distinguish whether the time variation we see is from the ionosphere or beam errors.

We checked the calibration of 3C 147 by imaging each IF of the final self-calibrated data separately, fitting a Gaussian to extract the integrated flux density, and plotting this against the input model, see Figure 3.3. The integrated flux density measurements are within the errors of the point-source model, while the peak brightness measurements are below the model. This is due to the fact that the jet in 3C 147, which is seen also at higher frequencies, is resolved (the restoring beam is $0.9'' \times 0.6''$). The values are systematically lower than the model, and slightly flatter. This could be due to the fact that the starting model from Scaife & Heald (2012) is a point source model, and 3C 147 is resolved. The flattening spectral index towards higher frequencies, where the beam size is smaller, implies that the jet which appears as a NW-elongation in Figure 3.4 has a steeper low-frequency spectral index than the core. This is supported by the fact that the peak brightness measurements are slightly flatter than the integrated flux density measurements in Figure 3.3.

In some extremely compact objects, scintillation effects from the interstellar medium have been seen to artificially broaden sources (e.g., Linsky et al., 2008; Quirrenbach, 1992; Rickett, 1986). However, these scintillations are usually only seen in compact ($\sim$10 mas) sources and/or on longer timescales (days to

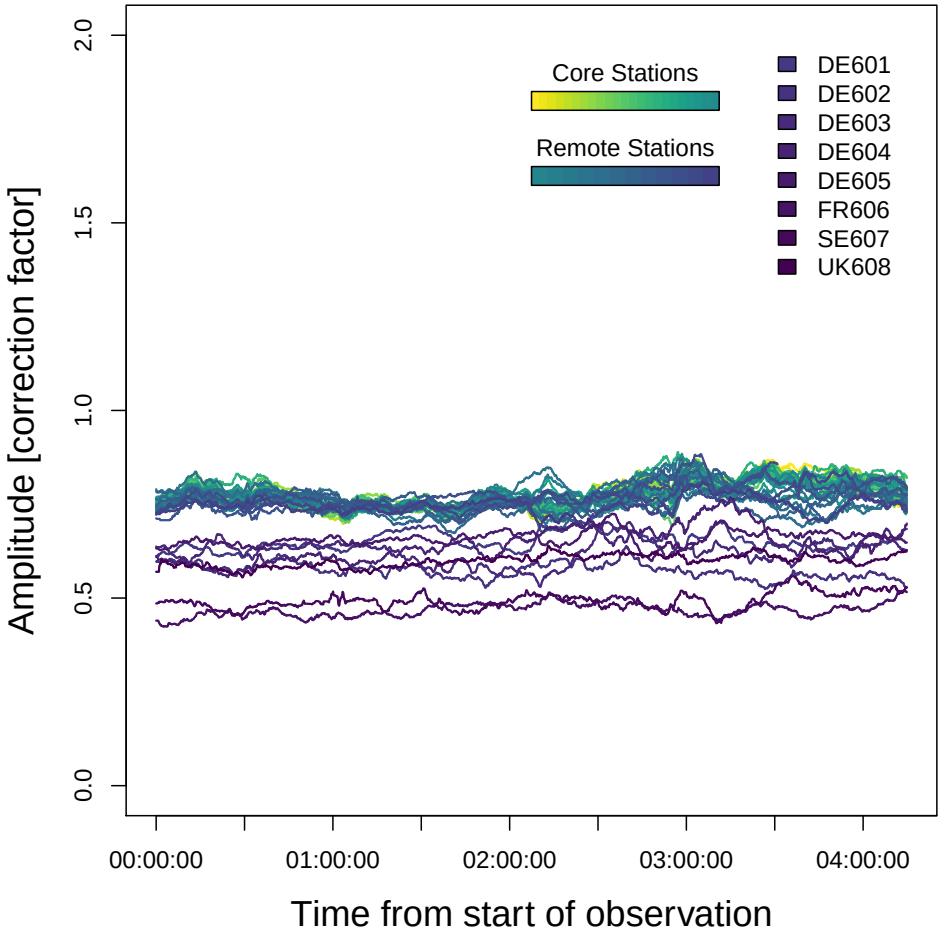

Figure 3.2: Amplitude solutions for all stations, from the final step of self-calibration. These are *corrections* to the initial amplitude calibration of each station, for the central IF at 53 MHz. The colours go from core stations (darkest) to international stations (lightest).

weeks). Both the calibrator and target are larger in size, and well outside of the galactic plane (above $b = 20°$). We thus do not expect that they should be impacted. The final self-calibrated image using the entire bandwidth is shown in Fig. 3.4, and has a noise of $135\,\mathrm{mJy\,bm^{-1}}$, about a factor of 3 above the expected noise given the amount of flagging (40 per cent) and the $u - v$ cut in imaging ($> 20\,\mathrm{k}\lambda$).

3.3.10 Target residual phase, delay, and rate

Before fringe-fitting on the target, the time independent and dependent amplitude corrections derived from the calibrator were applied to the target, for a dataset with the 'super' station. The time dependent core station amplitude corrections were all within a few per cent of each other so we transferred the amplitude corrections from a station close to the centre of the array, CS001, to the 'super' station. The fringe-fitting solutions from the calibrator, approximately 20° away, should also contain some instrumental and systematic effects, such as those due to clock offsets and large-scale ionospheric structure, which will be common to the target direction and can be usefully subtracted by applying the calibrator solutions to the target data. After extensive testing, we found that we gained the most signal to noise in the fringe-fitting by applying the smoothed delays from the calibrator, along with a model of the frequency dependence of the phases. We used the AIPS task MBDLY to model the frequency dependence from the FRING calibration solutions with smoothed delays. We used the 'DISP' option of MBDLY to find the dispersion and multi-band delay for each solution in the fringe-fitting calibration table. After zeroing the phases and rates in the FRING calibration solutions, we used the MBDLY results to correct for the multi-band delay and the dispersion. With the phases already zeroed, the dispersion provides a *relative* correction of the phases, effectively removing the frequency dependence. This allowed us to use a wider bandwidth in the FRING algorithm, which increased the signal to noise. We chose to use the entire 15.6 MHz bandwidth. The resultant delays were smaller by at least a factor of two on the longest baselines, which was expected as transferring the delays from the calibrator already should have corrected the bulk of the delays. These residual delays are then the *difference* in the dispersion and multi-band delays between the target and the calibrator. We also tested the effect of only including data from partial uv selections and established that it was necessary to use the full uv range to find robust fringe-fitting solutions. It is important to remember that the shortest baseline is from the 'super' station to the nearest remote station. There are 12 remote station – 'super' station baselines, ranging from about 4 km

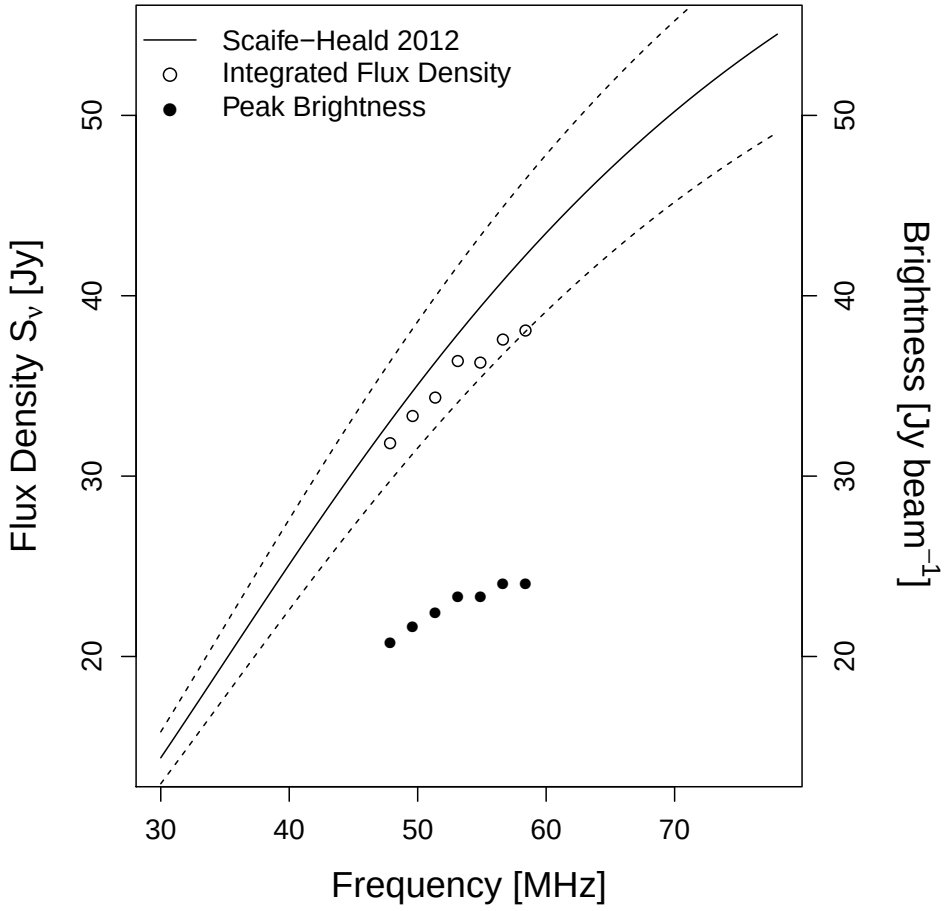

Figure 3.3: Spectral energy distribution (SED) of 3C 147. The solid line shows the calibration model that we used, while the dashed lines indicate errors of 10 per cent. The open circles show the integrated flux density measurements from each IF, while the filled circles show the peak brightness measurements.

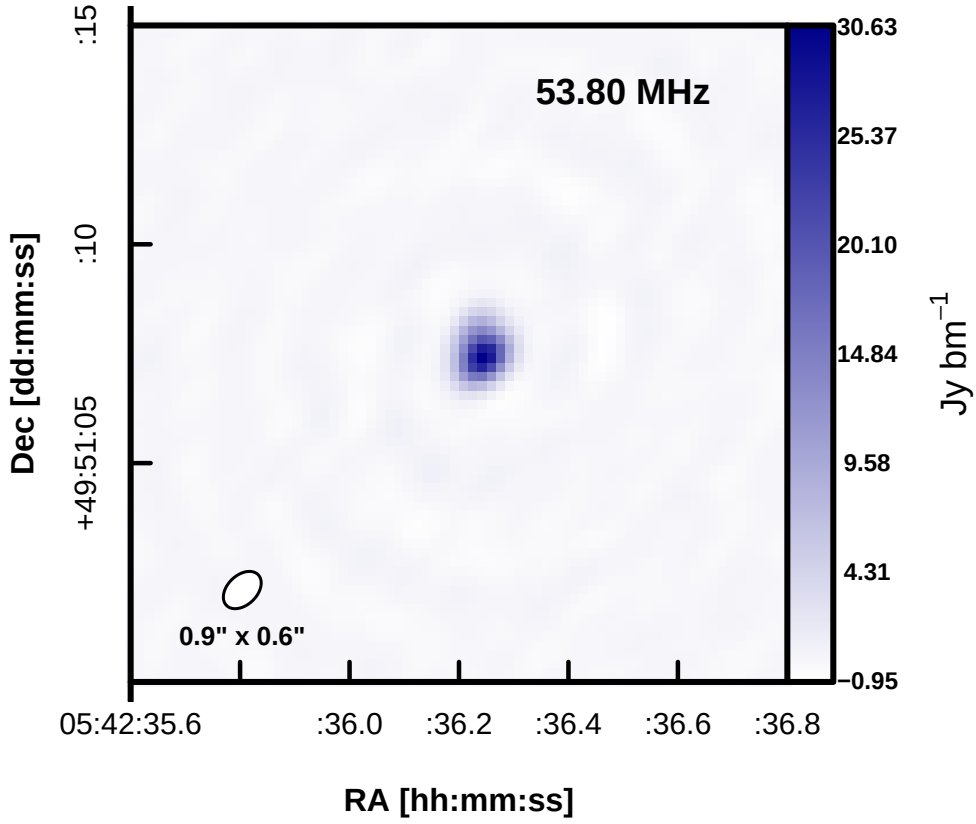

Figure 3.4: The calibrator, 3C 147, imaged using 15.6 MHz bandwidth and 4.25 hr of data. The noise in the image is 135 mJy bm^{-1}. The NW-elongation is a jet also seen at higher frequencies.

to 55 km, with a median length of about 16 km.

The next step was to perform fringe fitting on the target. We began fringe fitting using a point source model with a flux density equal to the integrated flux density of the target measured from a low-resolution image made with only the Dutch array. Initial tests showed a double source with similar separation and position angle (PA) as seen for 4C 43.15 at higher frequencies, rather than the input point source model. We further self-calibrated by using the resulting image as a starting model for fringe-fitting. We repeated this self-calibration until the image stopped improving.

3.3.11 Astrometric Corrections

The process of fringe frequency fitting does not derive absolute phases or preserve absolute positions, only relative ones. To derive the absolute astrometric positions we assumed that the components visible in our derived images coincided with the components visible on the high-frequency archival data for which the absolute astrometry was correct. We centred the low-frequency lobes in the direction perpendicular to the jet axis, and along the jet axis we centred the maximum extent of the low-frequency emission between the maximum extent of the high frequency emission. The re-positioning of the source is accurate to within $\sim 0.6''$ assuming that the total extent of the low-frequency emission is contained within the total extent of the high-frequency emission. This positional uncertainty will not affect the following analysis.

3.4 Results

In Figure 3.5 we present an LBA image of 4C 43.15 which achieves a resolution of $0.9'' \times 0.6''$ with PA -33 deg and has a noise level of 59 mJy bm^{-1}. This image was made using multi-scale CLEAN in the Common Astronomy Software Applications (CASA; McMullin et al., 2007) software package, with Briggs weighting and a robust parameter of -1.5, which is close to uniform weighting and offers higher resolution than natural weighting. The contours show the significance of the detection (starting at 3σ and up to 20σ). *This is the first image made with sub-arcsecond resolution at frequencies below 100 MHz.* The beam area is a factor of 2.5 smaller than that achieved by Wucknitz (2010). The measured noise is a factor of 2.4 above the theoretical noise.

In the following subsections we examine first the morphology of 4C 43.15 and then the spectral index properties of the source. For comparison with higher

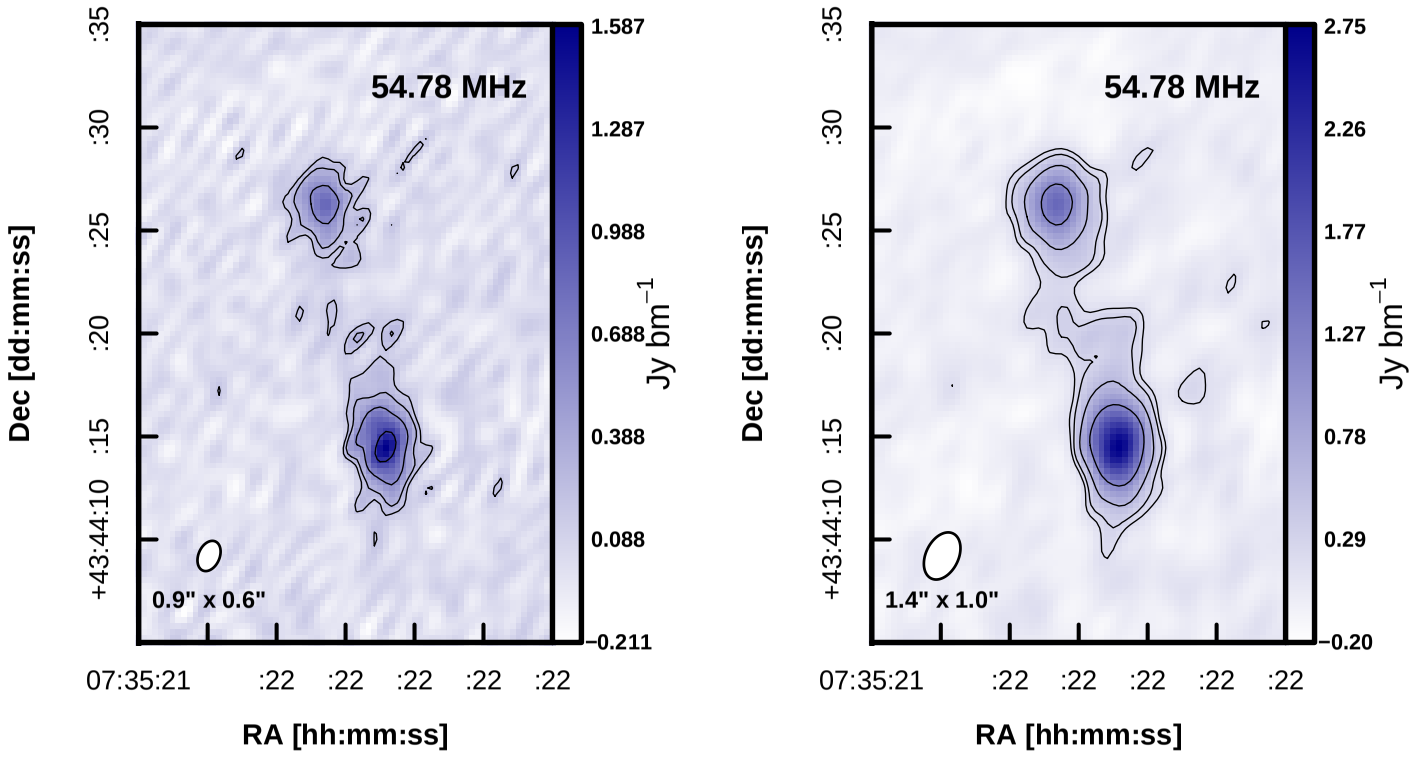

Figure 3.5: The final LBA images of 4C 43.15. The image on the left was made using 15.6 MHz of bandwidth centred on 55 MHz. We used the multi-scale function of the CLEAN task in CASA with Briggs weighting (robust -1.5) and no inner uv cut. The image noise achieved is 59 mJy bm^{-1}, while the expected noise given the amount of flagged data and image weighting is 25 mJy bm^{-1}. The final restoring beam is $0.9'' \times 0.6''$ with PA -33 deg. The image on the right is the same image, but smoothed with a Gaussian kernel 1.2 times the size of the restoring beam. The contours in both images are drawn at the same levels, which are 3, 5, 10, and 20σ of the unsmoothed image.

Table 3.2: Summary of archival VLA data and re-imaging parameters. All data were taken in A-configuration, which has a minimum baseline of 0.68 km and a maximum baseline of 36.4 km.

Date observed	ν [GHz]	Weighting	Maximum baseline	Beam size
31-08-1995	1.4	super uniform	–	$1.55'' \times 0.98''$
19-03-1994	4.7	natural	192 kλ	$1.02'' \times 0.88''$
31-08-1995	8.4	natural	192 kλ	$1.05'' \times 0.83''$

frequencies, we used archival data from the NRAO VLA Archive Survey[4]. The available images had higher resolution than the LBA image presented here, with the exception of images at 1.4 GHz. We therefore downloaded and re-imaged the calibrated data to produce more similar beam sizes with the use of different weighting and/or maximum baseline length. The archival data and resulting beam sizes are listed in Table 3.2. All images were then convolved to the largest beam full width at half maximum (FWHM) of $1.55'' \times 0.98''$ (at 1.4 GHz). Even at the highest frequency used here (8.4 GHz) the A-configuration of the VLA is still sensitive to emission on scales of about $5''$, or roughly the size of a single lobe of 4C 43.15. We therefore do not expect that the image misses significant contributions to the flux density. This is supported by the third panel in Figure 3.8, which shows that the spectral indices from 1.4 GHz to the two higher frequencies in this study are the same within the errors. If a substantial amount of flux density were missing at 8.4 GHz, we would expect to see a steeper spectral index from 1.4 GHz to 8.4 GHz than from 1.4 GHz to 4.7 GHz.

3.4.1 Morphology

Figure 3.5 shows two radio lobes that are edge brightened, the classic signature of an FR II source. FR II sources have several components. There are collimated jets that extend in opposite directions from the host galaxy, terminating in hot spots that are bright, concentrated regions of emission. More diffuse, extended radio emission from plasma flowing back from the hot spots comprises the lobes. In HzRGs, only the hotspots and lobes have been directly observed, since the jets have low surface brightness. Observations of 4C 43.15 at frequencies higher than 1 GHz clearly show the hot spots and diffuse lobe emission, but this is the first time this morphology has been spatially resolved for an HzRG at frequencies < 300 MHz. The smoothed image shows a bridge of emission connecting

[4] http://archive.nrao.edu/nvas/

the two lobes at the 3 and 5σ significance levels. This is similar to what is seen in the canonical low-redshift FR II galaxy, Cygnus A (Carilli et al., 1991), but this is *the first time that a bridge of low frequency emission connecting the two lobes has been observed in a HzRG.*

To qualitatively study the low-frequency morphology of 4C 43.15 in more detail and compare it with the structure at high frequencies, we derived the brightness profiles along and perpendicular to the source axis. To do this we defined the jet axis by drawing a line between the centroids of Gaussian fits to each lobe. We used the position angle of this line to rotate all images (the unsmoothed image was used for the 55 MHz image) so the jet axis is aligned with North. We fitted for the rotation angle independently for all frequencies, and found the measured position angles were all within 1 degree of each other, so we used the average value of 13.36 degrees to rotate all images. The rotated images are shown overlaid on each other in Figure 3.6, along with normalized sums of the flux density along the North–South direction and East–West direction.

The integrated flux density ratio of the lobes also evolves with frequency, which can be seen in Figure 3.6. The lobe ratio changes from 3 at the highest frequency to 1.7 at the lowest frequency. This implies a difference in spectral index between the two lobes, which will be discussed in the next section.

3.4.2 Spectral Index Properties

In this section we shall describe the spectral index properties of 4C 43.15 using the integrated spectra from each of the lobes, and the total integrated spectral index. Figure 3.7 shows the lobe spectra and the total integrated spectrum for comparison. The lobe spectra at 1.4, 4.7, and 8.4 GHz were measured from VLA archival images convolved to the resolution at 1.4 GHz and are reported in Table 3.4. We assumed errors of 20 per cent for the LOFAR data and 5 per cent for the VLA archival data. The integrated spectral data were taken from the NASA/IPAC Extragalactic Database (NED), with the inclusion of the new LOFAR data point, see Table 3.3.

Figure 3.8 shows the point-to-point spectral index values measured from each frequency to all other frequencies in this study. There are several interesting results.

1. The spectral index values amongst frequencies ≥ 1.4 GHz show a steepening high-frequency spectrum. This can be seen most clearly in the second panel from the top of Figure 3.8, where the spectral index from 4.7 GHz to 8.4 GHz is always steeper than the spectral index from 4.7 GHz to 1.4 GHz for all components.

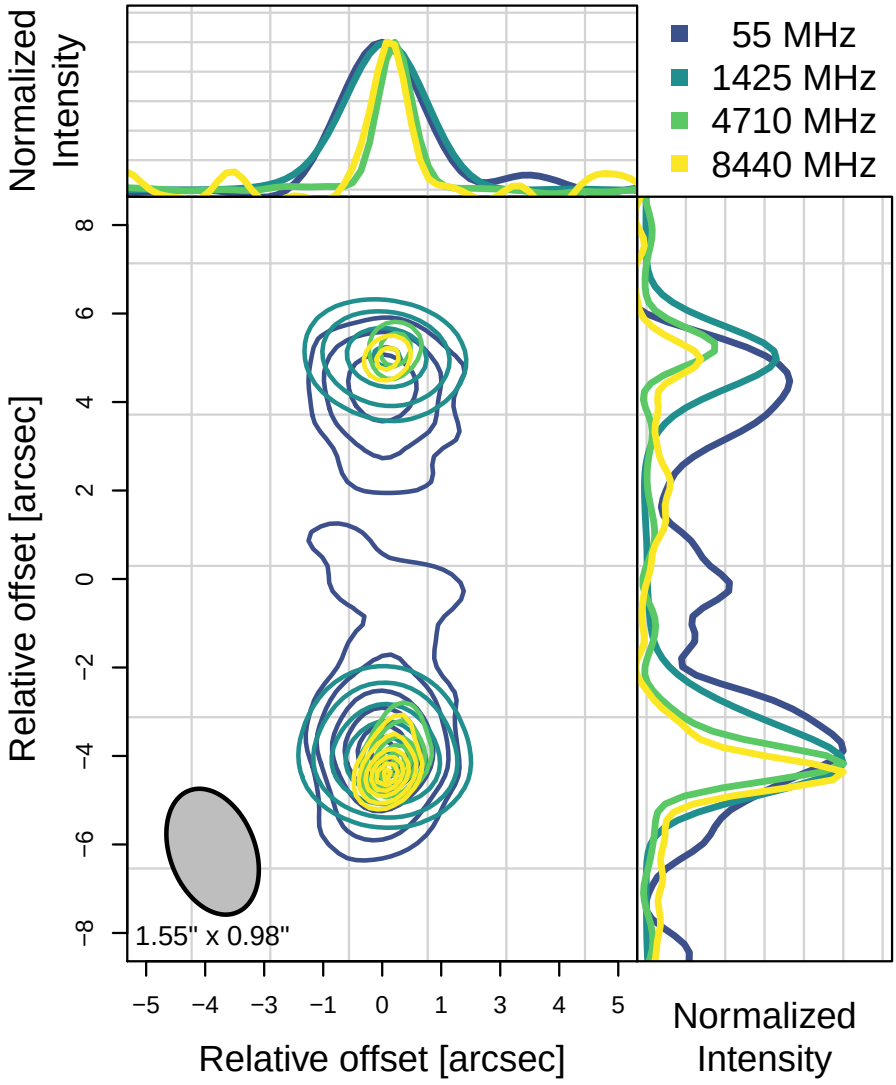

Figure 3.6: Contours and intensity profiles for 4C 43.15 at four frequencies. The rotation angle of the jet was determined per frequency to rotate all images so the jet axis is aligned for all images. The contours are set at 20, 40, 60, 80, and 95 per cent of the maximum intensity (which is unity).

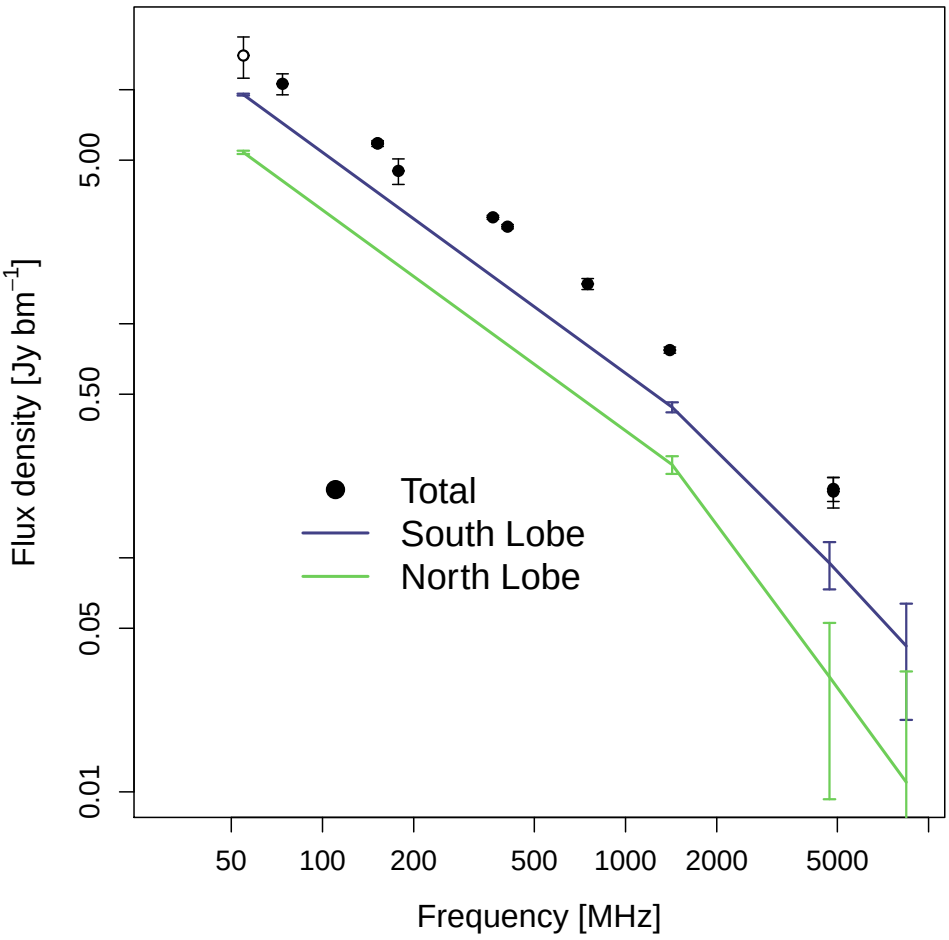

Figure 3.7: The total integrated spectrum derived from archival (black circles) and LOFAR data (white circle with black outline). The integrated spectra of the lobes are also shown for the measurements described in § 3.4.2. The lines between data points do not represent fits to the data and are only drawn to guide the eye.

Table 3.3: Integrated Flux Density Measurements.

Frequency	Flux Density [Jy]	Error [Jy]	Reference
54 MHz	14.9	3.0	This work
74 MHz	10.6	1.1	VLSS, Cohen et al. (2007)
151 MHz	5.9	0.17	6C, Hales et al. (1993)
178 MHz	4.5	0.56	3C, Gower et al. (1967)
365 MHz	2.9	0.056	Texas, Douglas et al. (1996)
408 MHz	2.6	0.056	Bologna, Ficarra et al. (1985)
750 MHz	1.5	0.080	Pauliny-Toth et al. (1966)
1.4 GHz	0.77	0.023	NVSS, Condon et al. (1998)
4.85 GHz	0.19	0.029	Becker et al. (1991)

2. The point-to-point spectral index from 55 MHz to the higher frequencies in this study steepens, i.e. becomes more negative, as the other point increases in frequency. This indicates a break frequency between 55 MHz and 1.4 GHz. This indicates either a steepening at high frequencies, a turnover at low frequencies, or a combination of both. However a low-frequency turnover is not observed in the integrated spectrum. Therefore a steepening of the spectra at high frequencies is more likely, which is seen in Figure 3.7.

3. The northern lobe always has a spectral index as steep or steeper than the lobe regardless of the frequencies used to measure the spectral index. This suggests a physical difference between the two lobes.

These results for the entire spectrum are consistent with a flatter, normal FR II spectral index coupled with synchrotron losses that steepen the spectra at high frequencies and cause a break frequency at intermediate frequencies (Harwood et al., 2016). The spectral index between 55 MHz and 1.4 GHz is $\alpha = -0.95$ for both lobes. We fit power laws to the lobe spectra for frequencies > 1 GHz and found spectral indices of -1.75±0.01 (northern lobe) and -1.31±0.03 (southern lobe). Figure 3.7 shows six measurements of the total integrated spectrum at frequencies less than 500 MHz. The spectral index measured from fitting a power law to these points is $\alpha = -0.83$, which we would expect the lobes to mimic if we had more spatially resolved low-frequency measurements.

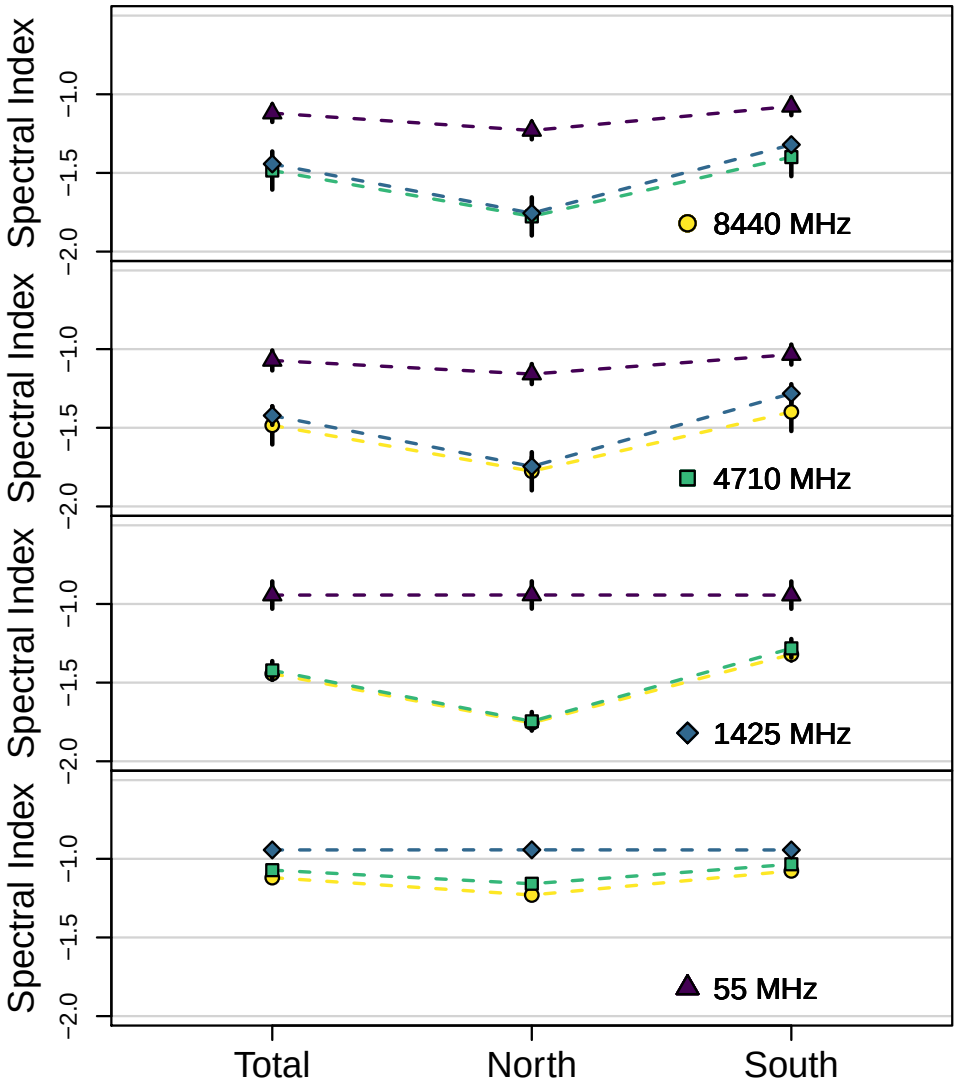

Figure 3.8: The point-to-point spectral index values measured from each frequency to all other frequencies in this study. The symbols in all panels of the plot are as follows: 55 MHz – yellow triangles; 1425 MHz – green diamonds; 4710 MHz – blue squares; 8440 MHz – purple circles.

Table 3.4: Source parameters. Uncertainties in the LOFAR measurement are assumed to be 20 per cent. The optical position was converted to J2000 from the B1950 coordinates in McCarthy (1991): B1950 07:31:49.37 +43:50:59.

	NORTHERN LOBE		SOUTHERN LOBE	
	S_ν [Jy]	Offset from host galaxy	S_ν [Jy]	Offset from host galaxy
55 MHz	5.40±1.1	4.34″	9.53±1.9	4.35″
1.4 GHz	0.25±0.013	4.87″	0.44±0.022	5.03″
4.7 GHz	$0.031\pm1.6\times10^{-3}$	4.52″	$0.095\pm4.8\times10^{-3}$	4.89″
8.4 GHz	$0.011\pm5.5\times10^{-4}$	5.02″	$0.042\pm2.1\times10^{-3}$	4.83″

3.5 Discussion

The main result is that both the general morphology and spectral index properties of 4C 43.15 are similar to FR II sources at low redshift. We have determined that 4C 43.15 has historically fallen on the spectral index – redshift relation because of the steepening of its spectrum at high frequencies, and a break frequency between 55 MHz and 1.4 GHz. The total integrated spectrum has a spectral index of $\alpha = -0.83 \pm 0.02$ for frequencies below 500 MHz, which is not abnormally steep when compared to other FR II sources. For example, the median spectral index for the 3CRR sample is $\alpha = -0.8$ (Laing et al., 1983). The lowest rest frequency probed is 180 MHz, which is still above where low-frequency turnovers are seen in the spectra of local FR II sources (e.g., McKean et al., 2016; Carilli et al., 1991). Thus we expect the break frequency to be due to synchrotron losses at high frequencies rather than a low frequency turnover.

We find no evidence that environmental effects cause a steeper overall spectrum. In fact, the northern lobe, which has the steeper spectral index, is likely undergoing adiabatic expansion into a region of lower density. This is contrary to the scenario discussed by Athreya & Kapahi (1998) where higher ambient densities and temperatures will cause a steeper spectral index. The interaction of 4C 43.15 with its environment will be discussed in detail later in this section.

The observational bias resulting in the initial classification of 4C 43.15 as having an ultra steep spectrum could be a manifestation of different spectral energy losses at high frequencies when compared to local radio galaxies. It is possible that inverse Compton losses, which scale as $(1+z)^4$, combined with spectral ageing, have lowered the break frequency relative to losses from spectral ageing alone. For any two fixed observing frequencies that straddle the break

frequency, a lower break frequency will cause a reduction in the intensity measured at the higher frequency, resulting in a steeper measured spectral index. To model the lobe spectra including the contribution from losses due to the CMB, we require spatially resolved measurements at another low frequency (less than ~ 500 MHz) to unambiguously determine the low-frequency spectral indices of the lobes of 4C 43.15. We plan to use HBA observations of 4C 43.15 to provide measurements at 150 MHz in future studies.

In the following subsections we first calculate the apparent ages of the radio lobes and then look at evidence for environmental interaction.

3.5.1 Ages of the radio lobes

The spectral age can be related to the break frequency ν_{br} and the magnetic field strength B by:

$$\tau_{\rm rad} = 50.3 \frac{B^{1/2}}{B^2 + B_{\rm iC}^2} [\nu_{br}(1+z)]^{-1/2} \text{ Myr} \quad (3.1)$$

(e.g., Harwood et al., 2013, and references therein). The inverse Compton microwave background radiation has a magnetic field strength $B_{\rm iC} = 0.318(1+z)^2$. The units of B and $B_{\rm iC}$ are nT and ν_{br} is in GHz. Using the standard minimum energy assumptions Carilli et al. (1997) derived minimum pressures for the hotspots, which correspond to a magnetic field of 32 nT for 4C 43.15, which is consistent with values for Cygnus A (Carilli et al., 1991). We therefore assume an average value of $B = 1$ nT for the lobes of 4C 43.15, which is consistent with Cygnus A. To calculate $\tau_{\rm rad}$, the break frequency must also be known, and we estimate this from fitting two power laws to integrated flux density measurements: one power low fitted to data at frequencies below 500 MHz, and one power law fitted to data at frequencies above 1 GHz. The frequency at which these two power laws cross is the break frequency.

Using the spectral indices calculated in the previous section, we estimate the break frequencies of the lobes by finding where the low and high frequency fitted power laws cross. The estimated break frequencies for the northern and southern lobes are 947 ± 12 MHz and 662 ± 29 MHz, giving apparent ages of 12.7 ± 0.2 and 15.2 ± 0.7 Myr, respectively. These ages are reasonable for FR II sources of this size (e.g., Harwood et al., 2015).

3.5.2 Environmental interaction

The fact that the observed lobes are not the same is clear: the northern lobe is little more than half as bright as the southern lobe, and has a steeper spectral

index above 1.4 GHz by $\Delta\alpha = -0.5$. We have thus far found that 4C 43.15 is consistent with local FR II sources, and therefore we do not expect an internal difference in physical processes driving the two lobes. This suggests there must be an external cause. Humphrey et al. (2007) found the differences between the lobes in 4C 43.15 to be consistent with orientation effects by modelling Doppler boosting of the hotspots to predict the resulting asymmetry between the lobes for a range of viewing angles and velocities. Although only hot spot advance speeds of $0.4c$ and viewing angles of > 20 deg approach the measured $\Delta\alpha = -0.5$. Since 4C 43.15 is similar to Cygnus A, hot spot advance speeds of $\sim 0.05c$ are much more likely. In this scenario, the models in Humphrey et al. (2007) predict a value for $\Delta\alpha$ at least an order of magnitude smaller than -0.5 for all viewing angles considered. We therefore find it unlikely that orientation is the only cause for the differences between the lobes.

Environmental factors could also cause differences between the lobes. In lower density environments, adiabatic expansion of a radio lobe would lower the surface brightness, effectively shift the break frequency to lower frequencies, and cause a slight steepening of the radio spectrum at higher frequencies. This is consistent with the morphology and spectral index properties of 4C 43.15. The northern lobe is dimmer, appears more diffuse, and has a spectral index steeper than that of the southern lobe. Having ruled out that orientation can explain these asymmetries, this implies that the northern jet is propagating through a lower density medium.

There is supporting evidence for a lower density medium to the North of the host galaxy. Both Lyman-α (Villar-Martín et al., 2003) and Hα+[N II] (Motohara et al., 2000) are seen to be more extended to the North. Figure 3.9 shows the Hα+[N II] overlaid on the radio images for comparison. Qualitatively the emission line gas is more extended and disturbed towards the North, and reaches farther into the area of the radio lobe. Motohara et al. (2000) concluded that the Lyman-α and Hα emission are both nebular emission from gas ionized by strong UV radiation from the central active galactic nucleus. They estimate the electron density of the ionised gas to be $38\,\mathrm{cm}^{-3}$ and $68\,\mathrm{cm}^{-3}$ for the northern and southern regions, respectively. The lower density in the North is consistent with adiabatic expansion having a larger impact on the northern lobe relative to the southern lobe. Naively, the ratios between the integrated flux densities of the lobes and the densities of the environment are similar. However determining the expected relationship between the two ratios requires estimating the synchrotron losses from adiabatic expansion, which requires knowing the relevant volumes and densities, then modelling and fully evolving the spectra. Measuring the vol-

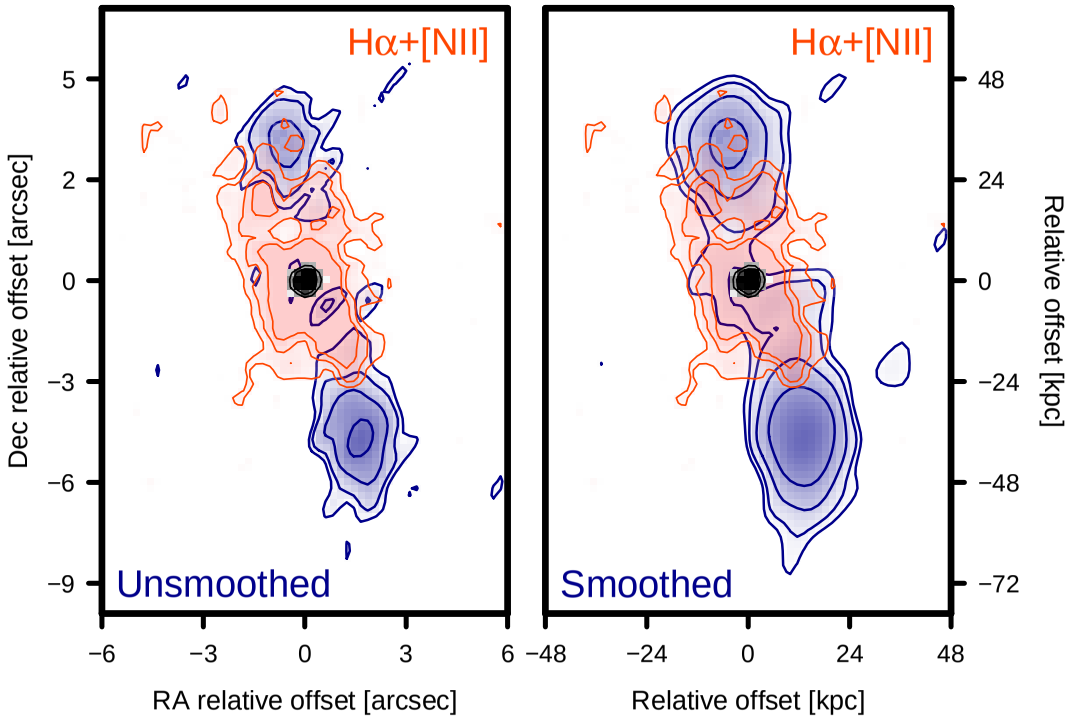

Figure 3.9: The spatial distribution of the radio emission compared with the with K'-band (2.13 μm) continuum from the host galaxy and Hα+[NII] line emission showing cones of ionized gas (Motohara et al., 2000). The two panels show the radio images with the same contours as the images in Figure 3.5 (unsmoothed in the left panel, smoothed in the right panel), overlaid with K'-band continuum in black and Hα+[NII] in red. A separate bright source to the NW has been blanked out.

umes requires knowing the full extent of the radio emission, which is hard to do if the lobe already has low surface brightness due to adiabatic expansion. This complex modelling is beyond the scope of this paper and will be addressed in future studies (J. Harwood, private communication).

3.6 Conclusions and Outlook

We have shown that I-LOFAR LBA is suitable for spatially resolved studies of bright objects. We have presented the first sub-arcsecond image made at frequencies lower than 100 MHz, setting the record for highest spatial resolution at low radio frequencies. This is an exciting prospect that many other science cases will benefit from in the future.

There are two main conclusions from this study of the spatially resolved low frequency properties of high redshift radio galaxy 4C 43.15:

- Low-surface brightness radio emission at low frequencies is seen, for the first time in a high redshift radio galaxy, to be extended between the two radio lobes. The low-frequency morphology is similar to local FR II radio sources like Cygnus A.
- The overall spectra for the lobes are ultra steep only when measuring from 55 MHz to frequencies *above* 1.4 GHz. This is likely due to an ultra-steep spectrum at frequencies ≥ 1.4 GHz with a break frequency between 55 MHz and 1.4 GHz. The low-frequency spectra are consistent with what is found for local FR II sources.

This study has revealed that although 4C 43.15 would have been classified as an ultra-steep spectrum source by De Breuck et al. (2000), this is likely due to a break frequency at intermediate frequencies, and the spectral index at frequencies less than this break is not abnormally steep for nearby FR II sources. Steepening of the spectra at high frequencies could be due to synchrotron ageing and inverse Compton losses from the increased magnetic field strength of the cosmic microwave background radiation at higher redshifts. Unlike nearby sources, we do not observe curvature in the low frequency spectra, which could be due to the fact that we only observe down to a rest frequency of about 180 MHz. Future observations at 30 MHz (103 MHz rest frequency) or lower would be useful.

Larger samples with more data points at low to intermediate frequencies are necessary to determine if the observed ultra steep spectra of high redshift radio galaxies also exhibit the same spectral properties as 4C 43.15. We will use the methods developed for this paper to study another 10 resolved sources with

$2 < z < 4$, incorporating both LBA and HBA measurements to provide excellent constraints on the low-frequency spectra. While a sample size of 11 may not be large enough for general conclusions, it will provide important information on trends in these high redshift sources. These trends can help guide future, large scale studies.

Acknowledgements

LKM gratefully acknowledges financial support from NWO Top LOFAR project no. 614.001.006. LKM and HR acknowledge support from the ERC Advanced Investigator programme NewClusters 321271. RM acknowledges support from the European Research Council under the European Union's Seventh Framework Programme (FP/2007-2013)/ERC Advanced Grant RADIOLIFE-320745. This paper is based (in part) on data obtained with the International LOFAR Telescope (ILT). LOFAR (van Haarlem et al. 2013) is the Low Frequency Array designed and constructed by ASTRON. It has facilities in several countries, that are owned by various parties (each with their own funding sources), and that are collectively operated by the ILT foundation under a joint scientific policy. This research has made use of the NASA/IPAC Extragalactic Database (NED) which is operated by the Jet Propulsion Laboratory, California Institute of Technology, under contract with the National Aeronautics and Space Administration. This research made use of Montage. It is funded by the National Science Foundation under Grant Number ACI-1440620, and was previously funded by the National Aeronautics and Space Administration's Earth Science Technology Office, Computation Technologies Project, under Cooperative Agreement Number NCC5-626 between NASA and the California Institute of Technology. The authors would like to thank J. Harwood and H. Intema for many useful discussions.

CHAPTER 4

Investigating the cause of the $\alpha - z$ relation

"Trying to predict the future is a mug's game. But increasingly it's a game we all have to play because the world is changing so fast and we need to have some sort of idea of what the future's actually going to be like because we are going to have to live there, probably next week."
−Douglas Adams−

Leah K. Morabito, Jeremy Harwood

The correlation between radio spectral index and redshift has long been used to identify high redshift radio galaxies, but its cause is unknown. Traditional explanations invoke intrinsic relations between spectral index and power, environmental differences at high redshift, or higher inverse Compton losses due to the increased photon energy density of the cosmic microwave background. In this paper we investigate whether the increased inverse Compton losses can cause the observed spectral index – redshift correlation by using spectral modelling of nearby radio galaxies to simulate their high redshift equivalents.

Morabito, L. K. and Harwood, J.
In preparation

4.1 Introduction

High redshift radio galaxies (HzRGs) are unique laboratories for studying the formation and evolution of massive galaxies, rich clusters and massive black holes at $z > 2$. They have extended jets on kpc scales that emit synchrotron radiation detectable in the radio regime. The host galaxies have clumpy optical morphologies (Pentericci et al., 2000b) and optical spectra indicative of extreme star formation and large stellar masses. They are often found in protocluster environments (Pentericci et al., 2000b) and are thought to evolve into present-day dominant cluster galaxies (Miley & De Breuck, 2008; Best et al., 1997b). Less than 200 HzRGs are presently known (Miley & De Breuck, 2008), and the highest redshift radio galaxy to date is at $z = 5.19$ (van Breugel et al., 1999).

Almost all of these HzRGs were found by searches for ultra steep spectrum (USS; defined as $\alpha < -1$ where flux density is $S \propto \nu^{\alpha}$) sources in radio surveys. Tielens et al. (1979) first recognized that USS sources were three times less likely to have an optically identified host galaxy, and that their smaller angular sizes implied they were at larger distances. Blumenthal & Miley (1979) found that spectral index did indeed correlate with redshift, with steeper spectral indices associated with objects at higher redshift. Since then, searching for USS sources has been an effective way to identify candidate high redshift sources (e.g., Röttgering et al., 1994) that can be followed up with spectroscopic confirmation.

While the $\alpha - z$ correlation is useful for identifying high redshift galaxies, it is not understood what causes the relation. The traditional explanation is that the observed USS is due to a radio k-correction coupled with the fact that fixed observing frequencies probe higher rest frame frequencies of the radio spectra for higher redshift sources, where steepening due to synchrotron losses is more pronounced. The high-frequency spectra will also be impacted by losses due to inverse Compton scattering of cosmic microwave background (CMB) photons (Krolik & Chen, 1991). Klamer et al. (2006) investigated the rest-frame radio spectra of 37 USS HzRGs with matched-resolution observations spanning $2.3 - 6.2$ GHz and found that the k-correction did not impact the overall relation between spectral index and redshift.

Two alternative explanations have been proposed. The first is that higher ambient density could cause steeper electron energy spectra in the particle acceleration processes at the jet working surfaces. Higher ambient density is expected at higher redshifts, and the radio spectra of HzRGs could therefore be steeper than local radio galaxies (Athreya & Kapahi, 1998; Klamer et al., 2006). The attraction of this explanation is that it could result in both a $\alpha - z$ relation

and a $\alpha-$luminosity relation.

Another explanation is that the $\alpha - z$ relation arises naturally from a correlation between α and luminosity (Chambers et al., 1990; Blundell et al., 1999). For models where higher jet powers produce steeper integrated spectra, when taking Malmquist bias into account no intrinsic relation between $\alpha - z$ is necessary to match observations. It is difficult to study these kinds of effects observationally with flux density limited surveys. Ker et al. (2012) examined the essential relationships amongst power, linear size, redshift, and spectral index for both low and high frequency selected surveys separately, finding only a weak $\alpha - z$ relation which is dominated by the scatter in α. Their findings are consistent with the increasing ambient density at higher redshifts driving the $\alpha - z$ relation.

In this paper we focus on understanding both the cause and the individual selection effects that can impact the $\alpha - z$ relation with a new approach. Using the Broadband Radio Astronomy ToolS software package (BRATS[1]; Harwood et al., 2013, 2015), we fit integrated spectral ageing models to archival radio measurements to produce model radio spectra between 100MHz and 10 GHz. Assuming that HzRGs are similar to their local counterparts (supported by the findings in Morabito et al., 2016), we construct a sample which has no initial dependence between α and z and simulate the sources at higher redshifts to introduce inverse Compton losses and selection effects individually. By doing so we can determine if the observed $\alpha - z$ relation can be reproduced via these effects alone.

In Section 4.2 we describe the initial sample. In Section 4.3 we explain how we use BRATS to model the data, and the introduction of selection effects. Results are presented in Section 4.4 followed by discussion and conclusions in Section 4.5. Throughout the paper we assume a ΛCDM concordance cosmology with $H_0 = 67.8\ \mathrm{km\,s^{-1}\,Mpc^{-1}}$, $\Omega_\mathrm{m} = 0.308$, and $\Omega_\Lambda = 0.692$, consistent with Planck Collaboration et al. (2015).

4.2 Initial Sample

4.2.1 Archival Radio Spectral Energy Distributions

Integrated flux density measurements are required across a wide range of frequencies to perform robust spectral modelling. It is important to capture the behaviour of the radio spectral energy distribution (SED) both at low and high frequencies, in order to fit for any curvature in the overall SED. In practice, this

[1] http://www.askanastronomer.co.uk/brats

generally means a minimum of two flux density measurements at frequencies less than ~ 500 MHz and three measurements above ~ 500 MHz. Extremely low frequencies ($\lesssim$ 100 MHz) can be impacted by free-free absorption and/or synchrotron self-Compton absorption, and will not be well-fitted by spectral ageing models that do not include these physical processes. At frequencies higher than ~ 10 GHz, most sources will be highly resolved and integrated flux density measurements will be unreliable. We therefore construct SEDs over frequencies from ~ 100 MHz to 10 GHz.

We started by searching the NASA/IPAC Extragalactic Database[2] for all objects with $z \leq 1$ and having radio photometry available at 178 MHz. This is the frequency of the 3CRR survey (Laing et al., 1983), which is a 96 per cent complete spectroscopic survey containing the type of bright, jetted radio sources we are interested in. This provided 840 sources, 777 of which had spectroscopic redshifts. We used the new TIFR GMRT Sky Survey Alternative Data Release 1 (TGSS ADR1; Intema et al., 2016) to provide an additional low-frequency measurement at 150 MHz and we cross-matched the 777 NED objects with the TGSS catalogue. There were 259 objects matched within a search radius of 12.5 arcsec (half the size of the average beam size in TGSS).

From the NED flux density measurements we automatically removed individual measurements that were marked as 'peak', 'core', or 'lobe' values. Measurements within 5 MHz of each other were averaged together and their errors added in quadrature. We required that each spectrum have at least two measurements below 500 MHz and three measurements above 500 MHz. There were 155 sources that met this criteria. We visually inspected the SEDs to identify and remove individual aberrant flux density measurements. We also removed 12 flat-spectrum sources, 1 Gigahertz-peaked source, and 5 nearby star-forming galaxies. This left us with a total of 137 sources.

We used BRATS to fit all radio spectra with a continuous injection model (Pacholczyk, 1970) for a range of initial electron energy distributions (injection index), from $\alpha_{inj} = 0.5$ to 1.0 in steps of 0.05. We assume a fixed magnetic field of 1×10^{-9} nT. While there is almost certainly a range of magnetic field strengths within our sample, the radiative losses (hence observed spectral index) are proportional to both the magnetic field strength of the source and the equivalent field of the CMB where $B = \sqrt{B_{lobe}^2 + B_{CMB}^2}$. Due to the equivalent field strength scaling as a function of redshift such that $B_{CMB} = 0.318(1+z)^2$,

[2]The NASA/IPAC Extragalactic Database (NED) is operated by the Jet Propulsion Laboratory, California Institute of Technology, under contract with the National Aeronautics and Space Administration.

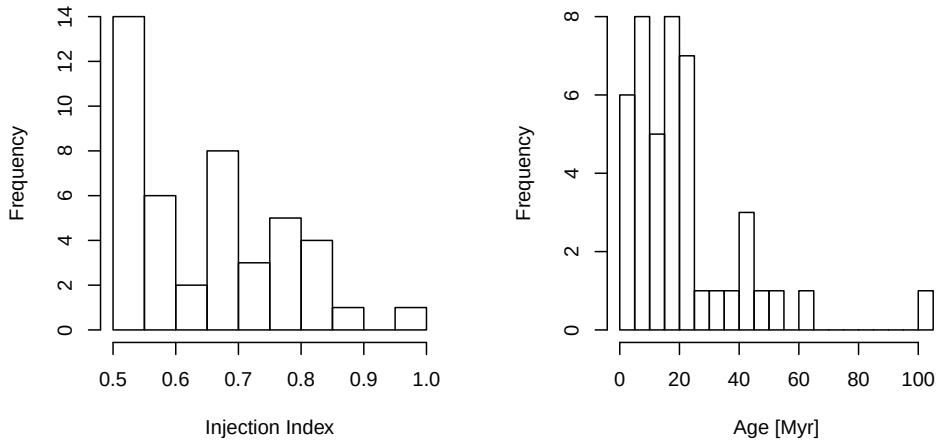

Figure 4.1: Distributions of initial spectral modelling parameters.

it is this term which dominates at high redshifts. It is these sources which most strongly influence the $\alpha - z$ relation and so the effect of any variations in our initial sample should not impact significantly on our overall result.

The output of this spectral modelling includes the spectral age, CMB magnetic field energy density, break frequency in the spectrum, χ^2 of the fit, and confidence level of the fit. Taking only the fits with confidence levels of 1σ, we use the χ^2 values to select the best injection index for each source. We removed two sources because the spectral modelling produced ages consistent with zero. We also removed three sources which were not well-fit due to low-frequency turnovers in their spectra. This left a total of 42 sources in the initial sample, and we show the distributions of parameters associated with the fits in Fig. 4.1.

BRATS also outputs rest frame model spectra, and we use these to measure the $\alpha - z$ relation for our initial sample, which contained only the radio galaxies with $z \leq 1$. De Breuck et al. (2000) calculated α using fixed observing frequencies of 325 or 365 MHz for the low-frequency point, and 1.4 GHz for the high frequency point. Here we use fixed observing frequencies of 325 MHz and 1.4 GHz to calculate α. Fig. 4.2 shows the $\alpha - z$ relation for the initial sample, using the rest-frame model spectra. A linear fit to the data shows the slope is 0.033 ± 0.071, which is consistent with zero.

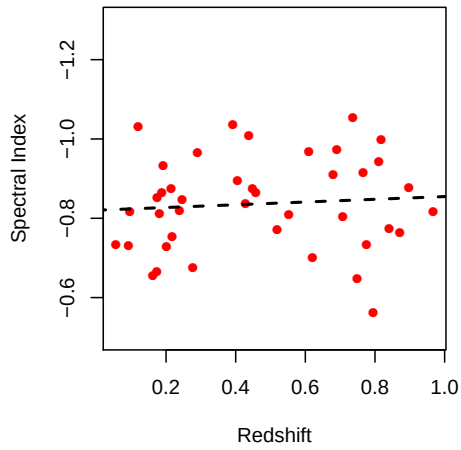

Figure 4.2: The $\alpha - z$ relation for the initial sample, which is limited to $0.1 \leq z \leq 1$. A linear fit to the data (red line) shows a slope of 0.033 ± 0.071, which is consistent with zero.

4.2.2 Constructing a High-redshift Sample

We construct a high-redshift sample by using the observed distribution of redshifts from De Breuck et al. (2000). We fit a power-law to the observed redshift distribution and use the acceptance-rejection method to simulate 10^6 redshifts consistent with this distribution (Fig. 4.3). Drawing from the simulated redshift distribution, we assign redshifts randomly to sources in our initial sample, taking care to match the observed redshift distribution. Some of the sources from our initial sample are used more than once, to match the total number of sources in the observed sample.

4.3 Modelling the Selection Effects

4.3.1 *k*-correction

The first selection effect we model is the *k*-correction. For this, we simply take the high-redshift sample and *k*-correct the rest-frame spectra to the observed frame using the simulated redshifts. We then measure the observed model spectra at fixed frequencies of 325 MHz and 1.4 GHz, and perform a linear fit to measure the slope of the relation between α and z. The redshift distribution and observed α-z relation are shown in Fig. 4.3. The linear fit to the data shows the slope of the relation is now 0.041 ± 0.010, which is slightly steeper but still consistent with the initial sample (within the uncertainties).

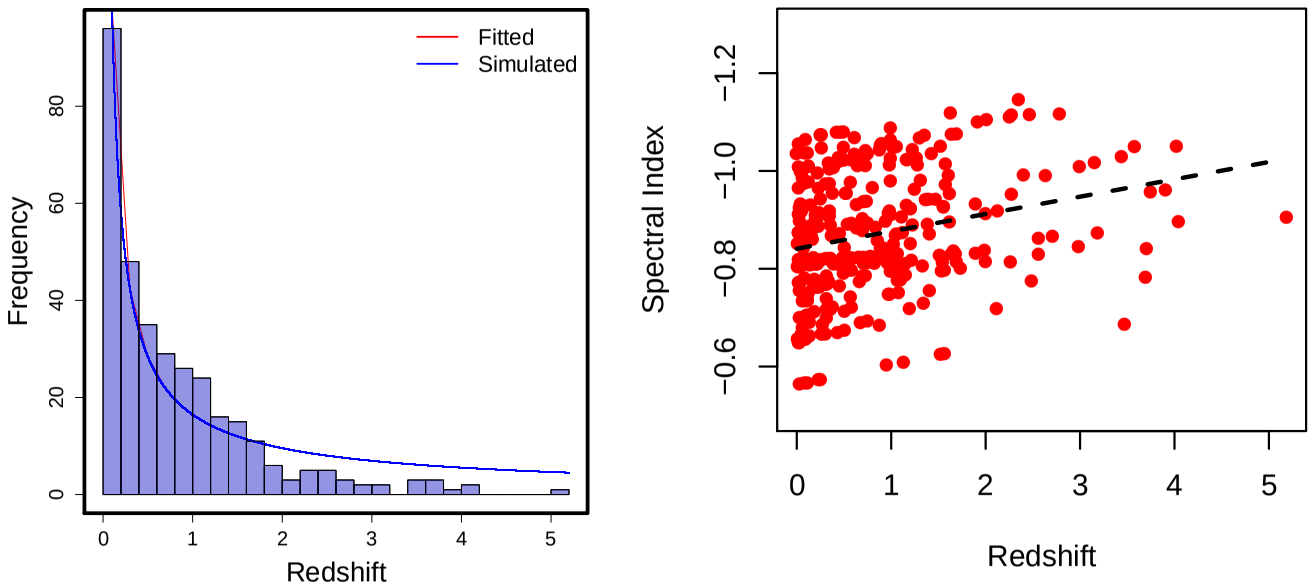

Figure 4.3: *Left:* The redshift distribution from De Breuck et al. (2000). The red line is a fit to the redshift distribution, and the blue line shows our simulated redshifts. The redshifts for the simulated sample are drawn from the simulated distribution, taking care to match the redshift distribution in the De Breuck et al. (2000) sample. *Right:* The sample of local galaxies that have been k-corrected with their simulated higher redshifts, drawn from the redshift distribution on the left.

4.3.2 Inverse Compton from CMB

To model the inverse Compton scattering from CMB photons, we take the rest-frame high redshift spectra and fix the ages and injection index from the initial BRATS models. We again perform spectral fitting using BRATS, but this time using the simulated redshifts, which introduces the $B_{\rm iC}$ term due to the inverse Compton scattering from the CMB. Fixing the ages insures that the only difference in the resultant model spectra is the effects of inverse Compton scattering. We again k-correct the rest-frame model spectra to the observed frame and measure the spectral index between 325 MHz and 1.4 GHz.

4.3.3 Observational Biases

To compare with the sample from De Breuck et al. (2000) we must be careful to use only objects from the simulated sample that would satisfy the selection effects in the observed sample. The 3CR and MRC samples are complete down to their flux density limits, but De Breuck et al. (2000) use other samples of USS sources selected from larger, incomplete samples. We therefore select objects to be included in the 'observed' simulated sample if they satisfy either of the following criteria:

- The source is above the flux density limit of the 3CR sample (10 Jy) with a redshift $\leq z_{max}$ of the 3CR sample ($z_{max} = 2.474$).
- The source is above the flux density limit of the 4C sample (2 Jy) with a spectral index at least as steep as $\alpha = -1.03$, the limiting spectral index for this sample in De Breuck et al. (2000).

4.4 Results

We plot the final results in Fig. 4.4. Shown in the figure are the observed sample from De Breuck et al. (2000), the entire high-redshift sample with inverse Compton effects modelled in the spectra, and the sample which also matches the selection criteria described in the last section. The linear fits of the simulated sample matching the selection criteria and the observed sample are also shown. We find $\alpha = -(0.16 \pm 0.0090)z - 0.79 \pm 0.0096$ for the simulated sample including selection effects and $\alpha = -(0.16 \pm 0.018)z - 0.75 \pm 0.021$ for the observed sample. These relations are consistent with each other within the uncertainties, and we find that the inverse Compton scattering from the CMB photons can entirely explain the $\alpha - z$ relation without invoking any environmental or intrinsic differences at high redshift.

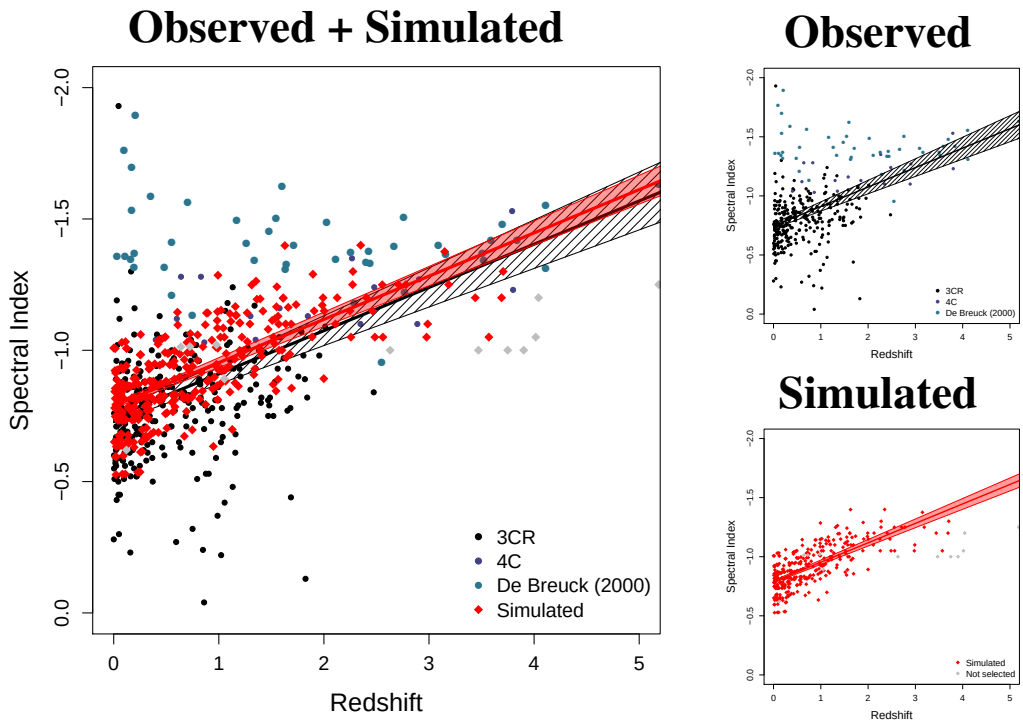

Figure 4.4: The $\alpha - z$ for the observed and simulated samples. The large panel on the left shows both observed and simulated samples together, while the panels on the right show the observed (*top*) and simulated (*bottom*) samples separately. The black points are from the 3CR survey, the dark blue points are from the 4C survey, and the points are the new additions of De Breuck et al. (2000). A linear fit to the observed sample is shown by the black line, with the hatched area representing the fit errors. The simulated data which meet the selection criteria explained in Section 4.3 are plotted as red diamonds, with a linear fit shown by a red line with the corresponding uncertainties in the shaded red area. Gray points are the simulated data that did not meet the selection criteria.

The scatter of measured spectral indices in the simulated sample is smaller than that in the observed sample, as evident in Fig. 4.4, but the fitted relations still agree at low redshift. At $z \leq 2$ this is partially due to our assumption of a single magnetic field strength, but also note that the USS objects at low redshift come from a positive bias, i.e., searches for USS objects in large, incomplete surveys. The scatter in our simulated sample is more comparable to the scatter in the 3CR survey, which is complete.

4.5 Discussion and Conclusions

In this paper we have used spectral modelling of a sample of local bright radio sources to simulate HzRGs and show that the observed $\alpha - z$ relation can be entirely reproduced by a combination of inverse Compton scattering from the CMB and selection effects. One final selection effect to consider in this analysis is that the sizes of radio galaxies decrease with increasing redshift (e.g., Morabito et al. 2016, Neeser et al., 1995). There is also a dependence of integrated spectral index on size, which Ker et al. (2012) have quantified as $\alpha = -0.07\mathrm{D} - 0.94$. Assuming the evolutionary dependence is $D \propto (1+z)^{-n}$ with $n = 1.99^{+0.25}_{-0.27}$ (Morabito et al., in preparation), the spectral index would tend to flatten towards higher redshift, but only by $\Delta\alpha \lesssim 0.1$ at $z = 5$. This is consistent with the differences we see in the simulated and observed samples.

We conclude that the $\alpha - z$ relation can be explained entirely by the enhanced inverse Compton losses at higher redshift, coupled with selection effects that are biased towards selecting USS sources from incomplete surveys. The $\alpha - z$ relation is still useful for finding candidate high-redshift galaxies, but we note that perhaps more high redshift sources could be found by relaxing the strict USS criteria to $\alpha < -0.9$ or < -0.8, and coupling the selection with size as suggested by Ker et al. (2012).

Acknowledgements

LKM acknowledges financial support from NWO Top LOFAR project, project n. 614.001.006.

CHAPTER 5

Discovery of Carbon Radio Recombination Lines in M82

"Though that, of course, was merely a discovery. It was there to be discovered."
−Douglas Adams−

Carbon radio recombination lines (RRLs) at low frequencies ($\lesssim 500$ MHz) trace the cold, diffuse phase of the interstellar medium, which is otherwise difficult to observe. We present the detection of carbon RRLs in absorption in M82 with LOFAR in the frequency range of $48-64$ MHz. This is the first extragalactic detection of RRLs from a species other than hydrogen, and below 1 GHz. Since the carbon RRLs are not detected individually, we cross-correlated the observed spectrum with a template spectrum of carbon RRLs to determine a radial velocity of 219 ± 9 km s^{-1}. Using this radial velocity, we stack 22 carbon-α transitions from quantum levels $n = 468-508$ to achieve an 8.5σ detection. The absorption line profile exhibits a narrow feature with peak optical depth of 3×10^{-3} and FWHM of 31 km s^{-1}. Closer inspection suggests that the narrow feature is superimposed on a broad, shallow component. The total line profile appears to be correlated with the 21 cm H I line profile reconstructed from H I absorption in the direction of supernova remnants in the nucleus. The narrow width and centroid velocity of the feature suggests that it is associated with the nuclear starburst region. It is therefore likely that the carbon RRLs are associated with cold atomic gas in the direction of the nucleus of M82.

Morabito, L. K., Oonk, J. B. R., Salgado, F., Toribio, M. C., Röttgering, H. J. A., Tielens, A. G. G. M., et al.
2014, ApJL, 795, L33

5.1 Introduction

The nearby (3.52 ± 0.02 Mpc; Jacobs et al., 2009) nuclear starburst galaxy M82 has been observed to host a wide range of phases of the interstellar medium (ISM). Observations of disrupted H I within the disk show that the neutral gas is more concentrated in the nuclear region (Yun et al., 1993). There is a rotating ring of molecular gas in the nucleus, as seen from observations of HCN, HCO+, CO(2-1) (Kepley et al., 2014), OH (e.g., Argo et al., 2010), and CO images (e.g., Westmoquette et al., 2013). Numerous H II regions are seen (e.g., McDonald et al., 2002; Gandhi et al., 2011) in this area. The nuclear region is also studded with compact, bright supernova remnants (SNRs; e.g., Muxlow et al., 1994; Fenech et al., 2010). The spectral turnovers of the SNRs (Varenius et al., in prep., Wills et al., 1997) as well as the overall spectrum (Varenius et al., in prep., Adebahr et al., 2013) indicate the presence of free-free absorption by ionized gas. The complex interplay of all these components of the ISM is not fully understood.

Carbon radio recombination lines can help characterize the cold, diffuse phase of the interstellar medium (ISM). When free electrons recombine with atoms at quantum numbers $n \gtrsim 50$, the decreased energy spacing of subsequent levels produces radio recombination lines (RRLs). By comparing observations of RRLs with detailed physical models, we can determine information on the physical properties, such as electron temperature and density, of the gas in which the RRLs originate (e.g., Salgado et al., in preparation; Walmsley & Watson, 1982; Shaver, 1975a; Dupree, 1969). At frequencies $\lesssim 500$ MHz, RRLs are spaced closely enough that wide-bandwidth instruments like the Low Frequency Array (LOFAR; van Haarlem et al., 2013) are able to track the dependence of line properties on quantum number within a single observation. These properties make RRLs a powerful tool for determining the temperature and density of their host phases of the ISM.

RRLs fall into two categories: discrete and diffuse. Discrete RRLs trace warm ($T_e \sim 10^4$ K), high-density ($n_e > 100$ cm^{-3}) gas associated with H II regions (Palmer, 1967). They are predominantly seen at frequencies above $\sim$ 1 GHz and originate from hydrogen, helium, and carbon (e.g., Poppi et al., 2007; Konovalenko & Stepkin, 2005; Roelfsema & Goss, 1991). These types of RRLs have been detected in a handful of nearby bright star-forming galaxies (e.g., Shaver et al., 1977; Anantharamaiah et al., 1993; Rodriguez-Rico et al., 2004; Roy et al., 2008).

Diffuse carbon RRLs (CRRLs) trace the cold neutral medium (CNM), which is cold ($T_e \sim 100$ K), and diffuse ($n_e \lesssim 0.1$ cm^{-3}). Diffuse RRLs are observed

at frequencies below 1 GHz. Typically the CNM has ionization levels that are too low to produce hydrogen and helium lines, and only CRRLs are observed. The ionization energy for atomic carbon is only 11.3 eV, lower than that of hydrogen, 13.6 eV. Some photons that can escape H II regions can therefore ionize carbon, and thus C II is expected to be the dominant state of carbon in the ISM. While discrete RRLs are used extensively to study star forming regions (e.g., Anderson et al., 2011; Roelfsema et al., 1992), not much is yet known about the CNM associated with diffuse RRLs, even in our Galaxy. Low frequency observations have shown that the CRRL emitting and absorbing gas is prevalent on scales of degrees along the Galactic plane (Erickson et al., 1995; Kantharia & Anantharamaiah, 2001). Pinhole studies in the direction of H II regions (e.g., Golynkin & Konovalenko, 1991), supernova remnants (Cassiopeia A; e.g., Asgekar et al., 2013; Payne et al., 1989; Konovalenko & Sodin, 1981) or bright background extragalactic sources (Oonk et al., 2014) have detected CRRLs on smaller scales. The new Low Frequency Array (LOFAR; van Haarlem et al., 2013) has observed CRRLs in our Galaxy. Over the next several years, LOFAR will perform a CRRL survey of the Galactic plane, on scales from degrees down to several arcseconds, producing maps that will provide a comprehensive picture of the Galactic CNM by quantifying the average gas temperatures and densities, as well as abundances.

In this paper, we present the first detection of extragalactic CRRLs, observed in M82 at frequencies near 60 MHz with LOFAR. This is the first extragalactic detection of diffuse RRLs, and the first extragalactic detection of RRLs from a species other than hydrogen. This detection opens up the possibility of tracing the evolution of the CNM through all stages of galaxy formation.

Section 5.2 outlines observations, data reduction, and imaging. Section 5.3 describes the extraction and processing of the spectra, cross-correlation of the overall spectrum to determine a velocity, and subband stacking to achieve a detection. Results are presented in § 4. Discussion and conclusions follow in § 5.5 and § 5.6, respectively.

5.2 Observations and Data Reduction

M82 was observed with a total on-source time of 5.0 hours on 21 February 2013 with the LOFAR low-band antenna (LBA; 10 − 80 MHz) stations, as part of early science (Cycle 0) data obtained for the LOFAR Survey of nearby galaxies (LC0_043, PI: R. Beck). We used 13 remote and 24 core stations for this observation, giving baselines between 90 m and 85 km. Each LBA station contains 96 dual polarization dipole antennas, 48 of which can be used simultaneously,

and has a total radius of 87 m. We used the LBA_OUTER configuration, where the outermost more sparsely spaced 48 antennas in each station record data. This configuration has a reduced field of view compared to other configurations, and mitigates the problem of mutual coupling between closely spaced antennas, providing slightly increased sensitivity.

Each dual-polarization dipole antenna provides four linear correlation products which were used to reconstruct Stokes I images. We obtained complete frequency coverage between 30 and 78 MHz with 1 s time resolution. This bandwidth was divided in 244 subbands, each 0.1953 MHz wide, and further subdivided into 128 channels, resulting in channel widths ranging from $6-16$ km s^{-1}. Using the total available bandwidth of 488 subbands and the multibeam capability of LOFAR we simultaneously observed the calibrator source 3C196 with identical frequency coverage.

The calibrator data were processed by the observatory pipeline, starting by flagging radio frequency interference (RFI) with the AOFlagger (Offringa, 2010). Typically, a few percent of the data were flagged due to RFI, consistent with a study of the LOFAR RFI environment (Offringa et al., 2013). The calibrator data were then averaged to 16 channels and 6 seconds before calibration with the BlackBoard Selfcal software system (Pandey et al., 2009). The target data were flagged with the AOFlagger, averaged to 6 seconds and 32 channels and the amplitude calibration obtained from 3C196 was applied. The velocity sampling of the individual subbands in target data after averaging ranges from $29-37$ km s^{-1}.

For imaging we selected only the 24 LOFAR core stations, which all observe with the same clock, making correction for time delays unnecessary. The proximity of the stations to each other also mitigates the chance of observing the target through severely different ionospheric conditions. Image cubes of a region with an area of 6×6 degree^2 centred on M82 were made with AWimager (Tasse et al., 2013), imaging and cleaning each channel individually. We used Briggs weighting (Briggs, 1995) with a robust value of 0.0 to create images with resolutions ranging between 259×340 arcsec^2 and 322×425 arcsec^2. At this resolution M82 is unresolved. Low resolution imaging parameters were deliberately chosen to speed up the computationally expensive imaging process. LOFAR does not support Doppler tracking so we have Doppler-corrected the data post imaging. In total we imaged 69 subbands in the range 50-64 MHz, centred on the peak response of the LBA (van Haarlem et al., 2013).

5.3 Spectral Processing

5.3.1 Individual subband processing

We extracted the spatially integrated spectra from elliptical apertures, where the appropriate elliptical dimensions in each subband were determined by fitting a 2D Gaussian to the point source in the centre and using the curve-of-growth (see Fig. 5.1) to select an aperture size that captured the total flux density of the point source but did not include nearby background sources. We calculated the standard deviation for each subband and implemented automatic removal of subbands with excessively large standard deviations ($\geq 10 \times \sigma_{\mathrm{median}}$), verified by visual inspection. Five subbands were removed from further processing. We inspected each subband for individual detections of lines, which were not seen. In order to increase the signal-to-noise ratio, we stacked CRRL α-transitions ($\Delta n = 1$, for $468 < n < 508$) to form an average line profile.

5.3.2 Measuring the velocity/redshift

Maximizing the signal-to-noise ratio of a stacked line profile requires precisely stacking the centres of each individual line, which requires an accurate radial velocity (redshift). While the systemic velocity of M82 has been measured as $210 \pm 20\,\mathrm{km\ s^{-1}}$ relative to the local standard of rest (LSR), observations show that even in the nuclear region there is a spread of $\sim 200\,\mathrm{km\ s^{-1}}$ in velocity (e.g., Wills et al., 1998; Kepley et al., 2014). We constrained the velocity for the CRRL absorbing gas by cross-correlating a spectral template of CRRLs (using Gaussian line profiles at known CRRL frequencies) with the entire observed spectrum over a range of redshifts. The template line peaks were normalised to a value of 3×10^{-3}. For the less certain line width parameter, we ran a series of models with different line widths, starting at $v = 15\,\mathrm{km\ s^{-1}}$ (to avoid cross-correlating with noise peaks). The magnitude of the cross-correlation peaks at $v = 210\,\mathrm{km\ s^{-1}}$ relative to the LSR (optical velocity), and we iterated with a template that only contains subbands for which rest-frame CRRLs would appear at this redshift. This reduces the amount of noise which is cross-correlated, very slightly improving the definition of the peak of the cross-correlation.

Figure 5.2 shows a clear peak in the cross-correlation at $v = 219\,\mathrm{km\ s^{-1}}$ ($z = 0.00073 \pm 0.00003$), consistent with the systemic velocity of M82, and we used this to stack our lines. We did not find evidence for CRRL features at either of the velocities of the two secondary peaks, $v = 168\,\mathrm{km\ s^{-1}}$ and $v = 255\,\mathrm{km\ s^{-1}}$.

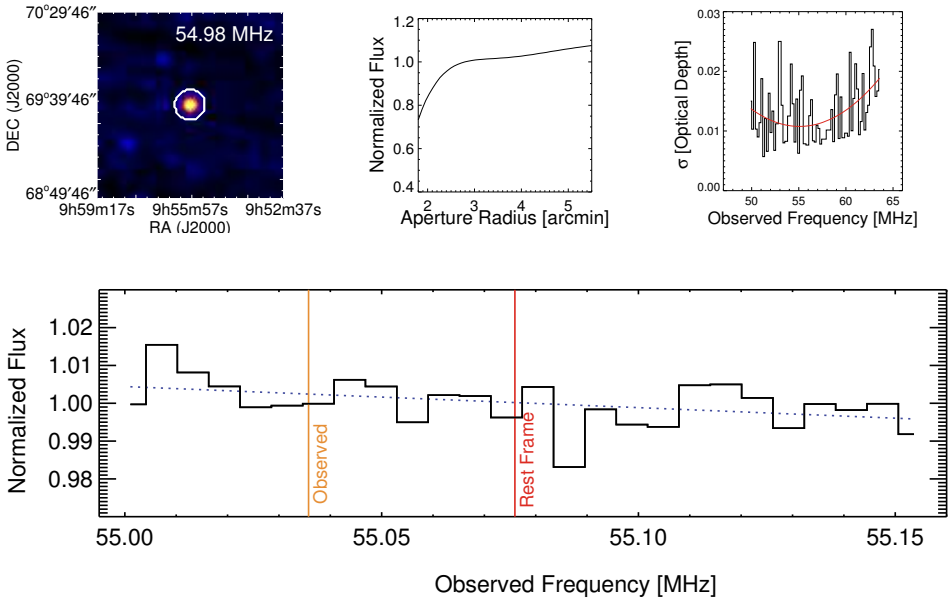

Figure 5.1: A demonstration of the spectral extraction process. The top left panel shows the centre of an image obtained by averaging all channels maps within one subband, with a white contour marking the extraction aperture (diameter ~ 15 arcmin). The top centre panel shows the curve-of-growth for the same subband used to determine the size of the aperture. The top right panel shows the optical depth standard deviation as a function of subband (frequency), with excessively noisy subbands filtered out. The bottom panel displays the normalised raw extracted spectrum for the same subband as the top left and center panels. A linear fit is overplotted as a blue dotted line, and observed and rest frame ($z = 0.00073$) frequencies of the α-transition CRRL in this subband are labelled.

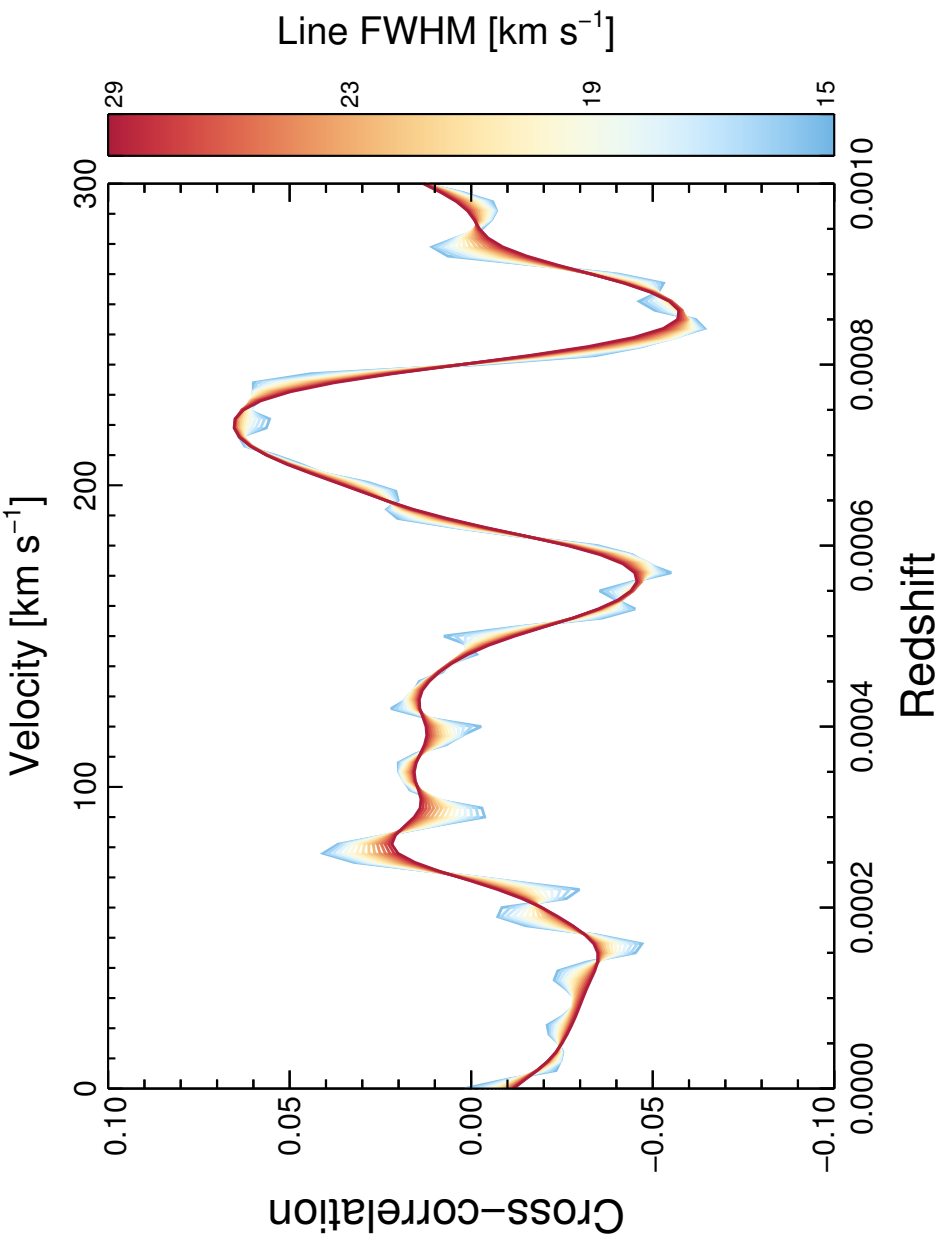

Figure 5.2: Cross-correlation values versus redshift. Larger absolute values indicate a higher correlation between the template and observed spectra.

5.3.3 Reconstructing the Line Profile

Requiring that rest-frame CRRL frequencies be at least six channels away from the edge of a subband to avoid problems with noisy edge channels, we find that twenty-three subbands have α-transitions. We clipped the first and last three edge channels and converted to optical velocity using the rest frequency of the CRRL within the subband. After blanking $\pm 50\,\mathrm{km\,s^{-1}}$ around the expected velocity of the CRRL, we fitted the continuum in each subband individually with a low (first or second) order polynomial. We also tried blanking different ranges around the line, from ± 50 to $\pm 250\,\mathrm{km\,s^{-1}}$, without seeing substantial differences in the final spectrum. For one subband, any blanking left continuum only on one side of the line, so we did not include this subband in the final stack. Each subband was continuum subtracted. The final spectrum was constructed from the individual points of 22 subbands, see Fig. 5.3.

The final stacked spectrum has a velocity sampling of $\sim 1.5\,\mathrm{km\,s^{-1}}$ within approximately $\pm 150\,\mathrm{km\,s^{-1}}$ of the measured velocity ($219\,\mathrm{km\,s^{-1}}$, LSR). The measurement error of each point is equal to the standard deviation of the continuum in the subband from which the point originates. The weighted standard deviation of the continuum in the final spectrum within approximately $\pm 150\,\mathrm{km\,s^{-1}}$ of the expected CRRL line centre is $\sigma_\tau = 0.005$, which is approximately $\sqrt{22}$ smaller than the average noise in a subband.

Galactic CRRLs show peak optical depths of $10^{-3} - 10^{-4}$ (e.g., Kantharia & Anantharamaiah, 2001; Konovalenko & Sodin, 1981). If the CRRLs in M82 have similar peak optical depths then these would be within the noise of this spectrum. We therefore used a low-pass Savitzky-Golay filter (SGF; Savitzky & Golay, 1964) which is a special case of a least-squares (LS) smoothing function that convolves the data with a filter whose shape is dependent on the polynomial order used for fitting. Other filtering methods (see Fig. 5.4) produced similar line profiles. After testing SGF filter widths from 15 to 60 data points for both first and second order polynomials, we selected an SGF with a width of 31 data points, which provided the flattest continuum. Within approximately $\pm 200\,\mathrm{km\,s^{-1}}$ of the feature in the final, smoothed spectrum, the standard deviation of the continuum is $\sigma_\tau = 3.3 \times 10^{-4}$, in good agreement with our expectations from the raw spectrum noise and filter window size. We assessed this filtering method with modelled spectra and found that the integrated line profile is preserved within the errors even after introducing Gaussian noise.

Radial velocities within the nuclear region range from $\sim 120 - 300\,\mathrm{km\,s^{-1}}$. The centroid of the CRRL feature is therefore consistent with an absorption feature associated with the centre of the nuclear region. The cross-correlation is

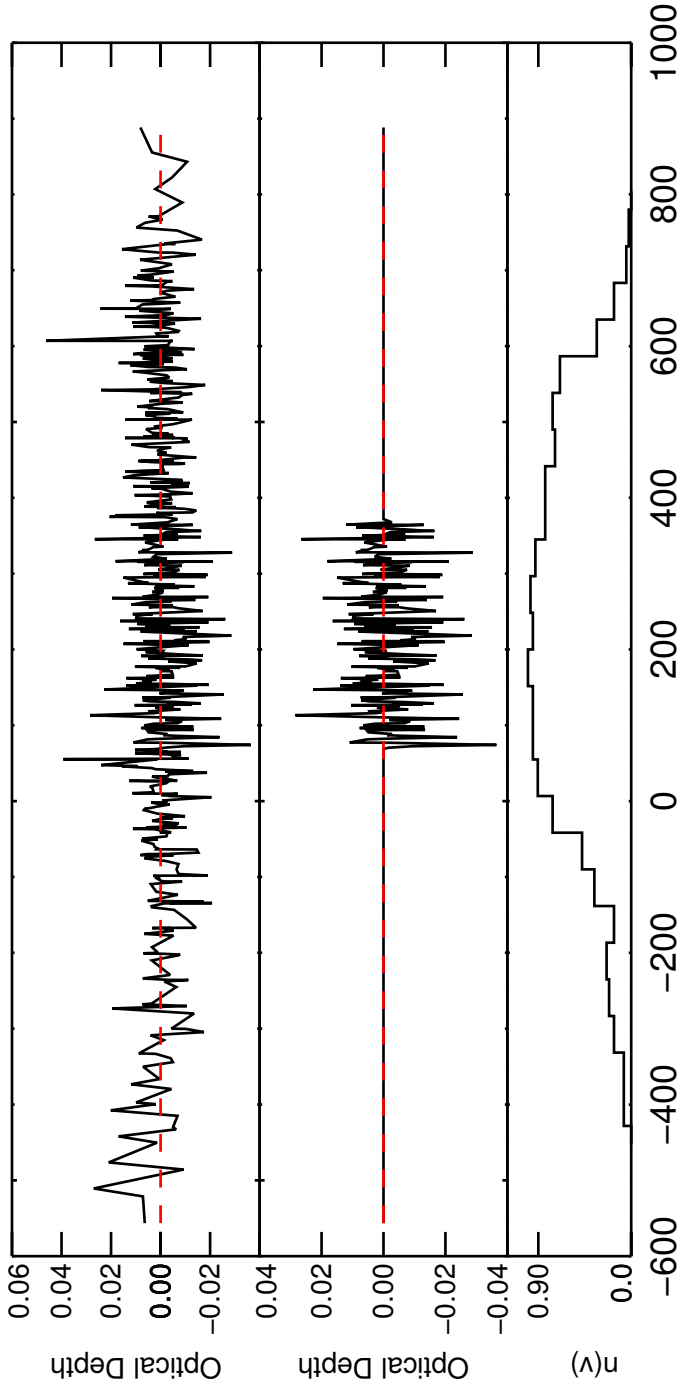

Figure 5.3: The stacked spectrum with the expected CRRL feature at the measured systemic velocity of v = 219km s^{-1}. From top to bottom: the complete reconstructed spectrum; the portion of the spectrum with dense velocity coverage; the normalised density of points in the spectrum. The red dashed line in the top two panels represents the continuum.

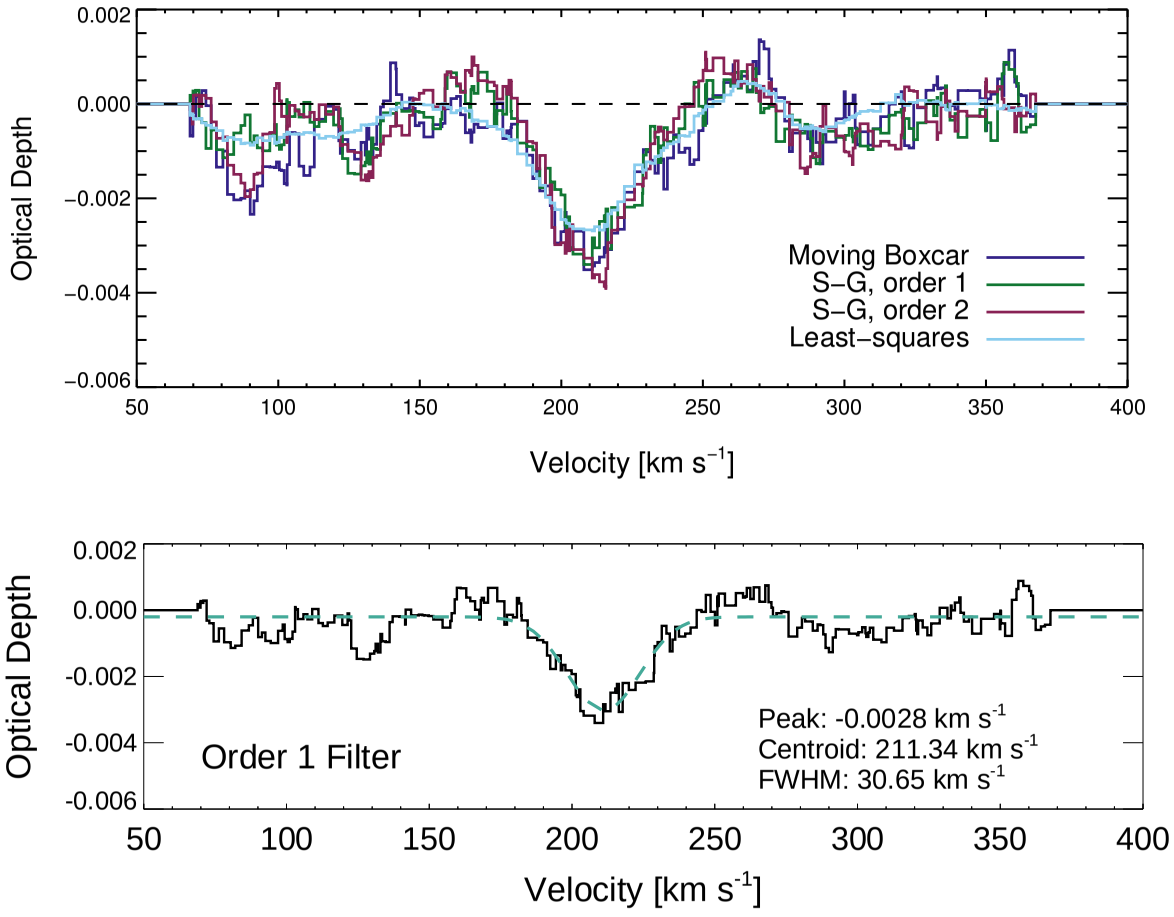

Figure 5.4: Top: Different methods of smoothing the noise. The various methods provide similar line profiles. Bottom: The final spectrum, fitted with a Gaussian profile.

already strong evidence that the feature does not arise merely from a chance alignment of noise, since the feature only arises from a location where we know there to be gas, which is necessary but not sufficient for CRRLs. To rule out other possibilities, we conducted a series of tests. We used a 'jack-knife' procedure where we re-stacked the subbands, each time leaving out an individual subband. None of the stacks produced a significant change to the absorption feature, confirming that the stacked spectrum is not dominated by one subband. Additionally, we stacked the subbands after introducing random velocity shifts to each subband before stacking, and were unable to produce any credible features. Spectra extracted from the background sky also do not show an absorption feature when stacked. From these tests, we conclude that our feature is real and associated with the M82 starburst galaxy.

We tried to detect CRRL β-transitions ($\Delta n = 2$), without success. This is not unexpected, as the CRRL β-transitions are expected to have integrated optical depths that are only $15-30\%$ that of the α-transitions (e.g., Stepkin et al., 2007; Payne et al., 1989). We did not find evidence for local CRRLs at $z = 0$. A search for hydrogen RRLs, both locally and at the redshift of M82, was also unproductive. This is unsurprising as these are believed to be very weak at these frequencies (e.g., Salgado et al. in preparation; Shaver, 1975a).

5.4 Results

We stacked the spectra to search for CRRLs in M82 using our measured velocity, $v = 219\,\mathrm{km\ s^{-1}}$, and detect carbon α-transition RRLs with a combined signal-to-noise ratio of 8.5σ in the filtered spectrum. The central absorption feature can be fitted by a four parameter Gaussian profile with a depth of $2.8^{+0.12}_{-0.10} \times 10^{-3}$, a FWHM of $30.6^{+2.3}_{-1.0}$ km s^{-1}, a centre of $211.3^{+0.7}_{-0.5}$ km s^{-1}, and an additive offset of $-2^{+0.012}_{-0.072} \times 10^{-4}$ (see Fig. 5.4).

5.5 Discussion

Other absorption features have been observed in M82 with similarly narrow widths. Weiß et al. (2010) observed p-H_2O absorption (in the far infrared) with a FWHM of $60\,\mathrm{km\ s^{-1}}$, although this is offset from the CRRL absorption by $\sim 50\,\mathrm{km\ s^{-1}}$. Additionally, a narrow component results if we limit the reconstruction of the H I absorption profile in the direction of SNRs in the nucleus of M82 to only the handful of bright SNRs which are relatively unaffected by free-free absorption at low frequencies. We constructed the H I absorption line profiles from measurements in Wills et al. (1998). We interpolated the spectra

(mJy/bm) in the direction of each of the 26 SNRs which show H 1 absorption onto a velocity grid with 1 km s^{-1} resolution using a cubic spline function. Addition of the individual spectra produces a combined spectrum with information in the direction of SNRs. For the low frequency spectrum, we cross matched the SNRs in Table 1 of Wills et al. (1998) with those still seen by LOFAR at 154 MHz (Varenius et al., in preparation). The eight SNRs from Wills et al. (1998) that have measured H I absorption and are > 1 mJy at 154 MHz are listed in that paper as 39.10+57.3, 39.40+56.1, 39.77+56.9, 42.53+61.9, 43.31+59.2, 45.74+65.2, 45.89+63.8, and 46.52+63.9.

Both of these absorption profiles show broader, shallower structure to either side of a deep, central feature, of which we see hints in the reconstructed CRRL profile (see Fig. 5.5). Galactic observations show a correlation between CRRLs and H I (e.g., Kantharia & Anantharamaiah, 2001; Payne et al., 1989), so it is unsurprising that this correlation would also be present in M82.

As Fig. 5.5 illustrates, integration of other tracers of interstellar gas over the disk of M82 leads to FWHM in excess of 200 km s^{-1} (Kepley et al., 2014; Wills et al., 1998). This leads us to expect a broad component of the CRRL profile, although the signal to noise coupled with the fixed velocity coverage and location of CRRLs in the subbands makes this difficult to ascertain. The overall CRRL profile follows the low-frequency H I line profile (Fig. 5.5). This shows that the CRRL absorbing gas is preferentially observed in front of those continuum sources that are still bright at low frequencies. The continuum offset and low-level absorption features in the CRRL spectrum also show reasonable agreement with the H I absorbing gas, indicating that possibly we are observing a widespread CRRL component associated with cold, diffuse H I throughout M82.

Integrating the line profile gives $\int \tau_{\rm CII} {\rm d}\nu = 21.3\,{\rm s}^{-1}$. To constrain physical parameters of the gas, i.e. temperature and density, a single measurement is not enough. Additional measurements at higher frequencies (100-400 MHz) are necessary.

5.6 Conclusions

We have presented the first detection of extragalactic carbon radio recombination lines, in M82, using early science (Cycle 0) observations with LOFAR. While we already know that cold, neutral gas exists in M82 from H I measurements, this is the first independent measurement of the atomic CNM. The narrow CRRL line is at a velocity corresponding to the centre of M82 and the profile corresponds to the absorption feature seen in the H I spectrum. Higher resolu-

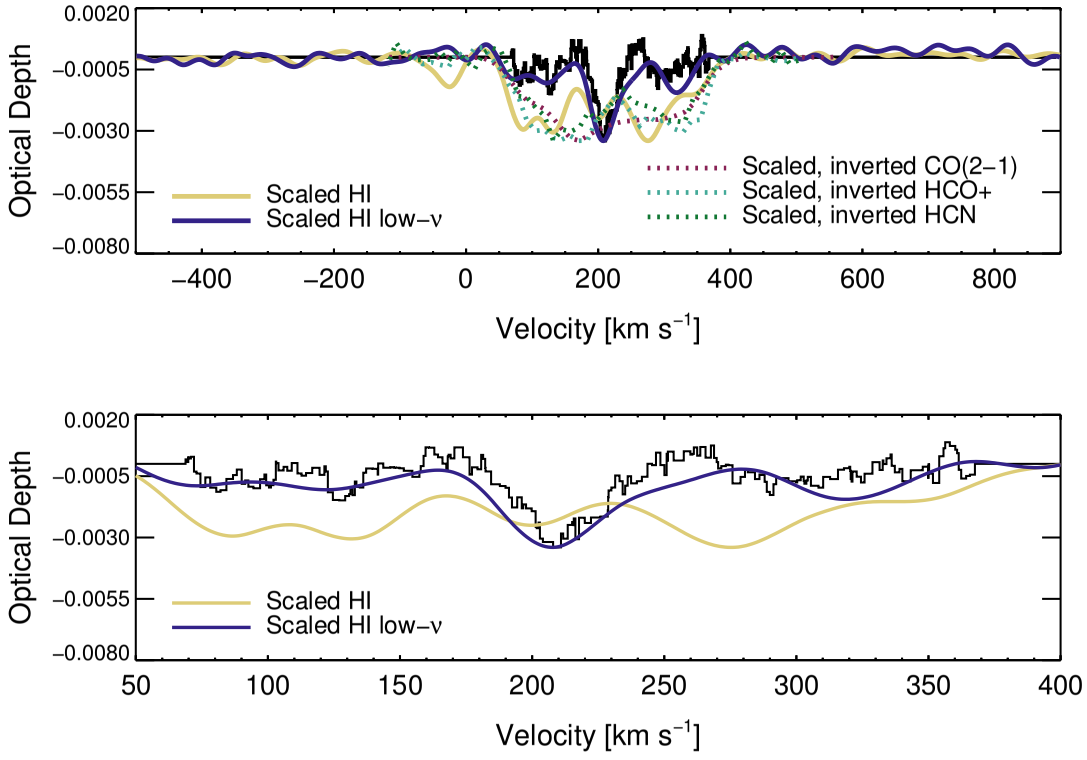

Figure 5.5: Comparison with other tracers. The CRRL profile is plotted in black. Molecular emission lines (Kepley et al., 2014) are shown by the dashed lines and are inverted for easier comparison, and H I absorption in the direction of SNRs in M82 (Wills et al., 1998) is plotted with solid colored lines. The gold solid line is the total contribution to the H I absorption profile in the direction of all SNRs in M82, while the dark blue line is the contribution from only those SNRs relatively unaffected by free-free absorption at low frequencies. The bottom panel shows the central portion of the spectra, with only the H I absorption profiles overlaid on the CRRL spectrum.

tion, higher sensitivity studies of M82 at the same frequencies would help to confirm that this feature is indeed associated with the nuclear region, and potentially shed more light on the origin of the optical depth. To constrain the gas properties we need studies at higher frequencies, and we are working towards detecting CRRLs in the range of 120 – 240 MHz with LOFAR's high band antenna array.

This discovery paves the way for future extragalactic CRRL studies to trace the CNM throughout the formation and evolution of galaxies, and is the basis of a pilot survey for CRRLs in other extragalactic sources.

Acknowledgements

LKM acknowledges financial support from NWO Top LOFAR project, project n. 614.001.006. JBRO acknowledges financial support from NWO Top LOFAR-CRRL project, project n. 614.001.351. The authors thank A. Kepley for providing GBT observed line profiles.

CHAPTER 6

Characterizing the Cold Neutral Medium in M82 with Carbon Radio Recombination Lines

"All you really need to know for the moment is that the universe is a lot more complicated than you might think, even if you start from a position of thinking it's pretty damn complicated in the first place."
−Douglas Adams−

We present observations of carbon radio recombination lines (CRRLs) from the nearby starbursting galaxy M82, with the first use of the P band of the Karl G. Jansky Very Large Array for spectroscopy. The aim of this study is to use these and previous CRRL observations of M82 to constrain the electron temperature T_e and density n_e of the cold neutral medium (CNM) in M82. When stacking only 10 of the available 50+ α-transitions ($\Delta n = 1$) we find a lower limit to the emission integrated optical depth of -100 Hz. By combining this limit with previous CRRL detections in M82 and comparing with detailed theoretical models of low-frequency CRRLs, we determine $T_e = 95^{+105}_{-85}$ K and $n_e = 0.030 \pm 0.005\,\mathrm{cm}^{-3}$. These values are similar to Galactic CRRL results and consistent with an origin in the CNM. Using previously measured H I column densities and a path length of $L = 340$ pc corresponding to previous measurements of the H I distribution, we estimate C II/H I $\lesssim 1.1 \times 10^{-3}$.

Zoutendijk, S. L., Morabito, L. K., Toribio, M. C., Oonk, J. B. R., Salgado, F., Salas, P., Röttgering, H. J. A., Tielens, A. G. G. M., et al.
In preparation

6.1 Introduction

The interstellar medium (ISM) is the repository of stellar ejecta and the birthsite of new stars and, hence, a vital factor in the evolution of galaxies over cosmic time. Cold, diffuse H I clouds are a key component of the ISM, but so far this phase has eluded detailed studies, because the main tracer, the 21-cm line, does not constrain basic physical information of the gas (e.g., temperature, density) well. With the advent of new and upgraded telescopes it is now possible to study this component of the ISM through low-frequency ($\lesssim 500$ MHz) carbon and hydrogen radio recombination lines (RRLs), which do provide a unique, sensitive probe of the physical conditions in cold, neutral clouds. Recently, Morabito et al. (2014) used the Low Frequency Array (LOFAR; van Haarlem et al., 2013) to detect carbon radio recombination lines (CRRLs) in absorption in the nearby starburst galaxy M82. The authors stacked 22 α-transitions ($\Delta n = 1$) in the frequency range 48 to 64 MHz ($n = 488$–508) to achieve an 8.5σ detection. The observed line profile had a peak line-to-continuum intensity of 3×10^{-3}, a FWHM of 31 km s^{-1}, and was centred on a velocity of 211 km s^{-1} with respect to LSR.

The velocity of the observed CRRL absorption feature indicates that it is associated with the nuclear starburst in M82. This compact region spans about 60 arcsec (approximately 1000 pc), and hosts a wide range of ISM phases. Observations of disrupted H I within the disk shows that the neutral gas is more concentrated in the nuclear region (Yun et al., 1993), where a high concentration of molecular gas is also seen (Lo et al., 1987). Observations of dense gas tracers associated with star formation indicate the presence of a rotating ring of lower density molecular gas (Kepley et al., 2014). The nuclear region is also studded with compact, bright supernova remnants (SNRs; e.g., Muxlow et al., 1994; Fenech et al., 2010), and H II regions (e.g., McDonald et al., 2002; Gandhi et al., 2011). Free–free absorption by ionised gas is also evident, seen in the spectral turnover of the SNRs (Wills et al., 1997) and the overall spectrum (Adebahr et al., 2013). The CRRLs trace a low electron density, low-temperature neutral gas component in this complex environment, but there are two main questions that a single LOFAR LBA detection cannot answer. First, by comparing the integrated optical depths and line widths of RRLs with detailed physical models, we can determine information on the physical properties of the gas, such as electron temperature and density (e.g., Salgado et al., in preparation; Ponomarev & Sorochenko, 1992; Walmsley & Watson, 1982; Brocklehurst & Seaton, 1972). The values of these observables depend sensitively on temperature and density as a function of quantum number (or equivalently frequency). Therefore, to determine these physical properties (T_e, n_e), it is crucial to observe the

CRRLs over a range of frequencies from about 50 to 500 MHz. Second, although Morabito et al. (2014) concluded that the CRRLs were likely associated with the nuclear region, M82 was unresolved in the LOFAR images. In order to understand the role of the cold neutral medium in the life cycle of the ISM in M82, it is important to establish firmly whether the CRRLs do originate in the nuclear region.

The Karl G. Jansky Very Large Array (JVLA; Perley et al., 2011) is the ideal instrument to answer these two questions. The P-band frequency range we use (248–480 MHz) covers 62 CRRL α-transitions. Even with flagging due to radio frequency interference (RFI) we expect to simultaneously observe 44+ α-transitions with sufficient sensitivity to either detect the lines or place stringent upper limits on the theoretical models of line intensity and width. At these frequencies, the CRRLs are expected to appear in emission, whereas they were observed in absorption by LOFAR. The JVLA also has sufficient angular resolution with B-configuration (maximum baseline of 11.1 km) to resolve the nuclear region of M82 separately from the rest of the galaxy, enabling us to pinpoint the spatial location of the CRRLs.

This paper outlines the JVLA P-band observations of CRRLs in M82, which are also the first spectroscopic observations performed with the JVLA's P band. Sections 6.2 and 6.3 outline observations and data reduction, respectively. Section 6.4 describes the spectral extraction and stacking of CRRLs. Results are presented in section 6.5. Discussion and conclusions follow in section 6.6 and section 6.7, respectively.

6.2 Observations

The data were taken in several blocks as part of the Resident Shared Risk Observing (RSRO) program during semester 15A. Table 6.1 summarizes the observations, which were all performed during B-configuration with identical frequency coverage. The only exception was the test block, which was observed prior to the semester when the array was still moving from A- to B-configuration. The observational blocks were dynamically scheduled and therefore vary in length, but all start and end with a standard flux calibrator, which was interleaved throughout the observation for calibration purposes. To maximize time on source, we decided not to include a separate phase calibrator, instead using a widefield model from a reduction of the TIFR GMRT Sky Survey (TGSS; Intema et al., 2016). Block 3 includes two flux calibrators because neither of them was visible for the entire observation. In practice we used only the first calibrator, 3C 147, for the data reduction of this block.

Table 6.1: Observational summary of the data taken with the JVLA.

	Date	Calibrator	Start UTC	Duration (h)	# antennae
Test Block	2015 Jan 30	3C 147	05:35:19	1.00	27
Block 1	2015 Mar 22	3C 147	04:03:23	2.15	27
Block 2	2015 Mar 27	3C 295	07:17:27	3.65	26
Block 3	2015 Mar 29	3C 147 / 3C 295	06:18:05	4.00	25
Block 4	2015 Apr 2	3C 295	06:34:19	3.65	27
Block 5	2015 Apr 4	3C 295	06:38:33	3.15	27

We used both intermediate frequencies (IFs; A0/C0 and B0/D0) with dual polarization to cover the frequency range of 248 to 453 MHz with overlapping spectral windows to provide uninterrupted frequency coverage and optimize CRRL placement. We were limited in bandwidth by the desired channel width (7.8125 kHz, $9.44\,\mathrm{km\,s^{-1}}$ – $5.17\,\mathrm{km\,s^{-1}}$) and the total allowable data rate. We used recirculation to increase the number of channels to 4096 for seven of the spectral windows with 32 MHz bandwidth each, and 2048 channels in one spectral window covering 16 MHz bandwidth. Details of the spectral windows are listed in Table 6.2.

6.3 Data Reduction

For the data reduction we used the Common Astronomy Software Applications package (CASA). The JVLA data were downloaded in science data model/binary data format (SDM/BDF) from the NRAO archive. After importing these data into the CASA measurement set (MS) format, the online flags were applied. A gain curve was calculated to compensate for instrumental elevation effects and applied to the data. We flagged the channels containing radio frequency interference (RFI) from MUOS satellites: channels 539 through 3041 in spectral window 4, corresponding to frequencies 360.211–379.766 MHz. The unflagged data were split out and Hanning smoothed to suppress Gibbs ringing around bright RFI.

The P band contains more RFI than most JVLA bands, a more elaborate process of RFI flagging was required. To avoid manually flagging the entire dataset, we used an interactive scheme with visual inspection in between non-interactive steps. First the TFCROP algorithm was applied to blocks 1 through 5 in order to remove the strongest interference. The result was inspected for each spectral window in each block to assess the usability. Spectral window 0 in its entirety and spectral window 1 up to channel 1700 were deemed unusable due to an extreme amount of RFI. The remaining data were inspected per scan for each block and spectral window, and scans showing signs of correlation failures and other instrumental issues were discarded. Some scans were only unusable for a fraction of their duration, and we flagged only the bad time ranges. At this point the MSes were split into individual spectral windows, which were processed separately. Because the data reduction is computationally expensive, we decided to focus on spectral windows 1 and 2 for now, as there are more CRRLs per spectral window at the lower frequencies of the P band.

Ten per cent of the channels are flagged on each side of the MS due to bandpass drop-off. Initial delays and bandpass corrections were determined from

Table 6.2: Details of the spectral windows in the JVLA data and the percentage of points flagged at the end of the reduction process.

	# channels	Channel width (kHz)	Start frequency (MHz)	End frequency (MHz)	Bandwidth (MHz)	Flagging (%)
Spectral window 0	4096	7.8125	248	280	32	100.0
Spectral window 1	4096	7.8125	275	307	32	68.7
Spectral window 2	4096	7.8125	302	334	32	36.6
Spectral window 3	4096	7.8125	329	361	32	...
Spectral window 4	4096	7.8125	356	388	32	...
Spectral window 5	4096	7.8125	383	415	32	...
Spectral window 6	4096	7.8125	410	442	32	...
Spectral window 7	2048	7.8125	437	453	16	...

one manually cleaned scan of the calibrator (approximately 4 min in duration) from block 3. These initial corrections were transferred to the calibrator data in the MS, together with an initial correction for the bandpass phases. This was followed by automatic RFI flagging with PIEFLAG (Middelberg, 2006; Hales & Middelberg, 2014), a CASA task to identify and remove bad data based on the statistics of an RFI-free reference channel. Any channel that was at least 97.5 per cent flagged was removed entirely. Remaining channels or time ranges obviously affected by RFI were identified by eye and flagged. After flagging was completed, the calibrator's delays and bandpass were redetermined. For the target, bandpass phase corrections were derived and applied together with the calibrator-derived delays and bandpass corrections. The PIEFLAG algorithm was run and remaining RFI was removed using visual inspection. At this point block 1, spectral window 1 was found to contain too many instrumentation-related problems, prompting its exclusion from further processing.

The delay- and bandpass-corrected data were subsequently split and averaged to a 16-channel MS, which is the maximum averaging that can be done while keeping bandwidth smearing negligible. Antenna gains for the calibrator were found using a point source model, appropriate for the resolution of these observations, with the Scaife–Heald (2012) standard. Phase-only calibration on the target was performed against a model derived from a 42.67 arcmin cut-out of the TGSS image, *w*-projected across 32 planes, using a single solution for all 16 channels. This calibration table and the calibrator's flux scale were then transferred to the target in the 4096-channel MS.

The calibrated blocks were concatenated into one MS per spectral window, dropping completely flagged rows. The percentage of data flagged is displayed in the last column of Table 6.2. Channel cubes were made for M82 with the CLEAN algorithm, using only channels within approximately $750\,\mathrm{km\,s^{-1}}$ of each expected CRRL, using the same spatial specifications as the phase-calibration model. The cleaning mask was generated with PYBDSM (Mohan & Rafferty, 2015) from a multifrequency-synthesized image of M82 using the entire spectral window. We used a cleaning threshold of 60 mJy, which is approximately three times the RMS determined from a manually cleaned cube. Taking into account the amount of flagged data and the bandwidth used, the rms noise is 1.4 times above the expected noise. The resulting cubes, with beam sizes of about 40 by 30 arcsec, were reconvolved to 60 arcsec circular beams to spatially smooth the extracted spectra and ensure one aperture would be valid for all channels.

6.4 Extracting and Stacking the CRRLs

The cleaned channels were arranged in $1000\,\mathrm{km\,s^{-1}}$ wide 'subbands' centred around the expected line positions. Drastic outliers were identified from a visual inspection and removed. We tested multiple extraction radii, from 1.6 to 3.0 times the standard deviation σ of a Gaussian fitted to M82's flux.

As the CRRLs are too weak to detect individually, line stacking is required. Though M82 has a systemic optical velocity of $210 \pm 20\,\mathrm{km\,s^{-1}}$ relative to the local standard of rest (LSR), the nuclear region alone shows velocities varying between 100 and $340\,\mathrm{km\,s^{-1}}$ (Wills et al., 1998; Kepley et al., 2014). Care therefore has to be taken in selecting the proper stacking velocity, which will depend on the location of the CRRLs' origin. We tested two different velocities: $211\,\mathrm{km\,s^{-1}}$ with respect to LSR (corresponding to a redshift $z \approx 0.00073$) as found by Morabito et al. (2014), $205\,\mathrm{km\,s^{-1}}$ ($z \approx 0.00068$) as found in LOFAR HBA observations of CRRLs in emission (Toribio et al., in preparation).

Before stacking, the subbands were corrected for residual bandpass effects. LOFAR HBA observations found a CRRL width of $65.8\,\mathrm{km\,s^{-1}}$ FWHM in emission (M. C. Toribio, private communication). The line width in our observations is expected to be comparable. We therefore blank a region of $\pm 40\,\mathrm{km\,s^{-1}}$ around the line centre and fit a polynomial to the remaining continuum. The polynomial order differs per subband, ranging from one through five. We divided the extracted flux by the fitted polynomial and subtracted from unity. Points more than three times the standard deviation away from zero were removed.

There were 12 lines in the unflagged parts of spectral windows 1 and 2, two of which had to be discarded because the residual bandpass was too irregular. The remaining ten lines have principle quantum numbers $n = 271$ and 273 through 282. None of the different combinations of extraction radius and systemic velocity produced a detection visible by eye. We therefore attempted to smooth the spectrum with an appropriate low-pass filter. We tested Savitzky–Golay filters (Savitzky & Golay, 1964) of orders 1 and 2, a boxcar filter, and a general least-squares filter, using filter widths from 5 to 61 points (corresponding to approximately 4 to $46\,\mathrm{km\,s^{-1}}$). The signal-to-noise ratio was approximated by dividing the standard deviation of the filtered stack within the blanking region by the standard deviation of the filtered stack outside of the blanking region. A maximum signal-to-noise ratio of 1.6 was found for a general least-squares filter with a width of 11 points, using a Gaussian aperture with a radius of 2.0σ and a redshift $z = 0.00068$. This extraction radius corresponds to an area with a physical diameter of $\sim 1.8\,\mathrm{kpc}$. The stack is shown in Figure 6.1.

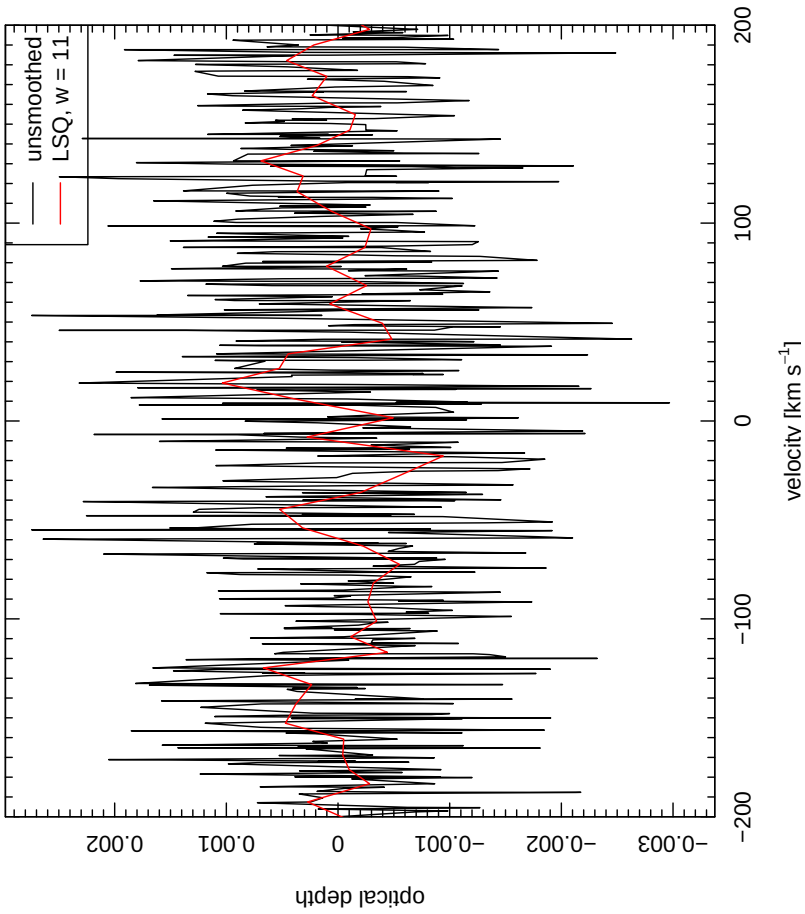

Figure 6.1: Stacked CRRL spectra from spectral windows 1 and 2, overlayed with a general least-squares filter of width 11. The subbands were stacked at redshift $z = 0.00068$, corresponding to a systematic optical velocity of $205\,\mathrm{km\,s^{-1}}$ with respect to the local standard of rest. Velocities are given in optical convention and relative to the systematic velocity. The velocity coverage in the central $\pm 200\,\mathrm{km\,s^{-1}}$ is $\sim 0.75\,\mathrm{km\,s^{-1}}$ per point. There is no detection of the CRRLs. The root-mean-square optical depth of the central $\pm 40\,\mathrm{km\,s^{-1}}$ is 1.4×10^{-3}.

6.5 Results

As the signal-to-noise ratio of the best stack is too low for a detection, we determine an upper limit to the peak optical depth by calculating the root-mean-square of the best stack in the central $\pm 40\,\mathrm{km\,s^{-1}}$. This upper limit is $\tau_{\mathrm{peak}} < 1.4 \times 10^{-3}$. Assuming a FWHM of $65.8\,\mathrm{km\,s^{-1}}$, the corresponding lower limit on the integrated optical depth is $\tau_{\mathrm{int}} > -100\,\mathrm{Hz}$. We adopt a ten per cent uncertainty on this value to account for the possibility of a different FWHM, resulting in $\tau_{\mathrm{int}} = -100^{+100}_{-10}\,\mathrm{Hz}$.

This result, together with previously determined integrated optical depths from LOFAR LBA ($\tau_{\mathrm{int}} = 21.3^{+1}_{-5}\,\mathrm{Hz}$, Morabito et al., 2014) and HBA ($\tau_{\mathrm{int}} = -30 \pm 2\,\mathrm{Hz}$, M. C. Toribio, private communication) observations, can be used to constrain the electron temperature and density of the cold neutral medium in M82. Detailed theoretical models of CRRLs (F. Salgado et al., submitted) predict the departure from local thermal equilibrium (LTE), which can be converted into integrated optical depth, for given values of the electron temperature T_e and electron density n_e. Modelled departure coefficients, defined as the ratio between actual and LTE level populations, were calculated for a grid of values for these two parameters. T_e varied from 10 to 250 K in steps of 5 K. The density n_e varied from 0.01 to $0.110\,\mathrm{cm^{-3}}$ in steps of $0.005\,\mathrm{cm^{-3}}$. We assume the background radiation temperature follows the Galactic power law

$$T_{\mathrm{R}} = T_0 \left(\frac{\nu}{\nu_0} \right)^{-2.6}, \tag{6.1}$$

with reference temperature $T_0 = 2000\,\mathrm{K}$ at $\nu_0 = 100\,\mathrm{MHz}$. This is based on Galactic values, which were estimated from the radio continuum at 408 MHz (Haslam et al., 1982). We estimated the radiation temperature of the nuclear region from previous higher-resolution HBA observations to be $\sim 3000\,\mathrm{K}$. Thus $T_0 = 2000\,\mathrm{K}$ is a reasonable assumption.

To scale the departure coefficients to integrated optical depth, the emission measure, defined as

$$\mathrm{EM} = \int_0^L n_{\mathrm{C\,II}} n_e \, \mathrm{d}s, \tag{6.2}$$

where the $\mathrm{d}s$ is a path element along the line of sight, is required. We assume that in the otherwise neutral medium, all electrons come from singly ionised carbon. If the carbon population is mostly in C II then $n_e \approx n_{\mathrm{C\,II}}$. If the electron density is constant along the line of sight, or if it is appropriately averaged, the

emission measure simplifies to

$$\mathrm{EM} = n_e^2 L, \tag{6.3}$$

where $L \equiv \int \mathrm{d}s$ is the path length through the observed object.

Because we only have two optical depth measurements and one lower limit, an assumption for L has to be made for the comparison of the model to the observations to be well constrained. Weliachew et al. (1984) found that the H I distribution in M82 can be described as a toroid with an inner radius of 170 ± 20 pc and an outer radius of 340 ± 30 pc. Assuming that the CRRLs trace the cold H I, a line of sight through the centre of the toroid, from end to end, corresponds to a path length of 340 pc. We assume that the detected CRRLs in emission originate from clouds distributed throughout the toroid, therefore we adopt $L = 340$ pc in this case (unity filling factor).

For the CRRLs in absorption we test two different assumptions. The simplest assumption is that the path length will be the same for both emission and absorption. However, one could also argue that if the absorbed emission originates from M82's nucleus only the clouds in front of the nucleus can be the origin of the CRRLs in absorption, and that therefore the path length for absorption should be 170 pc. Evidence for this is found in the HBA detection of CRRLs, which have a centroid offset from that of the LBA detection by -15.8 km s^{-1}, and a wider full width half maximum. The larger line width in emission could be explained by a line of sight through a larger number of independently moving clouds of H I.

Chi-squared values are calculated by comparing the models in this grid with the observed integrated optical depths. Confidence intervals on the grid were determined by integrating $1/\chi^2(T_e, n_e)$ over the grid, starting at the highest value of $1/\chi^2$ and including progressively lower values until the integrated volume encompasses a 1σ, 2σ, or 3σ fraction of the total volume. The resulting confidence intervals are shown in Figure 6.2.

To obtain separate constraints on T_e and n_e, we collapsed the grids along these two axes and integrated outwards from the maximum value to determine one-dimensional confidence intervals and the values with maximum $1/\chi^2$. For the case where $L = 340$ pc for both emission and absorption, we determined $T_e = 95^{+105}_{-85}$ K and $n_e = 0.030 \pm 0.005$ cm^{-3}, where the errors are based on the 1σ one-dimensional confidence intervals. If we assumed the path length is 340 pc for emission and 170 pc for absorption, the result was $T_e = 85^{+100}_{-75}$ K and $n_e = 0.04 \pm 0.005$ cm^{-3}. The best fit models are shown in Fig. 6.3. Both cases describe the data well; to judge which assumption on the path length is more correct a

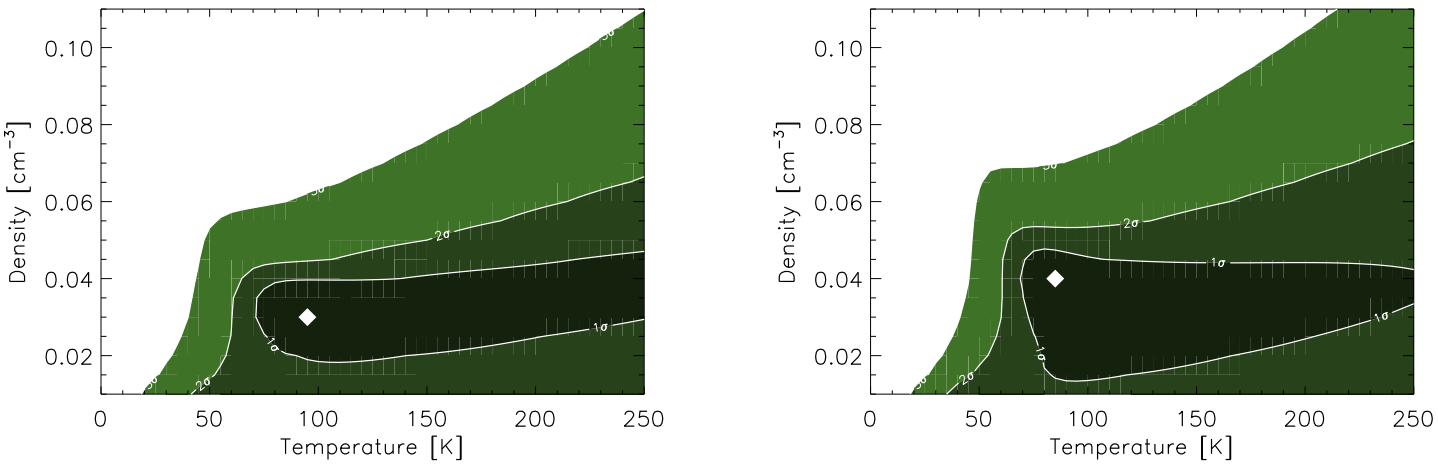

Figure 6.2: Confidence intervals on the electron temperature T_e and electron density n_e based on the observed and modelled integrated optical depths. In the left panel it is assumed that the path length is 340 pc for both emission and absorption, while in the right panel the path length is 340 pc for emission and 170 pc for absorption. The three regions are 1σ, 2σ, and 3σ confidence intervals, from the darkest to the lightest shade. The best-fit value is indicated by a white diamond.

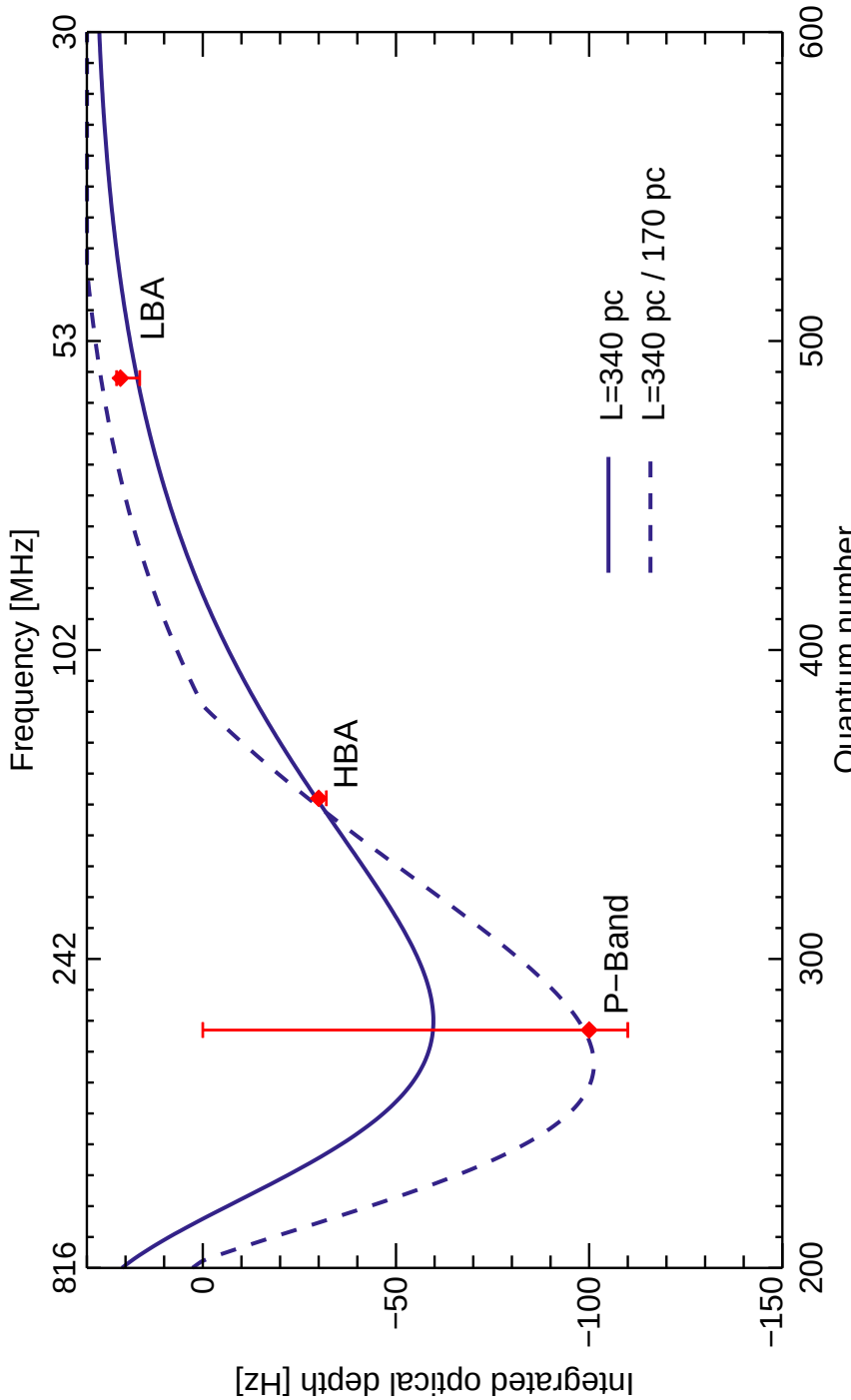

Figure 6.3: Integrated optical depths plotted with the two best-fit models. The solid blue line is for the best fit model with a single path length of 340 pc. The dashed blue line is for the best fit model assuming a path length of 340 pc for emission and 170 pc for absorption.

stricter lower limit on the integrated optical depth or a detection of the CRRLs in the P band is required. In the following we base our calculations on the case that $L = 340\,\mathrm{pc}$ in both emission and absorption, as it is the simpler assumption of the two. Because the results above are in agreement with each other, the following calculations will not change significantly if we choose the other set of results.

6.6 Discussion

The values found for T_e and n_e are compatible with the expectation that we observe diffuse CRRLs that trace the CNM. Morabito et al. (2014) found that the CRRLs in M82 are likely associated with the neutral hydrogen in M82, which is also seen in our own Galaxy (e.g., Anantharamaiah et al., 1994). The values of T_e and n_e from this paper are also similar to Galactic values. For example, Oonk et al. (2014) found values of $T_e \sim 110\,\mathrm{K}$ and $n_e \sim 0.06\,\mathrm{cm}^{-3}$ in the direction of bright background source Cygnus A. This is supporting evidence that CRRLs in our Galaxy and in M82 originate in similar conditions.

If we assume that the CRRLs trace the cold H I gas component in M82, the free electrons should be supplied by carbon, and $n_e \approx n_C$. The path length L can be used to convert density (cm^{-3}) to column density (cm^{-2}) for a comparison with previously measured H I column densities. This provides an estimation of the carbon-to-hydrogen ratio. For $L = 340\,\mathrm{pc}$, the column density is $N_{\mathrm{CII}} \sim 3.2 \pm 0.5 \times 10^{19}\,\mathrm{cm}^{-2}$. Measured column densities for cold H I in the direction of supernovae remnants in the nuclear region of M82 range from $> 30 \times 10^{21}$ to $< 1.6 \times 10^{21}$ cm^{-2} (Wills et al., 1998). The ratio C II/H I therefore ranges from 1.1×10^{-3} to 2.0×10^{-2}.

The estimated C II/H I ratio is about an order of magnitude higher than what has previously been measured for the diffuse interstellar medium (1.4×10^{-4}; Sofia et al., 1997). It is likely that our estimated ratio is actually higher than the real value, as the H I column density measurements are from observations with small beams that do not cover the entire region from which CRRLs may originate, and there is a tendency for higher column densities to be associated with the supernovae remnants unaffected by free-free absorption (thought to be associated with the LBA CRRL; see Morabito et al., 2014). The relevant H I content in the CNM may therefore be underestimated. This would decrease the upper limit on the C II/H I ratio. The ratio would also be reduced if the C II column density is actually smaller than the upper limit quoted here. It is difficult to estimate how this would change, as L, T_e, and n_e are degenerate and changes in path length and/or density could be absorbed by changes in T_e. Spatially resolving the region of CRRL emission is necessary to further constrain the path

length, and more measurements spread in frequency will help further constrain the temperature and density. It is not unreasonable to expect a higher C II/H I ratio in M82, as carbon enhancement associated with the nuclear region has been observed (e.g., White et al., 1994).

We can derive a total mass for C II using n_e and and the Carbon mass density, $\rho_C = (6.0 \pm 4.0) \times 10^{-25}\,\mathrm{g\,cm^{-3}}$, and assuming that the C II gas comes from a volume equal to that of the toroid described by (Weliachew et al., 1984). The volume of this toroid is on the order of $(2-3) \times 10^7\,\mathrm{pc}^3$, we therefore find a total carbon mass of $M_{\mathrm{CII}} \sim (1-3) \times 10^5\,M_\odot$. Assuming that the CNM mass is dominated by H I and C II, its total mass is:

$$M_{\mathrm{CNM}} \approx \left(1 + \frac{m_{\mathrm{H}}}{m_{\mathrm{C}}}\left[\frac{\mathrm{H}}{\mathrm{CII}}\right]\right) M_{\mathrm{CII}}. \tag{6.4}$$

For C II/H I$\sim 2.0 \times 10^{-2}$, this provides $M_{\mathrm{CNM}} \sim 5.3 \times 10^5 - 1.6 \times 10^6\,M_\odot$. For C II/H I$\sim 1.1 \times 10^{-3}$ the mass ranges from $M_{\mathrm{CNM}} \sim 8.1 \times 10^6 - 2.4 \times 10^7\,M_\odot$. Weliachew et al. (1984) estimated $M_{\mathrm{HI}} \sim 1.2 \times 10^7\,M_\odot$, which is in agreement with the masses calculated for the smaller C II/H I ratio of $\sim 1.1 \times 10^{-3}$. The total CNM mass estimates are $\sim 0.2 - 14$ per cent of the dense molecular gas mass in M82's nucleus, which is $M_{\mathrm{dense}} \sim (1.7 - 2.7) \times 10^8\,M_\odot$ (Naylor et al., 2010).

6.7 Conclusions

We have analysed spectroscopic observations of M82 with the JVLA P band to study diffuse CRRLs. By stacking 10 CRRL α-transitions, we provided an upper limit of 1.4×10^{-3} on the peak optical depth and a lower limit of $-100\,\mathrm{Hz}$ on the integrated optical depth. Comparing the lower limit on the integrated optical depth with a grid of detailed theoretical models of low-frequency CRRLs allowed us to constrain the electron density and temperature to $T_e = 95^{+105}_{-85}\,\mathrm{K}$ and $n_e = 0.030 \pm 0.005\,\mathrm{cm^{-3}}$. These values are similar to what has been seen for the CNM in our own Galaxy. By using the assumed path length $L = 340\,\mathrm{pc}$ for the H I distribution as measured by Weliachew et al. (1984), we estimate a total C II column density of $3.2 \pm 0.5 \times 10^{19}\,\mathrm{cm^{-2}}$. Comparison with the range of H I column densities measured by Wills et al. (1998) therefore imply carbon-to-hydrogen ratios of $1.1 \times 10^{-3} - 2.0 \times 10^{-2}$. Using the smaller carbon to hydrogen ratio and the carbon mass density, we estimate that the CNM in M82 has a total mass of $8.1 \times 10^6 - 2.4 \times 10^7\,M_\odot$, in agreement with previous measurements of the total mass of H I.

Stricter constraints on the integrated optical depth in the P band, or ideally a detection, are required to further constrain the determined T_e and n_e and test the assumptions on the path length. The work presented here only reports on 10 of the available lines, and adding more CRRL transitions would increase the signal to noise ratio by a factor of $\sqrt{N}$. Using conservative estimates on loss of data due to RFI flagging there will be a minimum of 20 lines available for stacking. By using these CRRL transitions we will increase the signal to noise and provide either tighter limits on or a detection of the CRRLs.

Acknowledgements

SLZ and JBRO acknowledge financial support from NWO Top LOFAR-CRRL project, project n. 614.001.351. LKM acknowledges financial support from NWO Top LOFAR project, project n. 614.001.006.

CHAPTER 7

Exact Bound-Bound Gaunt Factor Values for Quantum Levels up to n=2000

"We are stuck with technology when what we really want is just stuff that works."
−Douglas Adams−

Comparison of observations of radio recombination lines in the interstellar medium with theoretical models can be used to constrain electron temperature and density of the gas. An important component of the models is spontaneous transition rates between bound levels. Calculating these rates relies on accurate bound-bound oscillator strengths, which can be cast in terms of the Gaunt factor. The Gaunt factor contains terminating hypergeometric functions that cannot be calculated with sufficient accuracy for high quantum levels ($n \gtrsim 50$) by standard machine-precision methods. Methods to overcome the accuracy problem have been developed, which include asymptotic expansions and recursion relations. These methods, used in astrophysical models to calculate oscillator strengths, can introduce errors, sometimes up to as much as ~ 8 per cent. Detections of radio recombination lines with the new Low Frequency Array (LOFAR) has prompted an examination of theoretical models of the interstellar medium. We revisit the calculation of the Gaunt factor, employing modern arbitrary-precision computational methods to tabulate the Gaunt factor for transitions up to quantum level $n = 2000$, sufficient to model low frequency Carbon radio recombination lines. The calculations provide a relative error of $\sim 3 \times 10^{-4}$ when compared to more detailed calculations including relativistic corrections. Our values for the Gaunt factor are provided for download in a tabular format to be used for a wide range of applications.

Morabito, L. K., van Harten, G., Salgado, F.,
Oonk, J. B. R., Röttgering, H. J. A., Tielens, A. G. G. M.
2014, MNRAS, 441, 2855

7.1 Introduction

Diffuse, ionized gas is one component of the interstellar medium (ISM), where ions and free electrons recombine and produce spectral lines we call recombination lines. When these transitions occur at low quantum numbers, the recombination lines appear in the optical and UV regime. Recombination lines occur in the radio regime when the quantum numbers involved in the transitions are above $n \gtrsim 50$, due to the decreased energy spacing of adjacent levels. Models of radio recombination lines (RRLs) therefore have to predict accurate line intensities for quantum levels above $n \gtrsim 50$.

In our own Galaxy, RRLs are used to study two phases of the ISM. The "classical" RRLs are associated with HII regions, and are usually observed at frequencies above 1.4 GHz (e.g., Palmer, 1967; Roelfsema et al., 1987). These RRLs trace the warm, high density ($T \sim 10^4$ K, $n_e > 100$ cm^{-3}) medium. Frequencies below ~1.4 GHz are associated with the cold, low-density ($T \sim 100$ K, $n_e \lesssim 0.05$ cm^{-3}) medium (e.g., Shaver, 1976; Payne et al., 1989; Kantharia & Anantharamaiah, 2001) and trace the diffuse component of the ISM. Diffuse Carbon RRLs with bound levels as high as $n \sim 1000$ have been observed in the direction of Cassiopeia A (Konovalenko & Sodin, 1980; Stepkin et al., 2007; Asgekar et al., 2013). High quantum number RRLs manifest at low frequencies, and provide an important method to study physical properties such as electron temperature and density in the cold neutral medium. With recently completed low-frequency (<300 MHz, $n > 280$) radio telescopes, such as the Low Frequency Array (LOFAR; van Haarlem et al., 2013), we will be able to study these high quantum level transitions. With its unprecedented sensitivity, frequency resolution and coverage and multibeaming capability enabling efficient surveys of the sky, LOFAR will revolutionise the field of low frequency RRL studies as a crucial method for studying an important phase of the interstellar medium that so far has eluded detailed studies. Not only will we be able to map a large fraction of the Galaxy, but extragalactic sources of RRLs will be accessible, providing a redshift-independent means of studying the cold, diffuse gas content of galaxies.

The ability to calculate accurate bound-bound spontaneous transition rates in recombining ions has a wide range of applications, from predictions and measurements in the laboratory to extracting information from observations of a variety of astronomical phenomena. The transition rates depend on the atomic oscillator strengths, which are used to calculate the spontaneous and stimulated transition rates for non-relativistic electrons. The oscillator strength is easily described in terms either of the Gaunt factor or line strength. For low quantum

number states, analytical formulae for oscillator strengths are easy to compute. However, direct calculation of higher n transitions is impossible due to round-off errors and limitations on standard machine representation of numbers.

Predicting line intensities requires determining the LTE level populations of excited states, or levels, in an atom. There is a quantum level beyond which the electron will no longer be bound to the atom, and theoretical models must include all quantum levels up to this cut-off level in order to ensure correct calculations of the LTE level populations. For the low temperature, low density phase of the ISM from which we expect Carbon RRLs to originate, we have found a cut-off level of $n = 2000$ is sufficient to ensure this condition and therefore provide accurate line intensities (Salgado et. al, in prep.).

Here we revisit the calculation of the bound-bound Gaunt factor for quantum levels up to $n = 2000$, using arbitrary-precision operations to compute and tabulate exact values of the Gaunt factor for easy use. In this paper we compare different methods of calculation, and provide a downloadable FITS table[1] for general use. In section 2 we review the analytical form for the Gaunt factor and its relation to oscillator strength. In section 3 we discuss different methods to calculate oscillator strengths. Section 4 presents our arbitrary-precision method followed in Section 5 by a comparison of various methods. Conclusions are given in section 6, and a link to the downloadable data can be found in the Supporting Information section.

7.2 Oscillator Strength and the Gaunt Factor

The Gaunt factor is used to calculate spontaneous and stimulated transition rates of electrons between quantum levels. The spontaneous transition rates, $A_{nn'}$, can be expressed directly in terms of oscillator strength,

$$A_{nn'} = \frac{\omega_{n'}}{\omega_n} \frac{8\pi e^2 \nu^2 \mu}{m_e c^3} g_{nn'} f'_{nn'}, \tag{7.1}$$

where ω_n ($\omega_{n'}$) is the statistical weight of level n (n'), e and m_e are the charge and mass of an electron, ν is the frequency of the transition between level n and n', c is the speed of light, μ is the reduced mass, and $f_{nn'}$ is the oscillator strength, which can be expressed in terms of the Gaunt factor, $f_{nn'} = g_{nn'} f'_{nn'}$. The factor $f'_{nn'}$ is calculated from the statistical weight and quantum numbers,

[1] Available via the Strasbourg astronomical Data Center, http://cdsweb.u-strasbg.fr/

giving a total oscillator strength of:

$$f'_{nn'} = \frac{2^6}{3\sqrt{3}\pi}\frac{1}{\omega_{n'}}\frac{1}{\left(\frac{1}{n'^2}-\frac{1}{n^2}\right)^3}\left|\frac{1}{n^3 n'^3}\right|. \tag{7.2}$$

This can be substituted into Equation 7.1, expressing the transition rate in terms directly dependent on the Gaunt factor. Alternatively, total oscillator strength can be expressed in terms of radial dipole matrix elements, $R(nlm, n'l'm') = \langle\psi_{nlm}(\mathbf{r})|\mathbf{r}|\psi_{n'l'm'}(\mathbf{r})\rangle$, where ψ is the hydrogenic wave function, and $\mathbf{r}$ is the electron position vector. Equation 7.1 still holds, but now the oscillator strength is defined:

$$f_{nn'} = \frac{1}{3\omega_n}\left(\frac{1}{n^2}-\frac{1}{n'^2}\right)\frac{S_{nn'}}{e^2 a_0^2} \tag{7.3}$$

where $S_{nn'}$ is the line strength, dependent on the radial dipole matrix elements.

The Gaunt factor for bound-bound transitions between discrete quantum levels n and n' have the following form (Menzel & Pekeris, 1935), and are the same whether the transition is in absorption or emission, i.e. $g(n \to n') = g(n' \to n)$:

$$g_{nn'} = \pi\sqrt{3}\left|\frac{[(n-n')/(n+n')]^{2n+2n'} nn'\Delta(n,n')}{n-n'}\right|. \tag{7.4}$$

The factor $\Delta(n, n')$ is defined as:

$$\begin{aligned}\Delta(n,n') \equiv &\left[F(-n+1,-n',1,-\frac{4nn'}{(n-n')^2}\right]^2 \\ &-\left[F(-n'+1,-n,1,-\frac{4nn'}{(n-n')^2}\right]^2\end{aligned} \tag{7.5}$$

where $F(a, b; c; z)$ is the hypergeometric function:

$$F(a,b;c;z) = \sum_{n=0}^{\infty}\frac{\Gamma(a+n)\Gamma(b+n)\Gamma(c)}{\Gamma(a)\Gamma(b)\Gamma(c+n)}\frac{z^n}{n!}. \tag{7.6}$$

Expanding the series into terms provides:

$$F(a,b;c;z) = 1 + \frac{ab}{c}z + \frac{a(a+1)b(b+1)}{c(c+1)}\frac{z^2}{2} + \ldots. \tag{7.7}$$

The series will terminate, i.e. have a finite number of terms, if either a or b is zero or a negative integer (e.g., Whittaker & Watson, 1963; Gradshteyn et al., 2007). The magnitude of each term in the series is greater than that of the previous term, with alternating signs.

7.3 Methods of Calculation

Arithmetic operations involving very large or very small numbers on computers can result in round-off errors, and the error increases with the number of operations (for a more detailed discussion see e.g., Press et al., 1986). When calculating the value of Equation 7.5, the round-off errors (loss in accuracy) quickly start to add up, and once the standard floating-point limit of a machine is reached, fail to provide real, non-infinite values. This has been remarked upon by various authors (e.g., Gounand & Petitjean, 1984; Delone et al., 1994; Flannery & Vrinceanu, 2002) and Dewangan (2012) point out that the exact value of n for which these calculations start to break down depends on the variety of algorithms and methods used. The round-off errors and limitations of the standard floating-point machine representation of numbers have driven other methods of calculation for oscillator strengths. We outline three prevalent methods in this section, and provide a summary of their accuracy and range of quantum numbers for which they are valid in Table 7.1. These methods rely on numerous devices which do not involve direct calculation from the analytical formulae (given in the previous section).

7.3.1 Asymptotic Expansion

Asymptotic expansions are powerful approximations (e.g., Wright, 1935; Menzel & Pekeris, 1935; Omidvar & McAllister, 1995) that have long been used for calculations involving the Gaunt factor for quantum levels above $n \gtrsim 50$. These expansions are still widely used in astrophysical models (e.g., Shaver, 1975a; Salem & Brocklehurst, 1979; Kraus et al., 2000; Bergemann et al., 2010).

A commonly cited form of the asymptotic expansion is that of Menzel & Pekeris (1935), as corrected by Burgess (1958), which is obtained by the method of steepest descent (e.g., Whittaker & Watson, 1963). The first three terms are reproduced here in Equation 7.8. This expansion is valid when the difference between the levels is large ($n'/n \ll 1$).

$$g_{nn'} \simeq 1 - \frac{0.1728(1+(n'/n)^2)}{(n'(1-(n'/n)^2))^{2/3}} - \frac{0.0496(1-\frac{4}{3}(n'/n)^2+(n'/n)^4)}{(n'(1-(n'/n)^2))^{4/3}} + \cdots \tag{7.8}$$

This formula is easy to compute, and allows for approximations of the Gaunt factor for quantum levels that are not calculable from Equation 7.4 using standard machine precision. These approximations have errors of $\sim 0.5-8$ per cent (Table 1; Burgess, 1958). Omidvar & McAllister (1995) showed that the error

in the Menzel & Pekeris (1935) expansion can be reduced by an order of magnitude by keeping eight terms instead of five in the expansion. They additionally provide their own asymptotic expansion that has errors not in excess of 0.5 per cent.

7.3.2 Recursion Relations

Another way to calculate oscillator strength is via stable recursion relations (e.g., Dy, 2009; Storey & Hummer, 1991; Infeld & Hull, 1951). In this method, the line strength $S_{nn'}$ in Equation 7.3 is equated to the radial dipole matrix elements:

$$S_{nn'} \sim \sum_{l,l'} |R(nl, n'l')|^2. \tag{7.9}$$

The calculation of R, the radial dipole matrix elements, also contains the hypergeometric function. However, the matrix elements between subsequent states can be linked through recursion relations (e.g., Infeld & Hull, 1951). Given a starting point, higher quantum number states can be calculated through these relations. The total $n \rightarrow n'$ transition rate comes from summing over l levels. Storey & Hummer (1991) use these relations to calculate values of $R(nl, n'l')$ for up to $n = 500$, and provide FORTRAN code (reference given in Storey & Hummer, 1991) to perform these calculations. Dy (2009) also provide a FORTRAN code that makes use of recursion relations, to calculate values up to $n = 1000$. Both programs were not optimized to handle calculations above these ranges, and are therefore not sufficient for use in our theoretical models of low frequency RRLs, which require calculations up to $n = 2000$.

A robust method developed by Dewangan (2002, see also Dewangan 2012) exploits recursion relations in Jacobi polynomials. Standard mathematical texts transform the hypergeometric function to Jacobi polynomials, which have well known properties, including recursion relations and asymptotic expansions (e.g., Gradshteyn et al., 2007; Abramowitz & Stegun, 1972). The recursion relations make it possible to directly calculate the Jacobi polynomials necessary, as Dewangan (2002) demonstrated for a sampling of levels up to $n \sim 1000$ using extended (quadruple) precision. The author also discusses the usefulness of the asymptotic expression of the Jacobi polynomial to examine the behaviour at large n, which provides results in good agreement with the analytical values for a large range of parameters. This method is discussed in far more detail in Dewangan (2012), and the interested reader is referred there for further details.

7.3.3 OPACITY Project

The National Institute of Standards and Technology (NIST) Atomic Spectra Database[2] (Kramida et al., 2012) is widely used by the scientific community. This database contains, among other information, values for spontaneous transition rates that are the product of extensive calculations of the OPACITY project (The Opactiy Project Team, 1995). The OPACITY team extended the close-coupling method, in which wavefunctions are expanded in terms of the product of functions describing the N-electron states and functions describing the $(N+1)$ electron. The entire electron system is divided into an inner and an outer region, with boundary conditions set between the two regions. An iterative process finds solutions for the outer region, and matching the boundary conditions to the inner region then provides an eigenvalue problem which can be solved to find the bound energy states. In the newest update to the NIST database (Wiese & Fuhr, 2007), the team used sophisticated multi-configuration Hartree-Fock calculations that include relativistic effects to account for both fine and hyperfine structure. These values were checked against the few available experimental results, and the discrepancies between the theoretical and experimental values are less than about 2 per cent Wiese & Fuhr (2007). For a more in depth discussion of this method, we refer the reader to Wiese & Fuhr (2007); Seaton (1985), and references therein.

7.4 Arbitrary-Precision Calculations

Although the Gaunt factor (Equation 7.4) is of order unity, it is composed of factors that can be extremely large or small. For example, for the $n = 2000$ to $n' = 1999$ transition, the value of the hypergeometric functions is of the order $10^{28,000}$, while the multiplicative factor in front of it is of the order $10^{-28,000}$, yielding a value close to 1. To calculate values as large as $\sim 10^{\pm 28,000}$, it is necessary to increase the precision of the calculation. MATHEMATICA (Wolfram Research, Inc., 2010) allows the user to specify the required precision of the final calculation, and uses a $MaxExtraPrecision variable to control the precision of intermediate calculations. We requested a final precision of 10 digits, and the default value of 50 for $MaxExtraPrecision. MATHEMATICA will keep track of the resulting precision at each intermediate step, and if the precision becomes worse than the desired precision for the final answer, $MaxExtraPrecision will return an error. Calculating the bound-bound Gaunt factor for transitions up to $n = 2000$ took approximately 5 hours in MATHEMATICA using one 2.53GHz core with

[2] http://physics.nist.gov/asd

Table 7.1: A Sample of Methods of Calculating Oscillator Strength.

Method	Reference	n-range	Error (per cent)	Error determination
Asymptic Expansion	Menzel & Pekeris (1935)	$n \leq 35$; $n' = 1,2,3$	≤ 8	Comparison with selected analytical values
	Malik et al. (1991)	$50 \leq n \leq 900$	…	"Correct" to machine precision[1]
	Omidvar & McAllister (1995)	≤ 905	0.5	Comparison with selected analytical values
Recursion Relations	Storey & Hummer (1991)	≤ 500	< 1	Evaluation of loss of significant figures
	Dewangan (2002)	$10 \leq n \leq 1000$	…	"Correct" to machine precision[1]
OPACITY Project	Wiese & Fuhr (2007)	$n \lesssim 40$	2	Comparison with selected experimental values

[1] No error is reported, as transformations to equate the hypergeometric function to polynomials of other forms are used, and assumed to be exact.

4GB of available RAM. We only performed the calculations for $n \to n'$, since the value for the inverse transition is the same. The precision in these calculations is set by the lack of relativistic corrections, and is therefore of the order 10^{-4}. Our values therefore have a precision of ≈ 0.01 per cent.

7.5 Comparison of Other Methods of Calculation

7.5.1 Comparison with Asymptotic Expansion

We start with a direct comparison of the Gaunt factor from the Menzel & Pekeris (1935) asymptotic expansion and arbitrary-precision values in Fig. 7.1. The top left panel shows the analytical values calculated with finite-precision. Starting around $n \gtrsim 50$, standard finite-precision can no longer represent the values of the hypergeometric series terms in the Gaunt factor, and therefore most of the plot is empty. A zoom-in of the first 300 quantum levels is shown to further clarify the behaviour on the boundary of the region where values can still be represented by standard finite-precision calculations. The location of this boundary is set by the amount of bits available for double-precision calculations on a machine, and to a smaller extent the algorithms and methods used. When round-off errors start to be large, the Gaunt factor values near the boundary fluctuate. The top right panel demonstrates that Gaunt factor values calculated using the asymptotic expansion are at least able to fill the entire parameter space, giving real values near unity for all Δn transitions. The bottom left panel shows the analytical values for the Gaunt factor calculated using arbitrary-precision. The plot looks remarkably similar to that of the asymptotic expansion, so we plot the difference between the arbitrary-precision and asymptotic expansion values in Fig. 7.2. The difference between the arbitrary-precision and asymptotic expansion values is almost always less than the accuracy in the arbitrary-precision values, but it is precisely in the region of interest, $\Delta n \sim 1$ (adjacent levels), that the difference is largest. The maximum difference is 0.03, which means the asymptotic expansion is up to 3 per cent too large or small compared to the analytical values.

7.5.2 Relative Differences Between Methods

To compare with methods that calculate line strength rather than the Gaunt factor, we use the final value for spontaneous transition rates. The comparison is made using spontaneous transition rates for Hydrogen, with a reduced mass of $\mu = 0.99945568$. The NIST values include relativistic corrections and are therefore more complete and precise than other methods, so we compare the relative difference between the various methods and the NIST transition rates, $|A_{n,n',\mathrm{NIST}} - A_{n,n'}| / A_{n,n',\mathrm{NIST}}$. We are only able to make a comparison for those

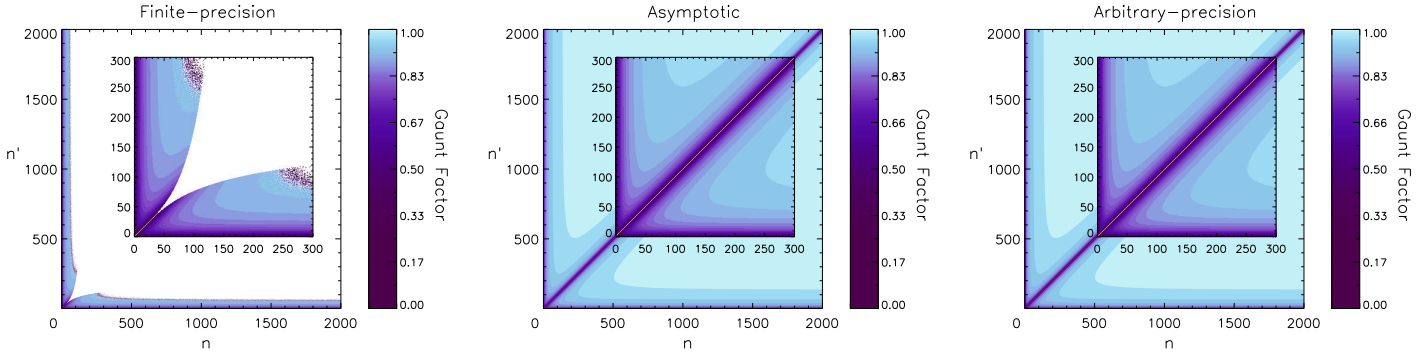

Figure 7.1: Values of the Gaunt factor for transitions amongst levels up to $n = 2000$. From left to right: using standard-precision calculations of the analytic expression; using the Menzel & Pekeris (1935) asymptotic expansion; using arbitrary-precision calculations of the analytic expression in MATHEMATICA. In the left panel, the white space shows where the values of the Gaunt factor cannot be represented by standard finite-precision calculations. The middle and right panels provide values of the Gaunt factor for every transition where $n \neq n'$. The difference between the two plots is hard to distinguish, and is plotted in Fig. 7.2.

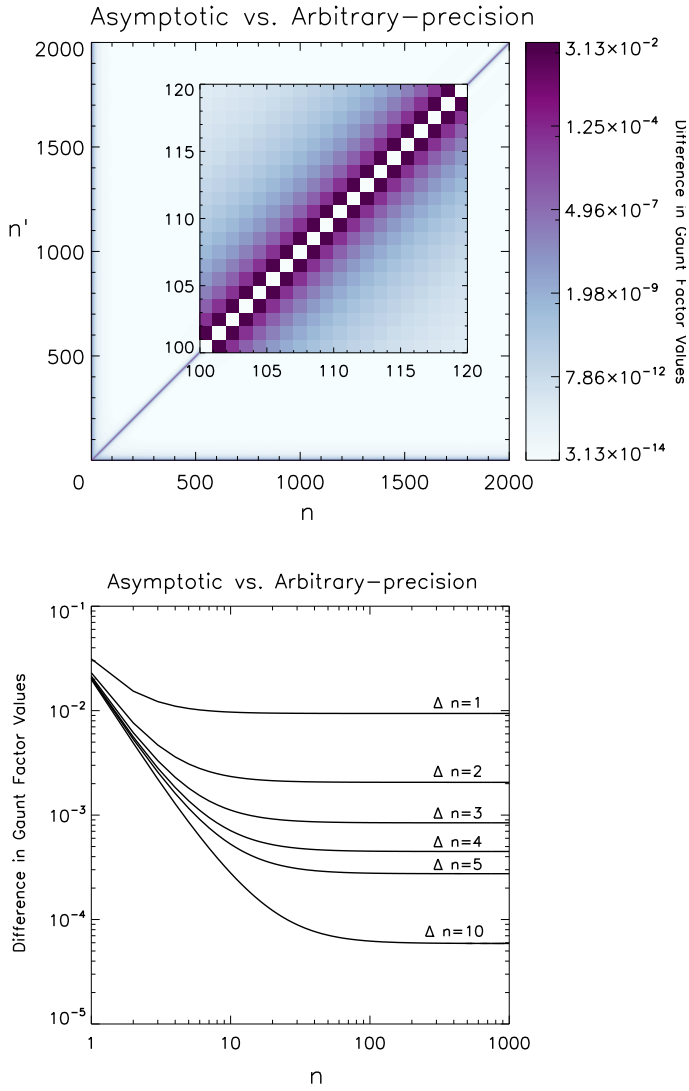

Figure 7.2: The absolute difference in values of the Gaunt factor as calculated by the Menzel & Pekeris (1935) asymptotic expansion and the analytic expression using arbitrary-precision. In the top panel, the darkest colors represent the largest differences. In the bottom panel, we plot the value of the difference against quantum number for several different values of $\Delta n = n - n'$. It is clear that the largest difference occurs for transitions between nearby ($n - n' \approx 1$) quantum levels.

levels available in NIST, and this comparison is shown in Fig. 7.3. The values from Storey & Hummer (1991) are the closest to the NIST values for these low levels, with larger scatter towards smaller changes in n. Although the relative difference is larger than that of Storey & Hummer (1991), the arbitrary-precision calculations presented here only have a relative difference of only $\sim 3 \times 10^{-4}$ from the NIST values. Therefore the arbitrary-precision values will introduce less than a tenth of per cent error into any final calculations we use them in. The scatter in the relative difference of the arbitrary-precision values of this work when compared to NIST values is of the order 10^{-5}, indicating that our results are also stable (i.e. differences in values of $n \rightarrow n'$ have only a very small effect on the relative difference from NIST values) and predictable. The asymptotic expansions by Malik et al. (1991) and Menzel & Pekeris (1935) are also fairly stable, with relative differences of 1×10^{-3} and 6×10^{-3}, respectively.

7.6 Conclusions

We have presented arbitrary-precision calculations of the Gaunt factor for transitions up to quantum level $n = 2000$, and shown that the improvement in accuracy is always at least an order of magnitude greater than the asymptotic expansions, when compared to the more complete simulations of NIST. The results of the calculations are stable and are at most only 0.03 per cent different from calculations that include relativistic corrections. The results are available for download as a FITS table. The Gaunt factor can be used for any atom to calculate spontaneous transition rates, and are therefore suitable for use by anyone working with recombination line spectra. In particular, these values fold linearly into our models of the cold neutral medium, proportionately propagating the improvement in spontaneous and stimulated transition rates.

The data is available as a FITS table from:
http://cdsarc.u-strasbg.fr/viz-bin/qcat?J/MNRAS/441/2855.

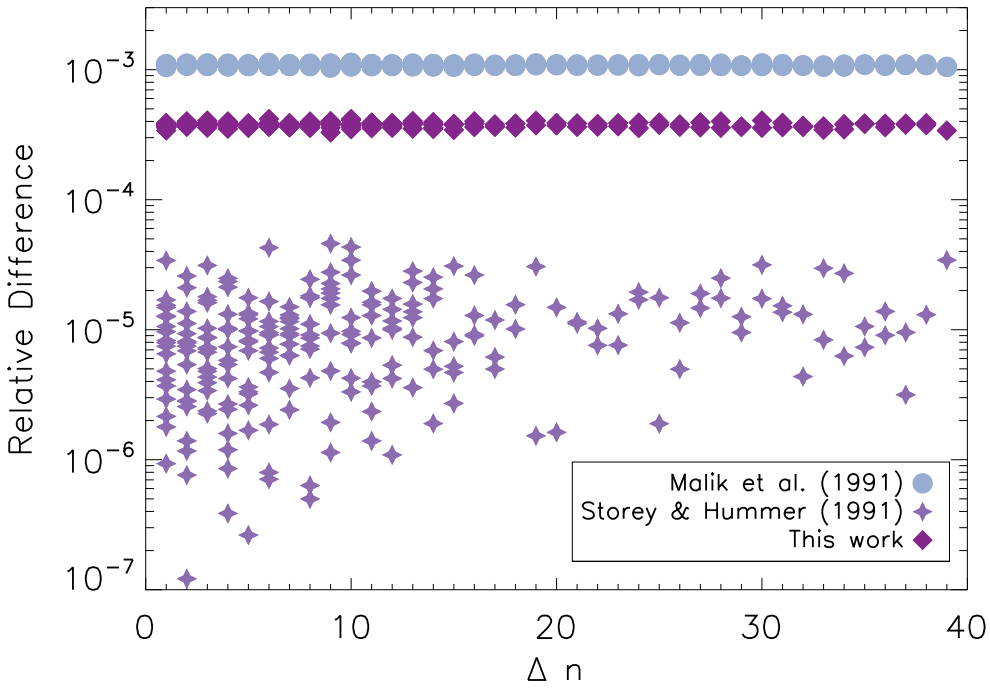

Figure 7.3: A comparison of the relative difference in two different methods and our arbitrary-precision Gaunt factor. The relative differences are calculated from values for spontaneous transition rates from NIST. These rates are linearly proportional to the Gaunt factor. Malik et al. (1991) use an asymptotic expansion, and Storey & Hummer (1991) use a recursion relation method.

APPENDIX A

Demixing LOFAR Long Baselines

A.1 Introduction

At low radio frequencies there are a few sources that dominate the sky. They are called the 'A-team' sources and include Cygnus A and Casseopeia A (and to a lesser extent Taurus A and Virgo A). The A-team sources have flux densities of thousands to tens of thousands of Janskys. Even when these bright sources are off-axis, they can still contribute significantly to the visibilities in an observation and their effects must be removed before the data can be used. This is done using a process called 'demixing' that relies on models of the A-team sources to predict their contribution to the visibilities (van der Tol et al., 2007). The demixing process is therefore only as good as the models of the A-team sources, which can be large (up to arcminutes) and have complex morphologies with flux on small scales (arcsec or less).

Ideally the A-team models would include components as compact as the highest resolution achievable with LOFAR, containing the correct fluxes for the LOFAR frequency range. The current A-team models are limited to either high-resolution models made at higher frequencies, or low-resolution models made at the appropriate frequencies. When demixing an LBA data set, I noticed that there was still some contribution from a nearby A-team source on the longest baselines, corresponding to the highest resolutions.

This appendix first describes the data reduction and inspection that led to uncovering this issue. Following that I show simulations which demonstrate that high-resolution models of A-team sources are necessary to properly demix baselines of all lengths.

A.2 Data Reduction and Inspection

The dataset consisted of a 6 hour simultaneous beam LBA observation taken on 15 June, 2013. The target was 3C 368 and the calibrator was Cygnus A. The continuous frequency coverage was 30 – 78 MHz for both target and calibrator. The data was pre-processed by the Radio Observatory (RO), including RFI flagging with the AOFlagger (Offringa, 2010) but not including demixing. I used the RO provided script to fix the beam information[1] and demixed Casseopeia A from the calibrator data set, and both Casseopeia A and Cygnus A from the target data set. The calibrator data were averaged to 1 channel per subband and 2 sec integration time and diagonal gain solutions were found using a model of Cygnus A made from HBA data (John McKean, private communication). The gain solutions were transferred to the target field, and the data were phase-only calibrated against the GSM.PY skymodel (described in the LOFAR Cookbook[2] for the Dutch array. These data were averaged to 1 channel per subband and 2 sec integration time.

Fig. A.1 shows the A-team elevation plotted for one hour of the observation, with the pointing also marked. For this observation, we had determined that Cas A and Cygnus A needed to be demixed. We used the standard ATEAM_LBA.SKYMODEL to demix.

Both the gains from the calibrator and the phase-only gains from the target were transferred to a separate target data set containing information from the international baselines. This data set had higher frequency resolution by a factor of 16. The international station visibility amplitudes were scaled by a factor of 120, thought to be appropriate from the SEFD. All core stations were combined into station TS001 using the Station Adder in the *new default pre-processing pipeline* (NDPPP), then core and remote stations were removed. Ten subbands (1.95 MHz) around the peak sensitivity of LOFAR (about 60 MHz) were converted to circular polarization using SIMPLE2CIRC.PY and combined into one measurement set, which was converted to uvfits format using MS2UVFITS. The data were then read into AIPS and indexed.

I used the AIPS task IBLED to perform baseline-based flagging to remove any lingering bad data in order to help the fringe fitting. I noticed that all baselines involving the superterp and either a DE or UK station clearly had beating and/or strongly time-varying amplitudes, see Fig. A.2. The maximum amplitudes reached are about 100 Jy.

[1] https://www.astron.nl/radio-observatory/observing-capabilities/depth-technical-information/system-notes/wrong-information-

[2] https://www.astron.nl/radio-observatory/lofar/lofar-imaging-cookbook

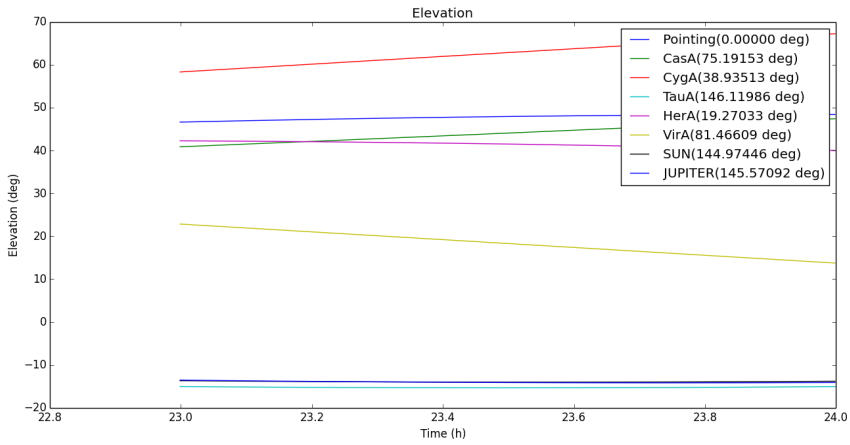

Figure A.1: A-team elevation plotted for the 1hr of observation that was simulated.

An inspection of the amplitude versus uv-distance showed that the first minimum occurs at a scale that corresponds to about 130 arcsec, which is roughly the size of Cygnus A. The beating is not evident on the international-to-international baselines, only on international-to-superterp baselines. In the case of the shortest international-to-international baseline, DE601-DE605, the baseline is only 52 km, and the models have sufficient resolution to demix this baseline. In the case of the other international-to-international baselines, there is either insufficient resolution in the the model, or not enough sensitivity, or a combination of both. I constructed a simulation to investigate this.

A.3 Demixing Simulation Input Models

In order to test whether the resolution of the skymodel used to demix can cause the beating we see on the international baselines, I constructed a simulation with a higher resolution A-team source. I split out an hour of the observation from one subband (corresponding to what is plotted in Fig. A.1). This provided a measurement set with the same date, times, and pointing phase center as the observation. I simulated a single point source at the phase center with a flux of 48 Jy, similar to 3C 368. I then constructed a model of a Cygnus A-like A-team source, i.e., two lobes, each with a compact hotspot. Using the coordinates of the hot spots of Cygnus A, I simulated two lobes, each with one point source and

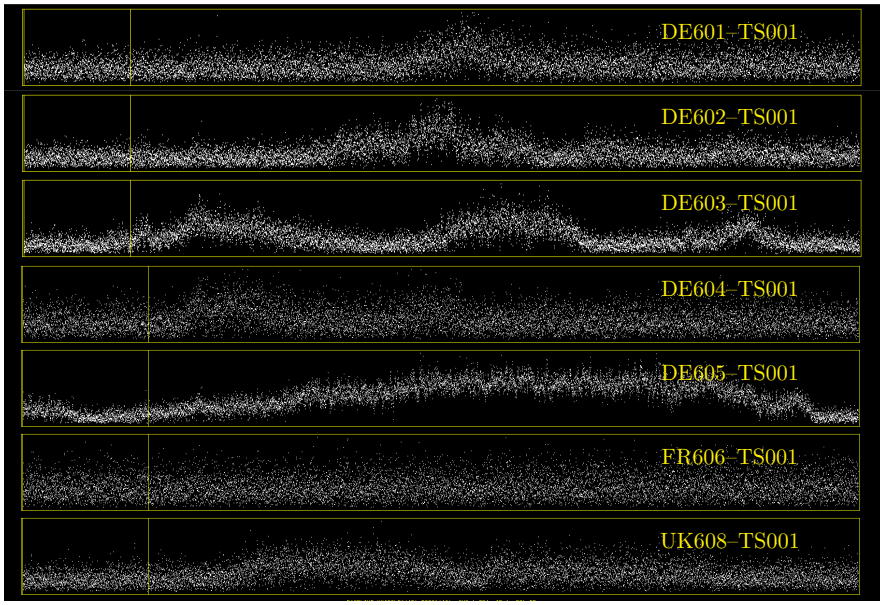

Figure A.2: Amplitude versus time for the entire six hour observation.

one Gaussian. A depiction is given in Fig. A.3 and the associated information is in Table A.1.

The simulations were performed with both beam and gain enabled. I then performed two separate demixing trials:

- **Trial 1:** Demixing the high-resolution model of the A-team source that I originally predicted.
- **Trial 2:** Demixing a low-resolution model that consists of the Gaussian components of the lobes only, but with total flux of Gaussian+point source

Table A.1: Model parameters

	Comp.	Major axis	Minor axis	flux
Lobe A	Gauss.	$20''$	$20''$	2,000 Jy
Lobe A	Point	–	–	8,000 Jy
Lobe B	Gauss.	$10''$	$10''$	1,000 Jy
Lobe B	Point	–	–	7,000 Jy

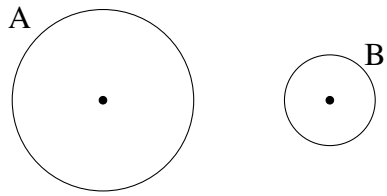

Figure A.3: Model of Cygnus A-like A-team source. The filled black circles are each one point in the model, and the open circles represent Gaussians. The model parameters are listed in Table 1.

(per lobe).

The two trials have the same total amount of flux, but allow for a comparison of the results of demixing with high- and low- resolution models.

A.4 Results

Fig. A.4 shows the results for a selection of core-to-international baselines. It is clear that the low-resolution model does not demix the flux of the A-team source, while the high-resolution model does. Demixing with the high-resolution model does leave some residuals, for example as seen on Baseline CS001LBA-DE602LBA just before time=500. I suspect that these residuals are a result of imperfect beam models.

A.5 Conclusions

The simulations show clearly that a low-resolution model cannot be used to demix baselines for which the resolution is better than the model. There are some residuals left over even after demixing the high-resolution model, which could be caused by imperfect beam models.

To enable proper demixing of long baselines for LOFAR, high-resolution models of the A-team sources will be necessary. Observations of the A-team sources with all LOFAR stations with both high band antenna (HBA) and LBA frequency ranges is the only way currently available to provide models with appropriate resolution for demixing all LOFAR baselines.

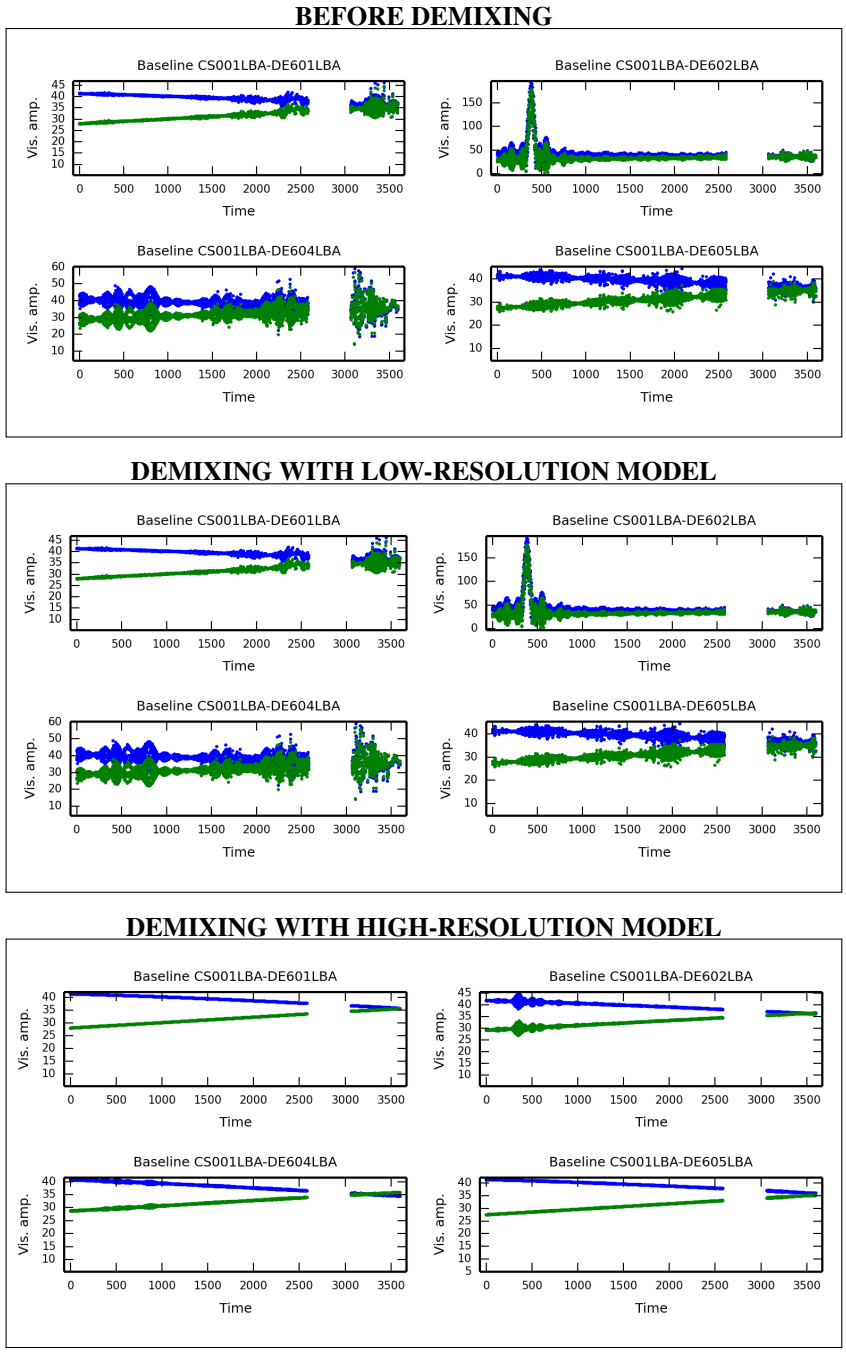

Figure A.4: Visibility amplitude versus time for a selection of baselines from the simulations.

APPENDIX B

The LOFAR Station Adder

B.1 Introduction

The 'StationAdder' step in the *new default pre-processing pipeline* (NDPPP) combines stations together by adding together visibilities from all baselines to a particular station. This is primarily used to increase the signal to noise ratio for baselines containing international stations by combining all of the core stations into a single 'Super' station. However, the long baseline working group has found that the StationAdder has provided images and/or calibration solutions that are noisier than expected. I have determined that this is at least partly due to the fact that while the documentation for NDPPP advertises that the weighted sum of visibilities is calculated for the output combined visibility, only the sum of visibilities is actually calculated.

This appendix outlines the steps taken to determine the problem, and shows the improvement when using the weighted sum of visibilities rather than the sum. A further improvement of ~ 1 per cent in image noise was found when using the weighted sum of the u, v, w coordinates.

B.2 Diagnosing the Problem

A single subband of a 15 minute LBA observation of 3C 147 that includes all international stations was used for this test. The data were first calibrated using the Black-Board Selfcal software (BBS; Pandey et al., 2009). Images were made before and after using the StationAdder to combine all core stations, and Fig. B.1 shows the difference in image quality. For the imaging, all of the shortest (core – core) baselines were flagged, and a uv-maximum of $15\,\mathrm{k}\lambda$ was used (i.e., no international stations). Only 10 iterations were used to make all images.

The image made with the uncombined stations has a noise level of $1.15\,\mathrm{Jy\,bm^{-1}}$. The image made with the StationAdder 'Super' station has a noise level of $1.58\,\mathrm{Jy\,bm^{-1}}$, almost 30% higher than before the stations were combined.

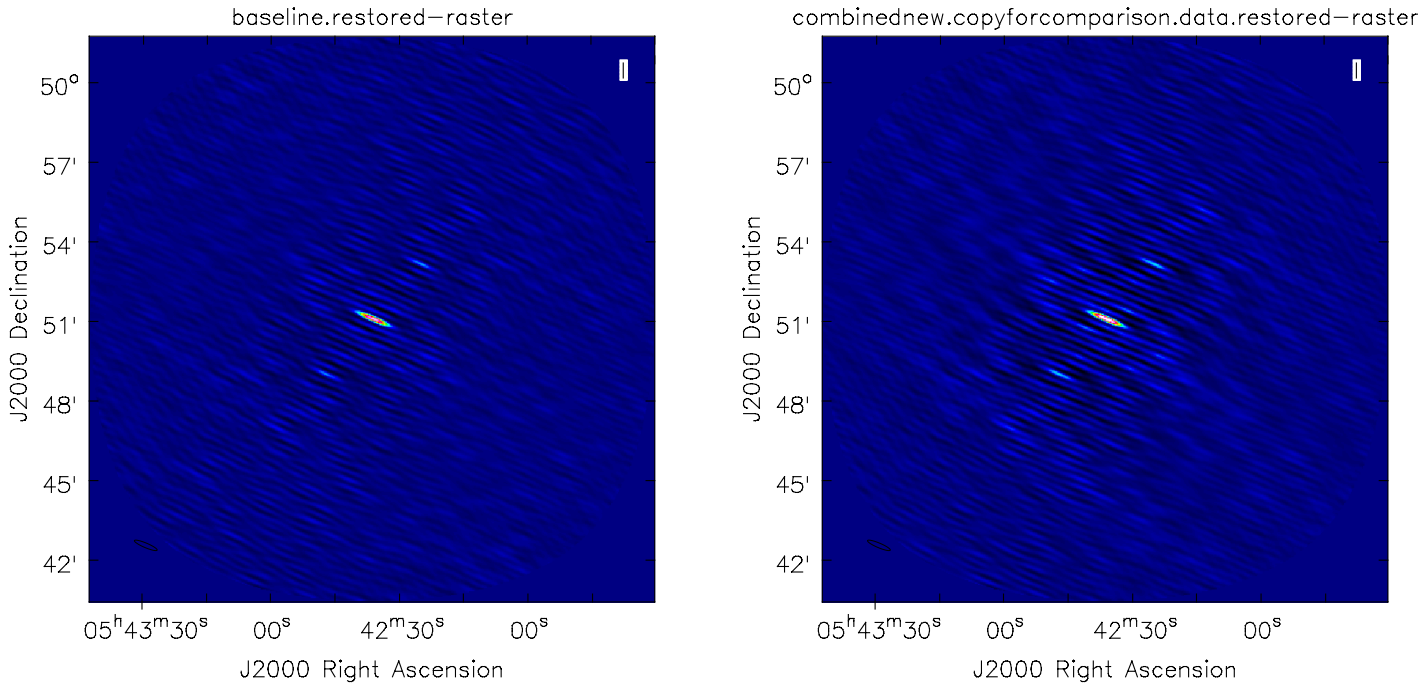

Figure B.1: *Left:* Image of 3C 147 with uncombined core stations. *Right:* Image of 3C 147 with all core stations combined using the NDPPP StationAdder step, and all core stations flagged afterwards. The color scale is the same for both images.

Comparison of individual visibilities using PLOTMS from the Common Astronomy Software Applications (CASA; McMullin et al., 2007) software package led me to believe that the new, combined visibility was merely the sum of the combined visibilities, rather than the weighted sum. To demonstrate this, I wrote a script[1] to read a measurement set containing both the uncombined and combined stations to find their corresponding visibility data. From the uncombined visibility data, both the sum and the weighted sum of the visibilities to be combined were calculated, and compared with the actual combined visibility values. The combined visibility weights are the straightforward sum of the weights of the uncombined visibilities, as expected. However, there is zero difference between the combined visibility value and the unweighted sum of the visibilities that were combined to create the new combined visibility. The difference between the calculated weighted sum of the visibilities to be combined and the combined visibility as calculated by the StationAdder is shown in an Argand diagram in Fig. B.2.

B.3 Fixing the Problem

To fix this problem, I wrote scripts[2] to calculate the correct weighted sum of visibilities, and additionally the weighted geometric center of the u, v, w coordinates of the visibilities being combined. This is different from the default method used by NDPPP to calculate the u, v, w coordinates. NDPPP first calculates the geographical position of the 'Super' station based on the longitude and latitude of the combined stations, and then re-calculates the u, v, w coordinates based on the station positions.

Figure B.3 shows a comparison of the uncombined, StationAdder combined, StationAdder combined + weighted sum corrected, and StationAdder combined + weighted sum corrected + weighted u, v, w coordinates calculated. The same imaging parameters were used for all images, and they are all set to the same color scale. For images using the combined 'Super' station, the core stations were flagged prior to imaging.

The difference in images can be seen by eye in Figure B.3, but the noise provides a quantitative measurement. Table B.1 lists the noise for each image, as calculated by the CASA task IMFIT.

While the final image with the correct weighted sum combined visibilities and weighted center of mass u, v, w coordinates only improves the noise by

[1] *show_weightedsum.py*, available upon request.

[2] *fix_weightedsum.py* and *fix_weightedsum_uvw.py*, available upon request.

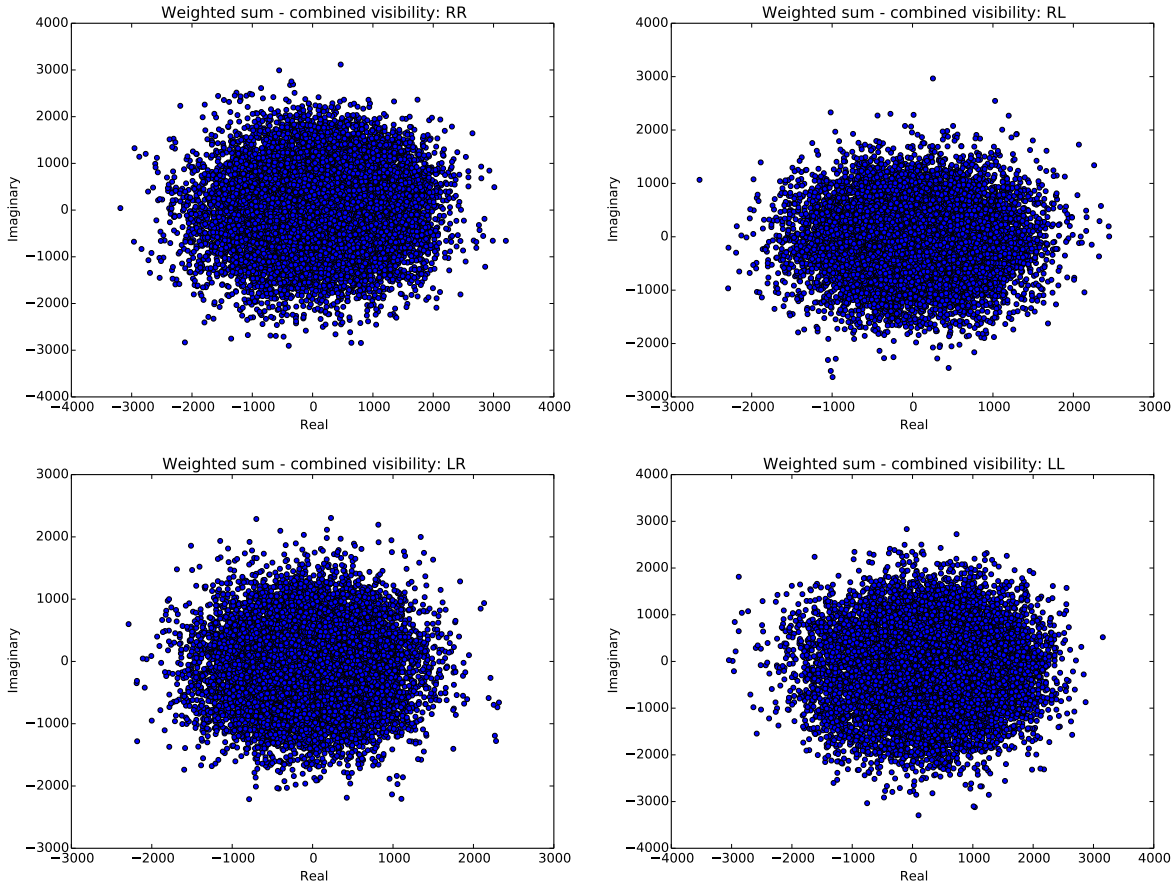

Figure B.2: The value of the weighted sum minus the value of the NDPPP StationAdder computed visibility, for the four different correlation products.

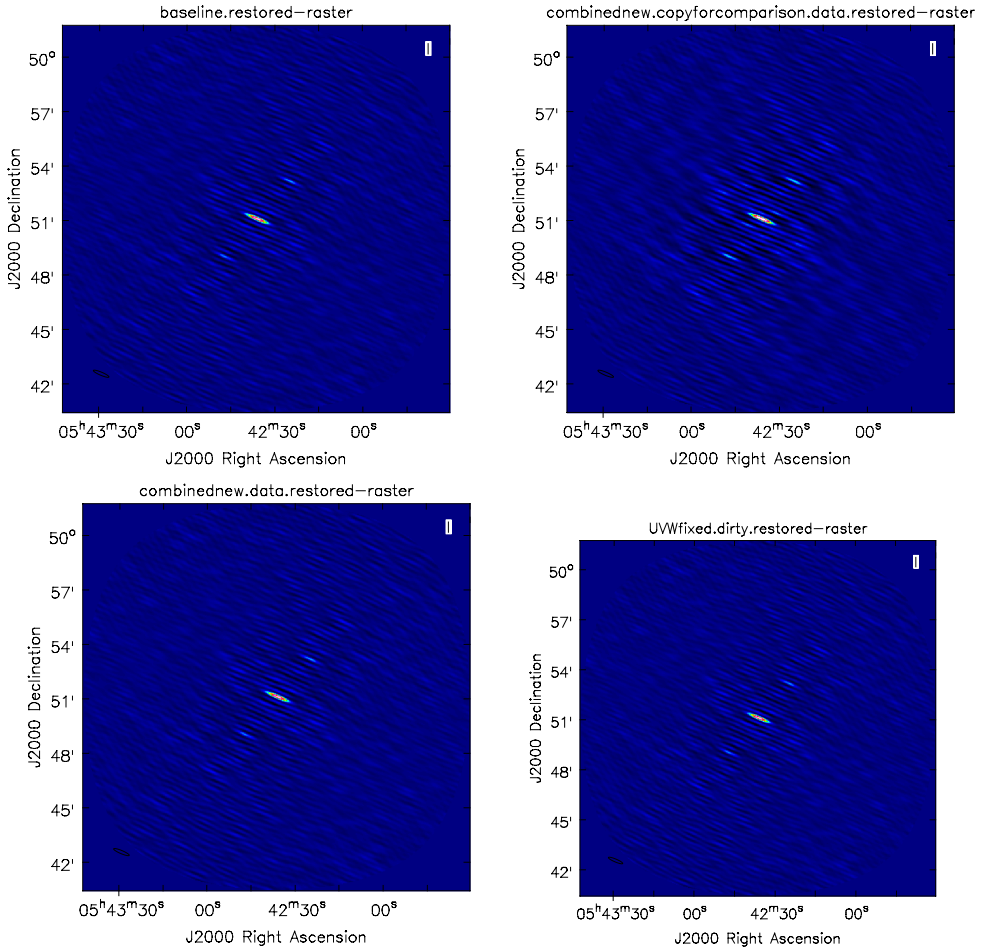

Figure B.3: *Top Left:* Uncombined core stations. *Top Right:* StationAdder combined 'Super' station. *Bottom Left:* StationAdder combined 'Super' station with the corrected weighted sum of visibilities. *Bottom Right:* Same as bottom left, but also with the corrected weighted center of mass of the u, v, w coordinates.

Table B.1: IMFIT calculated noise, $\mathrm{Jy\,bm^{-1}}$

Image	Image noise	Residual image noise
Uncombined	1.37797	1.14927
StationAdder	1.82356	1.57675
Weighted sum	1.37666	1.14932
Weighted sum, weighted uvw	1.36766	1.14101

$\sim 1\%$ when compared to the uncombined image, there is an almost 30% improvement over the image made using the NDPPP StationAdder step.

B.4 Conclusions

This appendix detailed a discrepancy in the NDPPP software and documentation: namely, that when combining stations using the StationAdder step, the weighted sum of the visibilities should be used, but NDPPP instead calculates the unweighted sum. This results in an increase in image noise of about 30%. A script was provided to fix this issue in measurement sets where the uncombined station visibilities still exist. Additionally, it was noticed that the new u, v, w coordinates of the new StationAdder combined visibilities were the unweighted geometric center of mass of the combining visibilities. A script was provided to fix this in addition to the visibility values themselves, and provides another $\sim 1\%$ improvement in image noise. The fixes have since been implemented in NDPPP (Software release 2.12.0).

Bibliography

Abramowitz M., Stegun I. A., 1972, Handbook of Mathematical Functions. Handbook of Mathematical Functions, New York: Dover, 1972

Adebahr B., Krause M., Klein U., Weżgowiec M., Bomans D. J., Dettmar R.-J., 2013, A&A, 555, A23

Anantharamaiah K. R., Zhao J.-H., Goss W. M., Viallefond F., 1993, ApJ, 419, 585

Anantharamaiah K. R., Erickson W. C., Payne H. E., Kantharia N. G., 1994, ApJ, 430, 682

Anderson L. D., Bania T. M., Balser D. S., Rood R. T., 2011, ApJS, 194, 32

Antonucci R. R. J., 1982, Nature, 299, 605

Antonucci R. R. J., 1984, ApJ, 278, 499

Antonucci R., 1993, ARA&A, 31, 473

Antonucci R. R. J., Ulvestad J. S., 1985, ApJ, 294, 158

Argo M. K., Pedlar A., Beswick R. J., Muxlow T. W. B., Fenech D. M., 2010, MNRAS, 402, 2703

Asgekar A., et al., 2013, A&A, 551, L11

Athreya R. M., Kapahi V. K., 1998, Journal of Astrophysics and Astronomy, 19, 63

Baade W., Minkowski R., 1954, ApJ, 119, 206

Baker J. C., Hunstead R. W., Kapahi V. K., Subrahmanya C. R., 1999, ApJS, 122, 29

Barthel P. D., 1989, ApJ, 336, 606

Barthel P. D., Hooimeyer J. R., Schilizzi R. T., Miley G. K., Preuss E., 1989, ApJ, 336, 601

Becker R. H., White R. L., Edwards A. L., 1991, ApJS, 75, 1

Bennett A. S., 1962, MNRAS, 125, 75

Bergemann M., Pickering J. C., Gehren T., 2010, MNRAS, 401, 1334

Best P. N., Heckman T. M., 2012, MNRAS, 421, 1569

Best P. N., Longair M. S., Röttgering H. J. A., 1997a, ArXiv Astrophysics e-prints,

Best P. N., Longair M. S., R"ottgering H. J. A., 1997b, ArXiv Astrophysics e-prints,

Best P. N., Röttgering H. J. A., Lehnert M. D., 1999, MNRAS, 310, 223

Best P. N., Kauffmann G., Heckman T. M., Ivezić Ž., 2005a, MNRAS, 362, 9

Best P. N., Kauffmann G., Heckman T. M., Brinchmann J., Charlot S., Ivezić Ž., White S. D. M., 2005b, MNRAS, 362, 25

Blanco V. M., Graham J. A., Lasker B. M., Osmer P. S., 1975, ApJL, 198, L63

Blumenthal G., Miley G., 1979, A&A, 80, 13

Blundell K. M., Rawlings S., Willott C. J., 1999, AJ, 117, 677

Bower R. G., Benson A. J., Malbon R., Helly J. C., Frenk C. S., Baugh C. M., Cole S., Lacey C. G., 2006, MNRAS, 370, 645

Bridle A. H., Schwab F. R., 1999, in Taylor G. B., Carilli C. L., Perley R. A., eds, Astronomical Society of the Pacific Conference Series Vol. 180, Synthesis Imaging in Radio Astronomy II. p. 371

Briggs D. S., 1995, in American Astronomical Society Meeting Abstracts. p. 1444

Brocklehurst M., Seaton M. J., 1972, MNRAS, 157, 179

Brown M. J. I., Dey A., Jannuzi B. T., Brand K., Benson A. J., Brodwin M., Croton D. J., Eisenhardt P. R., 2007, ApJ, 654, 858

Brown M. J. I., et al., 2008, ApJ, 682, 937

Burgess A., 1958, MNRAS, 118, 477

Carilli C. L., Perley R. A., Dreher J. W., Leahy J. P., 1991, ApJ, 383, 554

Carilli C. L., Röttgering H. J. A., van Ojik R., Miley G. K., Breugel W. J. M. van 1997, ApJS, 109, 1

Chambers K. C., Miley G. K., van Breugel W., 1987, Nature, 329, 604

Chambers K. C., Miley G. K., van Breugel W. J. M., 1990, ApJ, 363, 21

Cohen M. H., Ogle P. M., Tran H. D., Goodrich R. W., Miller J. S., 1999, AJ, 118, 1963

Cohen A. S., Lane W. M., Cotton W. D., Kassim N. E., Lazio T. J. W., Perley R. A., Condon J. J., Erickson W. C., 2007, AJ, 134, 1245

Condon J. J., Cotton W. D., Greisen E. W., Yin Q. F., Perley R. A., Taylor G. B., Broderick J. J., 1998, AJ, 115, 1693

Cotton W. D., 1995, in Zensus J. A., Diamond P. J., Napier P. J., eds, Astronomical Society of the Pacific Conference Series Vol. 82, Very Long Baseline Interferometry and the VLBA. p. 189

Cotton W. D., Condon J. J., Perley R. A., Kassim N., Lazio J., Cohen A., Lane W., Erickson W. C., 2004, in Oschmann Jr. J. M., ed., SPIEVol. 5489, Ground-based Telescopes. pp 180–189, doi:10.1117/12.551298

Cox A. N., 2000, Allen's astrophysical quantities

Dasyra K. M., Combes F., 2012, A&A, 541, L7

De Breuck C., van Breugel W., Röttgering H. J. A., Miley G., 2000, AAPS, 143, 303

Delone N. B., Goreslavsky S. P., Krainov V. P., 1994, Journal of Physics B Atomic Molecular Physics, 27, 4403

Dewangan D. P., 2002, Journal of Physics B Atomic Molecular Physics, 35, L427

Dewangan D. P., 2012, Phys. Rep., 511, 1

Donahue M., Smith B. J., Stocke J. T., 2002, AJ, 123, 1922

Douglas J. N., Bash F. N., Bozyan F. A., Torrence G. W., Wolfe C., 1996, AJ, 111, 1945

Dupree A. K., 1969, ApJ, 158, 491

Dy H.-B., 2009, Computer Physics Communications, 180, 2020

Edge D. O., Shakeshaft J. R., McAdam W. B., Baldwin J. E., Archer S., 1959, Memoirs of the RAS, 68, 37

Erickson W. C., McConnell D., Anantharamaiah K. R., 1995, ApJ, 454, 125

Evans D. A., Worrall D. M., Hardcastle M. J., Kraft R. P., Birkinshaw M., 2006, ApJ, 642, 96

Fanaroff B. L., Riley J. M., 1974, MNRAS, 167, 31P

Fenech D., Beswick R., Muxlow T. W. B., Pedlar A., Argo M. K., 2010, MNRAS, 408, 607

Ferrarese L., Merritt D., 2000, ApJL, 539, L9

Feruglio C., Maiolino R., Piconcelli E., Menci N., Aussel H., Lamastra A., Fiore F., 2010, A&A, 518, L155

Ficarra A., Grueff G., Tomassetti G., 1985, AAPS, 59, 255

Flannery M. R., Vrinceanu D., 2002, Phys. Rev. A, 65, 022703

Gandhi P., Isobe N., Birkinshaw M., Worrall D. M., Sakon I., Iwasawa K., Bamba A., 2011, PASJ, 63, 505

Garrington S. T., Leahy J. P., Conway R. G., Laing R. A., 1988, Nature, 331, 147

Gebhardt K., et al., 2000, ApJL, 539, L13

Gehrels N., 1986, ApJ, 303, 336

Gibbon T. B., et al., 2015, Journal of Astronomical Telescopes, Instruments, and Systems, 1, 028001

Golynkin A. A., Konovalenko A. A., 1991, Soviet Astronomy Letters, 17, 7

Gounand F., Petitjean L., 1984, Phys. Rev. A, 30, 61

Gower J. F. R., Scott P. F., Wills D., 1967, Memoirs of the RAS, 71, 49

Gradshteyn I. S., Ryzhik I. M., Jeffrey A., Zwillinger D., 2007, Table of Integrals, Series, and Products. Seventh Edition by I. S. Gradshteyn, I. M. Ryzhik, Alan Jeffrey, and Daniel Zwillinger. Elsevier Academic Press, 2007. ISBN 012-373637-4

Greisen E. W., 2003, Information Handling in Astronomy - Historical Vistas, 285, 109

Grimes J. A., Rawlings S., Willott C. J., 2004, MNRAS, 349, 503

Gültekin K., et al., 2009, ApJ, 698, 198

Hales C. A., Middelberg E., 2014, Astrophysics Source Code Library, record ascl:1408.014

Hales S. E. G., Baldwin J. E., Warner P. J., 1993, MNRAS, 263, 25

Hardcastle M. J., Evans D. A., Croston J. H., 2006, MNRAS, 370, 1893

Hardcastle M. J., Evans D. A., Croston J. H., 2007, MNRAS, 376, 1849

Hardcastle M. J., et al., 2013, MNRAS, 429, 2407

Harwood J. J., Hardcastle M. J., Croston J. H., Goodger J. L., 2013, MNRAS, 435, 3353

Harwood J. J., Hardcastle M. J., Croston J. H., 2015, MNRAS, 454, 3403

Haslam C. G. T., Salter C. J., Stoffel H., Wilson W. E., 1982, AAPS, 47, 1

Hatch N. A., et al., 2011, MNRAS, 410, 1537

Heiles C., Troland T. H., 2003, ApJS, 145, 329

Hine R. G., Longair M. S., 1979, MNRAS, 188, 111

Ho L. C., 2008, ARA&A, 46, 475

Humphrey A., Villar-Martín M., Fosbury R., Vernet J., di Serego Alighieri S., 2006, MNRAS, 369, 1103

Humphrey A., Villar-Martín M., Fosbury R., Binette L., Vernet J., De Breuck C., di Serego Alighieri S., 2007, MNRAS, 375, 705

Infeld L., Hull T. E., 1951, Reviews of Modern Physics, 23, 21

Inskip K. J., Best P. N., Longair M. S., Röttgering H. J. A., 2005, MNRAS, 359, 1393

Inskip K. J., Villar-Martín M., Tadhunter C. N., Morganti R., Holt J., Dicken D., 2008, MNRAS, 386, 1797

Intema H. T., 2014, preprint, (arXiv:1402.4889)

Intema H. T., van der Tol S., Cotton W. D., Cohen A. S., van Bemmel I. M., Röttgering H. J. A., 2009, A&A, 501, 1185

Intema H. T., Jagannathan P., Mooley K. P., Frail D. A., 2016, preprint, (arXiv:1603.04368)

Jackson N., Rawlings S., 1997, MNRAS, 286, 241

Jackson N., Tadhunter C., Sparks W. B., 1998, MNRAS, 301, 131

Jacobs B. A., Rizzi L., Tully R. B., Shaya E. J., Makarov D. I., Makarova L., 2009, AJ, 138, 332

Jannuzi B. T., Dey A., 1999, in Bunker A. J., van Breugel W. J. M., eds, Astronomical Society of the Pacific Conference Series Vol. 193, The Hy-Redshift Universe: Galaxy Formation and Evolution at High Redshift. p. 258

Jansky K. G., 1933, Popular Astronomy, 41, 548

Johnston S., et al., 2007, PASA, 24, 174

Kaiser C. R., Best P. N., 2007, MNRAS, 381, 1548

Kantharia N. G., Anantharamaiah K. R., 2001, Journal of Astrophysics and Astronomy, 22, 51

Kapahi V. K., Athreya R. M., van Breugel W., McCarthy P. J., Subrahmanya C. R., 1998a, ApJS, 118, 275

Kapahi V. K., Athreya R. M., Subrahmanya C. R., Baker J. C., Hunstead R. W., McCarthy P. J., van Breugel W., 1998b, ApJS, 118, 327

Kazemi S., Yatawatta S., Zaroubi S., Lampropoulos P., de Bruyn A. G., Koopmans L. V. E., Noordam J., 2011, MNRAS, 414, 1656

Kellermann K. I., Pauliny-Toth I. I. K., Williams P. J. S., 1969, ApJ, 157, 1

Kepley A. A., Leroy A. K., Frayer D., Usero A., Marvil J., Walter F., 2014, ApJL, 780, L13

Ker L. M., Best P. N., Rigby E. E., Röttgering H. J. A., Gendre M. A., 2012, MNRAS, 420, 2644

Klamer I. J., Ekers R. D., Bryant J. J., Hunstead R. W., Sadler E. M., De Breuck C., 2006, MNRAS, 371, 852

Kochanek C. S., et al., 2012, ApJS, 200, 8

Konovalenko A. A., Sodin L. G., 1980, Nature, 283, 360

Konovalenko A. A., Sodin L. G., 1981, Nature, 294, 135

Konovalenko A. A., Stepkin S. V., 2005, in Gurvits L. I., Frey S., Rawlings S., eds, EAS Publications Series Vol. 15, EAS Publications Series. pp 271–295, doi:10.1051/eas:2005158

Kormendy J., Richstone D., 1995, ARA&A, 33, 581

Kramida A., Ralchenko Y., Reader J., 2012, NIST Atomic Spectra Database (version 5.0). NIST ASD Team, National Institute of Standards and Technology, Gaithersburg, MD.

Kraus M., Krügel E., Thum C., Geballe T. R., 2000, A&A, 362, 158

Krolik J. H., Chen W., 1991, AJ, 102, 1659
Laing R. A., Riley J. M., Longair M. S., 1983, MNRAS, 204, 151
Larson R. B., 2010, Nature Physics, 6, 96
Linsky J. L., Rickett B. J., Redfield S., 2008, ApJ, 675, 413
Lo K. Y., Cheung K. W., Masson C. R., Phillips T. G., Scott S. L., Woody D. P., 1987, ApJ, 312, 574
Magorrian J., et al., 1998, AJ, 115, 2285
Malik G. P., Malik U., Varma V. S., 1991, ApJ, 371, 418
Marconi A., Hunt L. K., 2003, ApJL, 589, L21
McCarthy P. J., 1991, AJ, 102, 518
McCarthy P. J., van Breugel W., Spinrad H., Djorgovski S., 1987, ApJL, 321, L29
McDonald A. R., Muxlow T. W. B., Wills K. A., Pedlar A., Beswick R. J., 2002, MNRAS, 334, 912
McKean et al. 2016, MNRAS, submitted
McMullin J. P., Waters B., Schiebel D., Young W., Golap K., 2007, in Shaw R. A., Hill F., Bell D. J., eds, Astronomical Society of the Pacific Conference Series Vol. 376, Astronomical Data Analysis Software and Systems XVI. p. 127
Menzel D. H., Pekeris C. L., 1935, MNRAS, 96, 77
Middelberg E., 2006, PASA, 2, 64
Miley G. K., 1968, Nature, 218, 933
Miley G., De Breuck C., 2008, A&ARv, 15, 67
Mohan N., Rafferty D., 2015, Astrophysics Source Code Library, record ascl:1502.007
Moldón J., et al., 2015, A&A, 574, A73
Morabito L. K., et al., 2014, ApJL, 795, L33
Morabito L. K., et al., 2016, MNRAS, 461, 2676
Moran J. M., Dhawan V., 1995, in Zensus J. A., Diamond P. J., Napier P. J., eds, Astronomical Society of the Pacific Conference Series Vol. 82, Very Long Baseline Interferometry and the VLBA. p. 161
Motohara K., et al., 2000, PASJ, 52, 33
Muxlow T. W. B., Pedlar A., Wilkinson P. N., Axon D. J., Sanders E. M., de Bruyn A. G., 1994, MNRAS, 266, 455
Narayan R., Yi I., 1994, ApJL, 428, L13
Naylor B. J., et al., 2010, ApJ, 722, 668
Neeser M. J., Eales S. A., Law-Green J. D., Leahy J. P., Rawlings S., 1995, ApJ, 451, 76

Offringa A. R., 2010, AOFlagger: RFI Software, Astrophysics Source Code Library (ascl:1010.017)
Offringa A. R., et al., 2013, A&A, 549, A11
Ogle P. M., Cohen M. H., Miller J. S., Tran H. D., Fosbury R. A. E., Goodrich R. W., 1997, ApJL, 482, L37
Ogle P., Whysong D., Antonucci R., 2006, ApJ, 647, 161
Omidvar K., McAllister A. M., 1995, Phys. Rev. A, 51, 1063
Oonk J. B. R., et al., 2014, MNRAS, 437, 3506
Pacholczyk A. G., 1970, Radio astrophysics. Nonthermal processes in galactic and extragalactic sources
Palmer P., 1967, ApJ, 149, 715
Pandey V. N., van Zwieten J. E., de Bruyn A. G., Nijboer R., 2009, in Saikia D. J., Green D. A., Gupta Y., Venturi T., eds, Astronomical Society of the Pacific Conference Series Vol. 407, The Low-Frequency Radio Universe. p. 384
Pauliny-Toth I. I. K., Wade C. M., Heeschen D. S., 1966, ApJS, 13, 65
Payne H. E., Anantharamaiah K. R., Erickson W. C., 1989, ApJ, 341, 890
Payne H. E., Anantharamaiah K. R., Erickson W. C., 1994, ApJ, 430, 690
Pearson T. J., Readhead A. C. S., 1984, ARA&A, 22, 97
Pentericci L., Röttgering H. J. A., Miley G. K., Spinrad H., McCarthy P. J., van Breugel W. J. M., Macchetto F., 1998, ApJ, 504, 139
Pentericci L., Röttgering H. J. A., Miley G. K., McCarthy P., Spinrad H., van Breugel W. J. M., Macchetto F., 1999, A&A, 341, 329
Pentericci L., Van Reeven W., Carilli C. L., Röttgering H. J. A., Miley G. K., 2000a, AAPS, 145, 121
Pentericci L., et al., 2000b, A&A, 361, L25
Perley R. A., Napier P. J., Butler B. J., 2004, in Oschmann Jr. J. M., ed., SPIE Vol. 5489, Ground-based Telescopes. pp 784–795, doi:10.1117/12.551557
Perley R. A., Chandler C. J., Butler B. J., Wrobel J. M., 2011, ApJL, 739, L1
Pilkington J. D. H., Scott J. F., 1965, Memoirs of the RAS, 69, 183
Planck Collaboration et al., 2015, preprint, (arXiv:1502.01589)
Ponomarev V. O., Sorochenko R. L., 1992, Soviet Astronomy Letters, 18, 215
Poppi S., Tsivilev A. P., Cortiglioni S., Palumbo G. G. C., Sorochenko R. L., 2007, A&A, 464, 995
Press W. H., Flannery B. P., Teukolsky S. A., 1986, Numerical recipes. The art of scientific computing. Cambridge: University Press, 1986
Quataert E., 2001, in Peterson B. M., Pogge R. W., Polidan R. S., eds, Astronomical Society of the Pacific Conference Series Vol. 224, Probing the Physics of Active Galactic Nuclei. p. 71

Quirrenbach A., 1992, in Klare G., ed., Reviews in Modern Astronomy Vol. 5, Variability and VLBI Observations of Extragalactic Radio Surces. pp 214–228
Reber G., 1949, S&T, 8
Rickett B. J., 1986, ApJ, 307, 564
Rigby E. E., Best P. N., Brookes M. H., Peacock J. A., Dunlop J. S., Röttgering H. J. A., Wall J. V., Ker L., 2011, MNRAS, 416, 1900
Rodriguez-Rico C. A., Viallefond F., Zhao J.-H., Goss W. M., Anantharamaiah K. R., 2004, ApJ, 616, 783
Roelfsema P. R., Goss W. M., 1991, AAPS, 87, 177
Roelfsema P. R., Goss W. M., Wilson T. L., 1987, A&A, 174, 232
Roelfsema P. R., Goss W. M., Mallik D. C. V., 1992, ApJ, 394, 188
Roger R. S., Costain C. H., Stewart D. I., 1986, AAPS, 65, 485
Röttgering H. J. A., Lacy M., Miley G. K., Chambers K. C., Saunders R., 1994, AAPS, 108
Roy A. L., Goss W. M., Anantharamaiah K. R., 2008, A&A, 483, 79
Ryle M., 1962, Nature, 194, 517
Ryle M., Vonberg D. D., 1946, Nature, 158, 339
Salem M., Brocklehurst M., 1979, ApJS, 39, 633
Salgado et al. 2016a, ApJ, submitted
Salgado et al. 2016b, ApJ, accepted
Salvini S., Wijnholds S. J., 2014, A&A, 571, A97
Sandage A., 1965, ApJ, 141, 1560
Savitzky A., Golay M. J. E., 1964, Analytical Chemistry, 36, 1627
Scaife A. M. M., Heald G. H., 2012, MNRAS, 423, L30
Schilizzi R. T., 2005, in Gurvits L. I., Frey S., Rawlings S., eds, EAS Publications Series Vol. 15, EAS Publications Series. pp 445–463, doi:10.1051/eas:2005170
Schmidt G. D., Smith P. S., 2000, ApJ, 545, 117
Seaton M. J., 1964, MNRAS, 127, 177
Seaton M. J., 1985, Journal of Physics B Atomic Molecular Physics, 18, 2111
Shakura N. I., Sunyaev R. A., 1973, A&A, 24, 337
Shaver P. A., 1975a, Pramana, 5, 1
Shaver P. A., 1975b, A&A, 43, 465
Shaver P. A., 1976, A&A, 49, 1
Shaver P. A., 1978, A&A, 68, 97
Shaver P. A., Churchwell E., Rots A. H., 1977, A&A, 55, 435
Silk J., Nusser A., 2010, ApJ, 725, 556

Singal A. K., 2014, AJ, 148, 16
Singal A. K., Singh R. L., 2013, MNRAS, 435, L38
Smirnov O. M., Tasse C., 2015, MNRAS, 449, 2668
Smith D. J. B., 2015, preprint, (arXiv:1506.05630)
Smith H. E., Spinrad H., 1980, PASP, 92, 553
Sofia U. J., Cardelli J. A., Guerin K. P., Meyer D. M., 1997, ApJL, 482, L105
Stepkin S. V., Konovalenko A. A., Kantharia N. G., Udaya Shankar N., 2007, MNRAS, 374, 852
Stern D., et al., 2005, ApJ, 631, 163
Storey P. J., Hummer D. G., 1991, Computer Physics Communications, 66, 129
Tadhunter C., Morganti R., Rose M., Oonk J. B. R., Oosterloo T., 2014, Nature, 511, 440
Tasse C., Best P. N., Röttgering H., Le Borgne D., 2008, A&A, 490, 893
Tasse C., van der Tol S., van Zwieten J., van Diepen G., Bhatnagar S., 2013, A&A, 553, A105
Taylor M. B., 2005, in Shopbell P., Britton M., Ebert R., eds, Astronomical Society of the Pacific Conference Series Vol. 347, Astronomical Data Analysis Software and Systems XIV. p. 29
Taylor G. B., 2007, Highlights of Astronomy, 14, 388
The Opactiy Project Team 1995, The Opacity Project Vol. 1.. Institute of Physics Publications, Bristol, UK
Thompson A. R., Moran J. M., Swenson Jr. G. W., 2001, Interferometry and Synthesis in Radio Astronomy, 2nd Edition. 2nd ed. New York : Wiley, c2001.xxiii, 692 p. : ill. ; 25 cm. "A Wiley-Interscience publication." Includes bibliographical references and indexes. ISBN : 0471254924"
Tielens A. G. G. M., Miley G. K., Willis A. G., 1979, AAPS, 35, 153
Tingay S. J., et al., 2013, PASA, 30, e007
Urry C. M., Padovani P., 1995, PASP, 107, 803
Varenius E., et al., 2015, A&A, 574, A114
Varenius et al. 2016, A&A, submitted
Villar-Martín M., Binette L., Fosbury R. A. E., 1999, A&A, 346, 7
Villar-Martín M., Vernet J., di Serego Alighieri S., Fosbury R., Humphrey A., Pentericci L., 2003, MNRAS, 346, 273
Viner M. R., Erickson W. C., 1975, AJ, 80, 931
Walmsley C. M., Watson W. D., 1982, ApJ, 260, 317
Wardle J. F. C., Miley G. K., 1974, A&A, 30, 305
Weiß A., et al., 2010, A&A, 521, L1
Weliachew L., Fomalont E. B., Greisen E. W., 1984, A&A, 137, 335

Werner N., et al., 2014, MNRAS, 439, 2291
Westmoquette M. S., Smith L. J., Gallagher J. S., Walter F., 2013, MNRAS, 428, 1743
White R. L., Becker R. H., 1992, ApJS, 79, 331
White G. J., Ellison B., Claude S., Dent W. R. F., Matheson D. N., 1994, A&A, 284, L23
Whittaker E. T., Watson G. N., 1963, A course of modern analysis. Cambridge: University Press, |c1963, 4th ed.
Whysong D., Antonucci R., 2004, ApJ, 602, 116
Wiese W. L., Fuhr J. R., 2007, Journal of Physical and Chemical Reference Data, 36, 1287
Williams W. L., 2015, PhD thesis, Leiden University
Williams W. L., et al., 2016, preprint, (arXiv:1605.01531)
Willott C. J., Rawlings S., Blundell K. M., Lacy M., 1999, MNRAS, 309, 1017
Wills K. A., Pedlar A., Muxlow T. W. B., Wilkinson P. N., 1997, MNRAS, 291, 517
Wills K. A., Pedlar A., Muxlow T. W. B., 1998, MNRAS, 298, 347
Wolfram Research, Inc. 2010, Mathematica Edition: Version 8.0. Champaign, Illinois: Wolfram Research, Inc.
Wright E. M., 1935, Journal of the London Mathematical Society, 4, 286
Wucknitz O., 2010, in ISKAF2010 Science Meeting. p. 58 (arXiv:1008.4358)
Yatawatta S., et al., 2013, A&A, 550, A136
Yun M. S., Ho P. T. P., Lo K. Y., 1993, ApJL, 411, L17
de Vries W. H., Morganti R., Röttgering H. J. A., Vermeulen R., van Breugel W., Rengelink R., Jarvis M. J., 2002, AJ, 123, 1784
van Breugel W., De Breuck C., Stanford S. A., Stern D., Röttgering H., Miley G., 1999, ApJL, 518, L61
van Haarlem M. P., et al., 2013, A&A, 556, A2
van Weeren R. J., et al., 2016, ApJS, 223, 2
van der Tol S. ., Jeffs B. D., van der Veen A.-J. ., 2007, IEEE Transactions on Signal Processing, 55, 4497

Samenvatting

Actieve Sterrenstelsels

In het hart van bijna elk massief sterrenstelsel bevindt zich een zwart gat dat miljoenen tot miljarden keren zwaarder is dan onze Zon. De meeste sterrenstelsels bevatten 'slapende' zwarte gaten. In een fractie van sterrenstelsels ziet men zwarte gaten in interactie met hun gaststerrenstelsels, waarbij gas wordt ingevangen in een heldere hete schijf van verzamelend materiaal, dat rond hen spiraalt als water in het afvoerputje van een badkuip. Wanneer het zwarte gat van een sterrenstelsel op deze manier wordt gevoed, dan noemt men het sterrenstelsel 'actief'. De schijf van verzamelend materiaal rond het zwarte gat is klein vergeleken met de grootte van het hele sterrenstelsel, maar kan genoeg zichtbaar licht produceren om de rest van het sterrenstelsel te overschijnen. Het heldere licht afkomstig van deze compacte schijf ziet er voor een waarnemer op Aarde uit als een puntbron, vergelijkbaar met een ster. Vandaar dat men dit ook quasi-stellaire bronnen of *quasars* noemt. Actieve sterrenstelsels hebben een variatie aan verschillende kenmerken, en niet alle zijn quasars. De schijf van verzamelend materiaal kan omgeven zijn door stoffig moleculair gas. Dit stoffige gas wordt warmer als het licht afkomstig van de schijf absorbeert en het gloeit hierdoor helder in het infrarood. Aangezien alles aan de hemel slechts in twee dimensies (en niet drie) door ons wordt waargenomen, kan het stoffige gas afhankelijk van de orientatierichting van het sterrenstelsel soms het licht van de schijf blokkeren. Zelfs als wij weten dat een sterrenstelsel actief is, kunnen wij dan geen quasar zien. Er zijn ook andere observationele kenmerken die eveneens afhangen van de orientatierichting, en sterrenkundigen gebruiken daarom meerdere aanwijzingen om actieve sterrenstelsels te identificeren. Figuur 1 laat een diagram zien van het zwarte gat en het omliggende gebied in een radioluid actief sterrenstelsel.

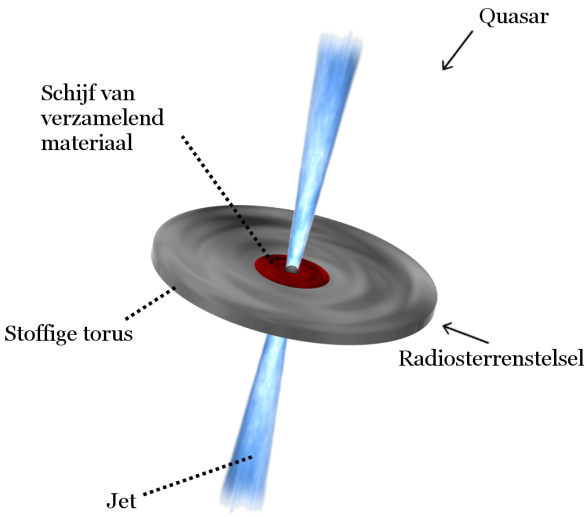

Figuur 1: Een diagram van het zwarte gat en het omliggende gebied in een actief sterrenstelsel. De straalstroom is slechts in ongeveer 10 procent van de actieve sterrenstelsels aanwezig. Deze stelsels noemt men 'radioluid'. Actieve sterrenstelsels kunnen verschillende waargenomen kenmerken hebben, afhankelijk van de orientatie ten opzichte van de waarnemer. De pijlen geven aan welk type object (afhankelijk van de kijkhoek) wordt gezien. Afbeelding afkomstig van J. Harwood.

Radiosterrenstelsels

Ongeveer 10 procent van actieve stelsels produceert straalstromen (ofwel 'jets') van plasma dat met relativistische snelheden beweegt. Deze straalstromen genereren radiostraling vanwege spiralende electronen in magneetvelden; een proces dat men synchrotronstraling noemt. Deze heldere krachtige jets bestaan uit twee klassen met duidelijk verschillende morfologische eigenschappen. Figuur 2 laat voorbeelden zien van de twee verschillende klassen: Fanaroff-Riley I (FR I) bronnen, die radiojets bevatten die meer op fonteinen lijken, met brede jets die zwakker worden richting de rand; en Fanaroff-Riley II (FR II) bronnen, die zeer gerichte radiojets hebben en het helderst zijn op het uiteinde van de jet.

Van verre radiosterrenstelsels wordt vermoed dat zij evolueren tot de meest massieve sterrenstelsels in het huidige heelal, en vaak bevat de ruimte rond hen meer sterrenstelsels dan verwacht. Daarom zijn deze stelsels belangrijke indicators om de evolutie van sterrenstelsels te bestuderen. Vooral ook omdat populaties van sterrenstelsels bestudeerd kunnen worden terwijl zij de overgang maken naar clusters van sterrenstelsels, de grootste gravitationeel gebonden objecten in het heelal.

De verst afgelegen radiosterrenstelsels hebben eigenschappen die verschil-

Figuur 2: Voorbeelden van typische Fanaroff-Riley FRI en FRII bronnen. *Links:* FRI radiosterrenstelsel Centaurus A. De kleur paars laat de radio-emissie zien (Bronnen: Röntgen: NASA/CXC/CfA/R.Kraft et al; Radio: NSF/VLA/Univ.Hertfordshire/M.Hardcastle; Optisch: ESO/WFI/M.Rejkuba et al.). *Rechts:* Cygnus A, het archetypale FRII radiosterrenstelsel. De kleur rood laat de radio-emissie met typische heldere rand zien. (Bronnen: Röntgen: NASA/CXC/SAO; Optisch: NASA/STScI; Radio: NSF/NRAO/AUI/VLA).

len van lokale radiosterrenstelsels en het is niet duidelijk of deze verschillen intrinsiek zijn of aan omgevingsfactoren liggen. Een van de meest intrigerende verschillen tussen lokale en verre radiostelsels is dat hoe verder een radiostelsels ligt, hoe steiler zijn radiospectrum is (de maat van steilheid is de spectrale index parameter, α). De relatie tussen de spectrale index in het radiogebied en de roodverschuiving (een astronomische afstandsmaat) is in het verleden succesvol toegepast om de verst afgelegen radiosterrenstelsels te vinden. Desondanks is de oorzaak van deze relatie onbekend.

Koolstof-radio-recombinatielijnen

De cyclus van sterformatie speelt een belangrijke rol in de evolutie van een sterrenstelsel. Het interstellair medium (ISM) levert de brandstof om nieuwe sterren te maken en is de verzamelplaats voor uitgestoten materiaal van oude sterren. Er zijn veel verschillende componenten in het ISM, en doorkrijgen hoe deze componenten bijdragen aan stervorming is van uiterst belang om de evolutie van sterrenstelsels te begrijpen. Een van de minst bekende onderdelen van het ISM is het koude neutrale medium, dat meer dan 10^{19} keer minder dicht is dan de lucht op Aarde en dat tevens een paar honderd graden onder nul is. Dit nevelachtige gas bestaat met name uit neutrale waterstofatomen en koolstofatomen

die eenmaal geioniseerd zijn (dat wil zeggen een electron missen).

Koolstofatomen hebben normaal zes protonen en zes electronen en zijn ongeveer een half miljoen keer kleiner dan de gemiddelde dikte van een menselijk haar. Het buitenste electron is redelijk makkelijk uit zijn baan te schieten door laagenergetische ultravioletstraling, waarna een eenmaal geioniseerd koolstofatoom overblijft. In het koude neutrale medium leven deze koolstofatomen samen met vrije electronen en neutrale waterstofatomen. De vrije electronen kunnen opnieuw ingevangen worden door de koolstofionen in een proces dat recombinatie heet (Figuur 3 laat een diagram zien van recombinatie). Op het moment dat deze recombinatie plaatsvindt naar een hoog energieniveau ($n \geq 300$), worden spectrale kenmerken gegenereerd op lage radiofrequenties ($\leq 240\,\mathrm{MHz}$). Er zijn veel van deze koolstof-radio-recombinatielijnen (CRRLs) in het radiofrequentiegebied maar zij zijn het sterkst in de FM-radioband.

Het waarnemen van CRRLs op lage frequenties heeft drie grote voordelen. Ten eerste zijn zij makkelijk waar te nemen omdat de spectrale kenmerken (door de achterliggende fysische processen) sterker zijn. Ten tweede liggen de lijnen dichter bij elkaar op lage frequenties en daardoor kunnen instrumenten met een breed golflengtebereik meerdere CRRLs tegelijkertijd waarnemen. Meerdere CRRLs gelijktijdig waarnemen verbetert de signaal-ruisverhouding waardoor het koude neutrale medium beter waargenomen kan worden. Ten derde worden laagfrequente CRRLs waargenomen als absorptie (in tegenstelling tot emissie), en hierdoor zijn de detecties alleen gelimiteerd door de hoeveelheid van absorberend gas en niet door de afstand tot het gas. Dit maakt het mogelijk om CRRLs op zeer grote afstanden waar te nemen, waar vrijwel niets bekend is over de koude neutrale medium inhoud van sterrenstelsels.

Door waarnemingen van deze koolstof-radio-recombinatielijnen te vergelijken met gedetailleerde theoretische modellen is het mogelijk om informatie te verkrijgen over de temperatuur en dichtheid van het koude neutrale medium. Deze modellen werden ontwikkeld in de jaren 60 en 70 en zijn pas recent uitgebreid om ook de laagst waarneembare radiofrequenties te omvatten (Salgado et al., verstuurd). Ontwikkelingen op computergebied maken het mogelijk om een nauwkeurige berekening te doen van de benodigde kwantiteiten om de electronpopulatie in koolstofatomen te berekenen, alsook een complete studie van hoe de stimulatie van de grondtoestand van koolstof de sterkte van CRRLs kan beinvloeden.

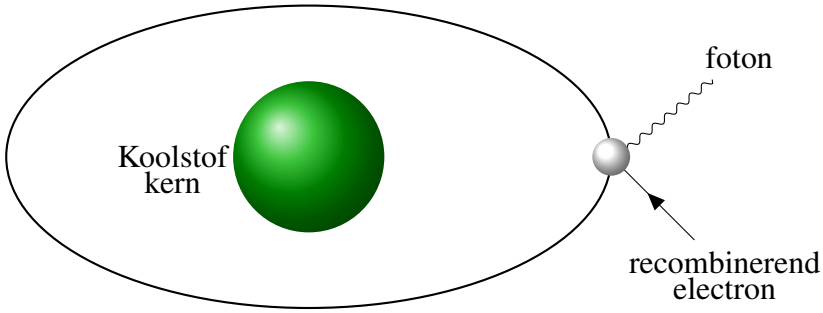

Figuur 3: Schematische weergave van een recombinerend koolstofatoom. De groene bal is de kern die protonen, neutronen en vijf electronen bevat. De witte bal is een vrij electron dat ingevangen is door de koolstofkern. Bij dit proces komt een foton vrij.

De Low Frequency Array

De resolutie die een telescoop kan halen is gerelateerd aan de waarneemfrequentie en de grootte van de telescoop. Voor een hoge resolutie bij lage frequenties zijn telescoopschotels nodig die zo groot zijn dat het onpraktisch wordt. Radiosterrenkundigen gebruiken daarom vaak arrays van telescopen. Het combineren van de signalen van individuele telescopen vormt effectief een instrument met de eigenschappen van een vele malen grotere telescoop. Dit proces noemt men interferometrie.

De Low Frequency Array (LOFAR; van Haarlem et al., 2013) is een nieuwe radio-interferometer met een revolutionair fase-array ontwerp dat gebruikt maakt van electronisch gerichte dipolen in plaats van de traditionele schotelantennes. De simpele dipoolantennes zijn gegroepeerd in stations. Er liggen 37 stations geconcentreerd in Nederland, en verder zijn 12 stations verspreid over 5 andere Europese landen. Er zitten twee verschillende dipooltypes in elk station. De High Band Array (HBA) werkt net boven de FM-radioband en bestaat uit dunne metalen dipolen ondersteund door piepschuim en afgeschermd van weersinvloeden. De Low Band Array (LBA), waarop de focus van dit proefschrift ligt, werkt net onder de FM-radioband en is het meest gevoelig rond 60 MHz. Elke LBA-antenne bestaat uit twee simpele draaddipolen vastgemaakt aan de grond, en op het hoogste punt in het midden worden ze ondersteund door een plastic buis. De locatie van de stations wordt getoond in Figuur 4, samen met een overzichtsfoto van een station en een detailfoto van de LBA-dipolen.

De meeste LOFAR-waarnemingen gebruiken alleen de Nederlandse stati-

Figuur 4: *Boven:* De locaties van LOFAR-stations. De data in dit proefschrift werd genomen voor de bouw van de stations in Polen, toen de langste basislijn lag tussen Onsala en Nançay (1292 km). *Midden:* Het LOFAR-UK-station in Chilbolton. De LBA-antennas liggen op de voorgrond met daarachter de HBA-antennes bij elkaar onder een weerbestendige bedekking. *Onder:* Dipolen van een LBA-station in de centrale kern van LOFAR, met de auteur voor schaal.

ons, waarbij een beeldveld 40 keer groter dan de volle maan wordt bestreken, en waarbij het kleinst waarneembare object aan de nachthemel zo groot lijkt als Mars. De wijde geografische verdeling van internationale stations geeft LOFAR een effectief verzamelgebied met een diameter van meer dan 1000 kilometer. Dit levert resoluties op die een factor 10 beter zijn dan alleen de Nederlandse kernstations. Deze resolutie is vergelijkbaar met de grootte van een Amerikaanse penny of een 10 eurocentmuntje op 8 kilometer (5 mijl) afstand. Deze eigenschap onderscheidt LOFAR van andere laagfrequente arrays en staat ons toe om compleet andere wetenschappelijke problemen te onderzoeken.

Met nieuwe technologische ontwikkelingen komen nieuwe uitdagingen. Laagfrequente radiotelescopen werken in een frequentiegebied waar de ionosfeer een grote invloed kan hebben op waarnemingen. Waarbij stationaire radiobronnen lijken te bewegen en/of scintilleren in afbeeldingen, zoals sterren lijken te twinkelen als men die met het blote oog door een turbulente atmosfeer bekijkt. Nieuwe calibratietechnieken zijn nodig om deze effecten uit de radiodata te verwijderen. En het probleem is dat dit voor de volledige International LOFAR zelfs nog lastiger wordt, aangezien de signalen van geografisch geisoleerde stations komen. Met fouten in de positie van de stations, fouten in de tijdsklokken, en met fouten afkomstig van de voortplanting van radiogolven bij verschillende atmosferische omstandigheden moet rekening gehouden worden.

Dit proefschrift

Het doel van dit proefschrift is om door middel van laagfrequente radiosterrenkundige technieken de volgende vragen helpen te beantwoorden:

- Zijn verafgelegen radiosterrenstelsels fundamenteel andere objecten dan hun nabijgelegen tegenhangers?
- Wat veroorzaakt de correlatie tussen de spectrale index in het radiogebied en afstand?
- Hoe groot is de koud gas inhoud van radiosterrenstelsels, en hoe speelt het een rol in de cyclus van sterformatie?

In het bijzonder gebruikt dit proefschrift de volgende data om de vragen te beantwoorden: (i) catalogi van bronnen afkomstig van LOFAR afbeeldingen die zwakkere sterrenstelsels laten zien dan eerder waargenomen op deze lage frequenties; (ii) afbeeldingen met de allerhoogste resoluties op frequenties lager dan 100 MHz genomen met de International LOFAR LBA-stations; en (iii)

waarnemingen van spectrale kenmerken afkomstig van LOFAR en de Karl G. Jansky VLA (VLA).

Hoofdstuk 2 onderzoekt of de geprojecteerde groottes van radiobronnen bestaande aanwijzingen ondersteunen dat de orientatierichting van een actief stelsel direct gerelateerd is aan de waargenomen kenmerken (de andere verklaring is dat objecten met verschillende kenmerken intrinsiek anders zijn). De kijkhoek bepaalt of de waarnemer de stoffige torus vanaf de zijkant (radiosterrenstelsel) of de schijf van verzamelend materiaal binnen in de torus (quasar) ziet. Met behulp van data uit een catalogus van LOFAR-gedetecteerde radiobronnen van Williams et al. (2016) vinden we dat de LOFAR-gedetecteerde radiosterrenstelsels gemiddeld 3.1 ± 1.0 keer groter zijn dan quasars, wat bewijs levert voor een unificatie op basis van orientatie.

Hoofdstuk 3 is een gedetailleerde studie op 55 MHz van 4C 43.15, een object uit een verzameling van 10 verafgelegen FR II radiosterrenstelsels. Dit hoofdstuk presenteert de allerhoogste resolutieafbeeldingen lager dan 100 MHz, genomen met International LOFAR. De beelden van dit radiostelsel laten een brug van radio-emissie zien tussen de twee FR II radiolobben, de eerste keer dat dit fenomeen is gezien in een ver radiostelsel. De waargenomen eigenschappen van 4C 43.15 zijn vergelijkbaar met die van lokale radiostelsels, inclusief de spectrale index in het radio gebied gecorrigeerd naar het ruststelsel. Dit impliceert dat verafgelegen radiosterrenstelsels fundamenteel gelijk zijn aan hun lokale tegenhangers.

Hoofdstuk 4 onderzoekt of de relatie tussen spectrale index en roodverschuiving ($\alpha - z$) simpelweg kan ontstaan door oplopende energieverliezen op hogere frequenties in het radiospectrum door de aanwezigheid van de kosmische achtergrondstraling (CMB), dat toeneemt als $(1 + z)^4$. Dit hoofdstuk neemt een nieuwe benadering door archiefdata te selecteren voor ongeveer 50 lokale radiosterrenstelsels met genoeg data om hun hele radiospectrum te reconstrueren, en door deze te gebruiken om radiospectra te simuleren van radiostelsels op hoge roodverschuiving. We vinden dat de waargenomen relatie volledig kan worden gereproduceerd met alleen de oplopende synchrotronverliezen vanwege inverse Comptonverstrooiing met fotonen van de CMB op hoge roodverschuiving, zonder gebruik te maken van een intrinsieke α-macht relatie of omgevingsfactoren.

Hoofdstuk 5 presenteert de eerste detectie van CRRLs in een ander sterrenstelsel dan het onze. Dit sterrenstelsel is het nabijgelegen M82, dat een intense, kortdurende periode van sterformatie ondergaat. Dit is de eerste extragalactische detectie van RRLs van een element anders dan waterstof en beneden de 1 GHz. De laagfrequente CRRLs komen van koolstofatomen die aanwezig zijn

in het hart van M82 en die het koude neutrale medium volgen. Door 22 CRRLs op te tellen in het frequentiegebied 48-64 MHz, corresponderend met energieniveaus (quantum niveaus) van $n = 468 - 508$, wordt een 8.5σ detectie bereikt. Recombinatie naar zo een hoge energieniveaus betekent dat de koolstofatomen ongeveer 2.1 micron in grootte zijn. Het lijnprofiel lijkt gecorreleerd te zijn met koud atomisch gas in het kerngebied van M82, wat de verwachtingen op basis van CRRLs in onze Melkweg bevestigd.

Hoofdstuk 6 bouwt verder op Hoofdstuk 5, aangezien de eerder beschreven CRRL-detectie niet genoeg data bevat om te vergelijken met gedetailleerde modellen en daarmee de gas temperatuur en -dichtheid af te leiden. Met behulp van VLA-waarnemingen in een hoger frequentiegebied (250−480 MHz) tellen wij 12 CRRLs op om een betekenisvolle bovenlimiet te vinden waarmee we de gastemperatuur en -dichtheid met behulp van modellen kunnen beperken. We vinden dat de gastemperatuur en -dichtheid consistent zijn met de waardes van het koude neutrale medium.

Hoofdstuk 7 beschrijft de berekening van gebonden-gebonden Gaunt factoren voor energieniveaus tot aan $n = 2000$. Deze factoren worden gebruikt om oscillatorsterktes te berekenen; een van de benodigde kwantiteiten in de verbeterde theoretische modellen van CRRLs (Salgado et al., 2016a,b). Een overzicht wordt gegeven van verschillende rekenmethodes, met een nadruk op de computationele problemen waardoor eerdere auteurs hun toevlucht zochten tot benaderingen met grote onzekerheid. De nieuwe berekeningen hebben de onzekerheid met meer dan factor 10 verbeterd. Deze waardes zijn bruikbaar voor een groot aantal natuurkundige toepassingen, en zijn daarom getabuleerd en online beschikbaar gemaakt.

In het algemeen heeft dit proefschrift twee grote conclusies:

- Verre radiosterrenstelsels lijken op hun lokale tegenhangers
- Koolstof-radio-recombinatielijnen zijn detecteerbaar in extragalactische bronnen en kunnen een krachtige techniek zijn om de eigenschappen van het koude neutrale medium in verre sterrenstelsels te bepalen

English Summary

Active Galaxies

At the heart of almost every massive galaxy resides a black hole that is millions to billions times more massive than the sun. Most galaxies are host to dormant black holes. In a fraction of galaxies, the black holes are observed to interact with their host galaxies, as they draw in and accumulate gas into a bright, hot disk of material that swirls around them like water around a drain in a bathtub. When the black hole of a galaxy is being fed in such a manner, the galaxy is called an 'active galaxy.' The disk of accumulating material around a black hole is tiny when compared to the size of the entire galaxy, but can produce enough optical light to outshine the light from the rest of the galaxy. This bright light coming from a very compact disk appears as a point-like source, comparable to a star, to an observer on Earth, leading to the name quasi-stellar or *quasar*. Active galaxies have a variety of different characteristics, and not all of them are quasars. The disk of accumulating material can be surrounded by dusty molecular gas. This dusty gas becomes warmer as it absorbs the light from the disk, which makes it glow bright in the infrared. Since everything on the sky is seen in two rather than three dimensions, sometimes the orientation of a galaxy means the dusty gas will block the light of the disk, and while we know the galaxy is an active galaxy, a quasar is not observed. There are other observational characteristics that will also depend on orientation, and astronomers use a wide variety of clues to identify active galaxies. Figure 1.3 shows a diagram of the region around the black hole in a radio loud active galaxy.

Radio Galaxies

About 10 per cent of active galaxies also produce jets of plasma moving at relativistic speeds. These jets produce radio emission from electrons circling in magnetic fields, a process called synchrotron radiation. These bright, powerful jets comprise two classes with distinct morphological features. Figure 2 shows

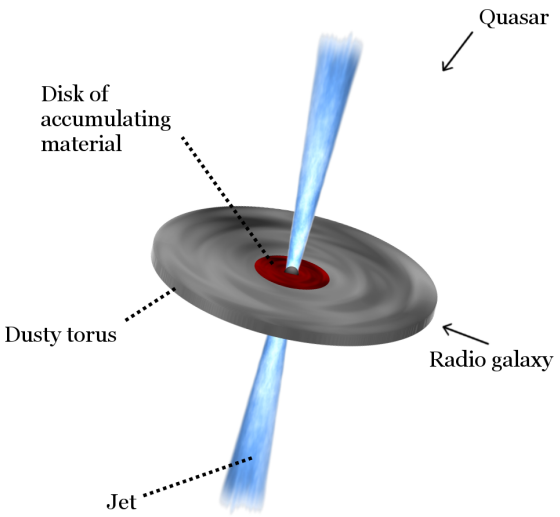

Figure 1: A diagram of the black hole and surrounding region in an active galaxy. The jet is only present in about 10 per cent of active galaxies, which are termed 'radio-loud'. Active galaxies can exhibit different observed features based on its orientation with respect to the observer, and the arrows indicate the type of object that is seen based on viewing angle. Image credit J. Harwood.

examples of the two different classes: Fanaroff-Riley I (FR I) sources which have radio jets that are more like fountains, with wider jets that are dimmer towards their edges; and Fanaroff-Riley II (FR II) sources, which have highly directional radio jets that are brightest where the jets terminate.

Distant radio galaxies are thought to evolve into the most massive galaxies in the present day Universe, and often the space around them has more galaxies than expected. They are therefore important beacons for studying galaxy evolution, as populations of galaxies can be studied as they traverse into clusters of galaxies, which are the largest gravitationally bound objects in the Universe. The more distant radio galaxies exhibit different characteristics to local radio galaxies, and it is not understood if these differences are intrinsic or environmental. One of the most intriguing differences between local and distant radio galaxies is that the more distant a radio galaxy is, the steeper its radio spectrum is (the steepness is measured by the spectral index parameter, α). The relation between radio spectral index and redshift (an astronomical distance measurement) has been successfully exploited in the past to find some of the most distant galaxies. However the cause of the relation still remains unknown.

Carbon Radio Recombination Lines

The cycle of star formation plays a key part in shaping a galaxy's evolution. The interstellar medium (ISM) provides the fuel to make new stars and is the reposi-

Figure 2: Examples of typical Fanaroff-Riley FRI and FRII sources. *Left:* FRI radio galaxy Centaurus A. The color purple shows the radio emission (Credit: X-ray: NASA/CXC/CfA/R.Kraft et al; Radio: NSF/VLA/Univ.Hertfordshire/M.Hardcastle; Optical: ESO/WFI/M.Rejkuba et al.). *Right:* Cygnus A, the archetypal FRII radio galaxy. The color red shows the edge-brightened radio emission. (Credit: X-ray: NASA/CXC/SAO; Optical: NASA/STScI; Radio: NSF/NRAO/AUI/VLA).

tory for the ejecta of old stars. There are many different components of the ISM, and understanding how all of these components contribute to star formation is critical to understanding galaxy evolution. One of the least known components of the ISM is the cold neutral medium, which is over 10^{19} times less dense than air on Earth, and a couple hundred degrees below 0 degrees Celsius. This nebulous gas consists mostly of neutral hydrogen atoms, and carbon atoms that are singly ionised (that is, they are missing an electron).

Carbon atoms normally have six protons and six electrons and are about half a million times smaller than the average thickness of a human hair. The outermost electron is easily bumped out of orbit by low-level ultraviolet radiation, leaving behind a singly-ionised carbon atom. In the cold neutral medium, these carbon ions co-exist with free electrons and neutral hydrogen atoms. The free electrons can be re-captured by the carbon ions in a process called recombination (see Figure 3 for a depiction). When the recombination happens to a high energy level ($n \geq 300$), the process produces spectral features at low radio frequencies ($\leq 240\,\mathrm{MHz}$). There are many of these carbon radio recombination lines (CRRLs) in the radio frequency range, but they are strongest below the FM radio band.

Observing CRRLs at low frequencies has three main advantages. First, they are easier to detect because the physical processes involved increase their

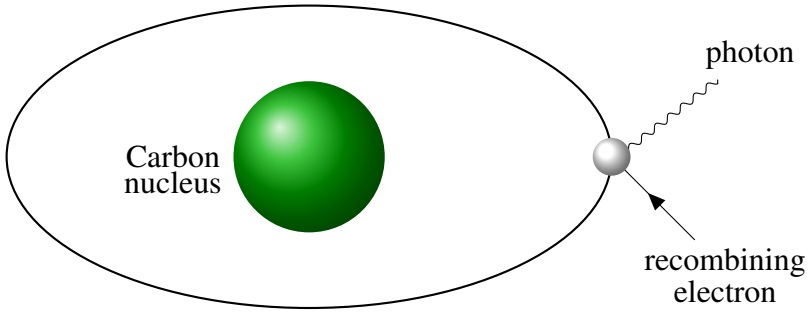

Figure 3: A depiction of a recombining carbon atom. The green ball represents the nucleus, which includes protons, neutrons, and five electrons. The white ball represents a free electron which has been captured by the carbon nucleus, a process which emits a photon.

strength. Second, the lines are closer together in frequency at lower frequencies, and instruments with wide bandwidths can observe multiple CRRLs simultaneously. Considering multiple CRRLs simultaneously will increase the signal to noise ratio, providing better data with which to observe the cold neutral medium. Third, low-frequency CRRLs are seen as absorption features (rather than emission features), and detections are limited only by the amount of absorbing gas present and not the distance to the gas. This opens up the possibility of observing CRRLs at very large distances, where virtually nothing is known about the cold neutral medium content of galaxies.

By comparing observations of these carbon radio recombination lines to detailed theoretical models it is possible to gather information on the temperature and density of the cold neutral medium. These models were developed in the 1960's and 1970's and have only recently been expanded to include the lowest observable radio frequencies (Salgado et al., submitted). Advances in computing have also allowed for more accurate computation of the necessary quantities to calculate the electron population in carbon atoms, as well as a complete treatment of how the stimulation of the ground state of carbon can impact the strength of CRRLs.

The Low Frequency Array

The resolution a telescope can achieve is related to the observed frequencies, and the size of the telescope. High resolution at low frequencies requires telescopes so large that they are impractical, and radio astronomers often use arrays of

telescopes. Combining the signals from individual telescopes effectively creates an instrument with the desired properties of a much larger telescope. This is a process called interferometry.

The Low Frequency Array (LOFAR; van Haarlem et al., 2013) is a new radio interferometer with a revolutionary phased-array design that makes use of electronically pointed dipoles rather than traditional dish telescopes. The simple dipole antennas are grouped into stations. There are 37 stations concentrated in the Netherlands, and 12 stations spread across five other European countries. There are two different types of dipoles in each station. The High Band Array (HBA) operates just above the FM radio band and consists of thin metal dipoles supported by Styrofoam and protected from the weather. The Low Band Array (LBA), which is the focus of this thesis, operates just below the FM radio band and is most sensitive around 60 MHz. Each LBA antenna consists of two simple wire dipoles attached to the ground and supported at their apex in the center by a plastic pipe. The station locations are shown in Figure 4, along with a bird's eye view of a station, and a close up of the LBA dipoles.

Most LOFAR observations use only the stations in the Netherlands, which provide fields of view 40 times larger than the full moon, and the smallest object that can be resolved is about the size of Mars in the night sky. The wide geographic distribution of international stations provides LOFAR with an effective collecting area more than a thousand kilometres across, allowing resolutions ten times better to be achieved. This is equivalent to the size of a US penny or 10 euro cent coin that is 8 kilometres (5 miles) away. This capability sets LOFAR uniquely apart from other low-frequency arrays, and enables exploration of entirely different science topics.

With new technological advances come new challenges. Low frequency radio telescopes operate in a frequency range where the ionosphere can have a large impact on observations, causing stationary radio sources to appear to move and/or scintillate in an image, just like stars seem to twinkle when seen with the naked eye through turbulent atmosphere. New calibration techniques are necessary to remove this effect from the radio data, and the problem is even more challenging when using the full International LOFAR, as it is challenging to combine signals from geographically isolated stations. Errors in station positions, different station clocks, and errors from propagation through different atmospheric conditions must all be accounted for.

Figure 4: *Top:* The locations of LOFAR stations. The data in this thesis were taken before the stations in Poland were constructed, when the longest baseline was between Onsala and Nançay (1292 km). *Middle:* The LOFAR-UK station at Chilbolton. The LBA antennas are in the foreground with the HBA antennas clustered together under a weather-protective covering behind the LBA. *Bottom:* Dipoles from an LBA station within the central core of LOFAR, with the author in the picture for scale.

This Thesis

The goal of this thesis is to use low frequency radio astronomy tools to help answer the following questions:

- Are more distant radio galaxies fundamentally different objects than their nearby counterparts?
- What causes the correlation between radio galaxy spectral index and distance?
- What is the cold gas content in radio galaxies, and how does it play a part in the cycle of star formation?

In particular, this thesis uses several tools to help answer these questions: (i) catalogues of sources from LOFAR images that detect fainter galaxies than ever before detected at low frequencies; (ii) images with the highest resolution at frequencies below 100 MHz using the International LOFAR LBA stations; and (iii) observations of spectral features from both LOFAR and the Karl G. Jansky VLA (VLA).

Chapter 2 investigates whether the projected sizes of radio sources support other evidence that the orientation of an active galaxy on the sky directly informs the observed characteristics (the other alternative is that objects with different characteristics are intrinsically different). The viewing angle dictates whether the observer sees the obscuring torus edge on (radio galaxy) or is able to see the disk of accumulating material inside the torus (quasar). Using data from a catalogue of LOFAR-detected radio sources from Williams et al. (2016) we find that the radio galaxies are on average 3.1 ± 1.0 times larger than the quasars for the LOFAR-detected radio sources, which is evidence for orientation-based unification.

Chapter 3 is a detailed study at 55 MHz of 4C 43.15, one of a sample of 10 distant FR II radio galaxies. This chapter presents the highest resolution images below 100 MHz, using the International LOFAR. The images of this radio galaxy reveal a bridge of radio emissions between the two FR II radio lobes, the first time this has been seen in a distant radio galaxy. The observed properties of 4C 43.15 are similar to those seen in local radio galaxies, including the rest-frame radio spectral index. This implies that distant radio galaxies are fundamentally the same as their local counterparts.

Chapter 4 investigates whether the relation between spectral index and redshift ($\alpha - z$) can arise simply due to increased energy losses at higher frequencies in the overall radio spectrum due to the proximity of the cosmic microwave

background (CMB), which increases as $(1+z)^4$. This chapter uses a new approach of selecting archival data for ~50 local radio galaxies with enough data available to model their entire radio spectra, and using these to simulate radio spectra of radio galaxies at higher redshifts. We find that the observed relation can be entirely reproduced with only the increased synchrotron losses due to inverse Compton scattering of photons from the CMB at high redshift, without having to invoke any intrinsic α-power relationship or environmental effects.

Chapter 5 presents the first detection of CRRLs in a galaxy other than our own. This galaxy is nearby M82, which is undergoing an intense, short-lived period of star formation. This is the first extragalactic detection of RRLs from a species other than hydrogen, and below 1 GHz. The low frequency CRRLs come from carbon atoms that are present in the heart of M82 and trace the cold neutral medium. By stacking 22 CRRLs in the frequency range of 48-64 MHz, corresponding to energy levels (quantum levels) of $n = 468 - 508$, an 8.5σ detection was achieved. Recombination to such high levels mean that the Carbon atoms are about 2.1 microns in size. The line profile appears to be correlated with cold atomic gas in the nuclear region of M82, confirming what is expected from observations of CRRLs in the Milky Way.

Chapter 6 builds on Chapter 5, as the CRRL detection described therein does not provide enough data to compare with the detailed models to constrain the gas temperature and density. Using VLA observations at a higher frequency range (250−480 MHz) we stacked 12 CRRLs to find a meaningful upper limit with which to constrain the gas temperature and density by comparison with models. We find that the gas temperature and density are consistent with Galactic values for the cold neutral medium.

Chapter 7 describes the calculation of bound-bound Gaunt factors for levels up to $n = 2000$. These factors are used to calculate oscillator strengths, one of the necessary quantities in the updated theoretical models of CRRLs (Salgado et al., 2016a,b). A review is presented of various calculation methods, with particular attention given to the computational problems that led previous authors to use approximations with large errors. The new calculations have improve the errors by more than a factor of 10. The values are useful for a wide range of physical applications, and are tabulated and published online.

Overall, this thesis has two major conclusions:

- Distant radio galaxies look like their local counterparts
- Carbon radio recombination lines are detectable in extragalactic sources and can be powerful tools for measuring the properties of the cold neutral medium in distant galaxies

Publications

Refereed first author publications

- **Morabito, L. K.**, Deller, A. T., Röttgering, H., et al., *LOFAR VLBI studies at 55 MHz of 4C 43.15, a z= 2.4 radio galaxy*, 2016, MNRAS, 461, 2676
- **Morabito, L. K.**, Oonk, J. B. R., Salgado, F., et al., *Discovery of Carbon Radio Recombination Lines in M82*, 2014, ApJL, 795, L33
- **Morabito, L. K.**, van Harten, G., Salgado, F., et al., *Exact bound-bound Gaunt factor values for quantum levels up to n = 2000*, 2014, MNRAS, 441, 2855
- **Morabito, L. K.**, Dai, X., Leighly, K. M., Sivakoff, G. R., & Shankar, F., *Unveiling the Intrinsic X-Ray Properties of Broad Absorption Line Quasars with a Relatively Unbiased Sample*, 2014, ApJ, 786, 58
- **Morabito, L. K.**, & Dai, X., *A Bayesian Monte Carlo Analysis of the M-σ Relation*, 2012, ApJ, 757, 172
- **Morabito, L. K.**, Dai, X., Leighly, K. M., Sivakoff, G. R., & Shankar, F., *Suzaku Observations of Three FeLoBAL Quasi-stellar Objects: SDSS J0943+5417, J1352+4239, and J1723+5553*, 2011, ApJ, 737, 46

Refereed co-author publications

- Williams, W. L., van Weeren, R. J., Röttgering, H. J. A., et al., *LOFAR 150-MHz observations of the Boötes field: catalogue and source counts*, 2016, MNRAS, 460, 2385
- Varenius, E., Conway, J. E., Martí-Vidal, I., et al., *Subarcsecond international LOFAR radio images of Arp 220 at 150 MHz: A kpc-scale star forming disk surrounding nuclei with shocked outflows*, 2016, arXiv:1607.02761
- Shimwell, T. W., Luckin, J., Brüggen, M., et al., *A plethora of diffuse steep spectrum radio sources in Abell 2034 revealed by LOFAR*, 2016, MNRAS, 459, 277
- Williams, W. L., van Weeren, R. J., Röttgering, H. J. A., et al., *LOFAR 150-MHz observations of the Boötes field: Catalogue and Source Counts*, 2016, arXiv:1605.01531
- Heald, G. H., Pizzo, R. F., Orrú, E., et al., *The LOFAR Multifrequency Snapshot Sky Survey (MSSS). I. Survey description and first results*, 2015, A&A, 582, A123

- Oonk, R., **Morabito, L.**, Salgado, F., et al., *The Physics of the Cold Neutral Medium: Low-frequency Radio Recombination Lines with the Square Kilometre Array*, 2015, Advancing Astrophysics with the Square Kilometre Array (AASKA14), 139
- Varenius, E., Conway, J. E., Martí-Vidal, I., et al., *Subarcsecond international LOFAR radio images of the M82 nucleus at 118 MHz and 154 MHz*, 2015, A&A, 574, A114
- Moldón, J., Deller, A. T., Wucknitz, O., et al., *The LOFAR long baseline snapshot calibrator survey*, 2015, A&A, 574, A73
- Oonk, J. B. R., van Weeren, R. J., Salgado, F., et al., *Discovery of carbon radio recombination lines in absorption towards Cygnus A*, 2014, MNRAS, 437, 3506

Conference proceedings

- **Morabito, L.**, Deller, A., Moldón, J., et al., *A LOFAR survey of spatially resolved Ultra Steep Spectrum sources*, 2015, The Many Facets of Extragalactic Radio Surveys: Towards New Scientific Challenges, 71
- **Morabito, L. K.**, Deller, A., Oonk, J. B. R., Röttgering, H., & Miley, G., *Spatially resolved studies of extragalactic jets in high redshift radio galaxies*, 2015, Extragalactic Jets from Every Angle, 313, 231
- Toribio, M. C., **Morabito, L. K.**, Oonk, J. B. R., et al., *Radio Recombination Line studies on M82 from LOFAR HBA observations*, 2015, Galaxies in 3D across the Universe, 309, 350
- **Morabito, L. K.**, Oonk, J. B. R., Salgado, F., et al., *Discovery of Carbon Radio Recombination Lines in M82*, 2015, Galaxies in 3D across the Universe, 309, 141
- Moldon, J., Deller, A., Wucknitz, O., et al., *The LOFAR long baseline snapshot calibrator survey*, 2014, Proceedings of the 12th European VLBI Network Symposium and Users Meeting (EVN 2014). 7-10 October 2014. Cagliari, Italy. Online at `http://pos.sissa.it/cgi-bin/reader/conf.cgi?confid=230`, id.97, 97
- Dai, X., **Morabito, L. K.**, Shankar, F., Sivakoff, G. R., & Leighly, K. M., *Large BALQSO Fractions Inferred from NIR and Radio Surveys: Implication to AGN and Feedback Models*, 2012, AGN Winds in Charleston, 460, 120
- **Morabito, L. K.**, Dai, X., Leighly, K. M., Sivakoff, G. R., & Shankar, F., *X-ray Observations of Broad Absorption Line Quasars*, 2012, American Astronomical Society Meeting Abstracts #219, 219, 154.06

Curriculum Vitae

I was born on 22 January, 1983 in Englewood, Colorado, USA. When I was five years old my family moved to Federal Way, Washington, where we lived within walking distance of Pugeot Sound. When I was ten years old my family moved to North Carolina, and four years later we moved again to Michigan. As a child I was an avid reader, and also watched all of the science programmes on television that I could. I developed a passion for anything space-related, from the smallest details of the US space program to science fiction. When I was 13 years old I went to Space Camp in Florida, and was the Pilot for the simulated space mission. When I was in high school, this helped prompt my decision to take a four-year scholarship in the Reserve Officer Training Corps for the US Air Force. I took this scholarship to the University of Michigan, where I earned a double major in both Physics and Astrophysics and graduated with an Angell Scholar award and membership in the National Physics Honors Society, Sigma Pi Sigma.

After graduation, I commissioned as an officer in the US Air Force and went to Florida for a year of specialized training to become an Air Battle Manager. Upon finishing training, I moved to Tinker Air Force Base in Oklahoma and qualified as an Air Weapons Officer (Distinguished Graduate) to fly on the E-3 Airborne Warning And Control System (AWACS). After a deployment to south-west Asia where I provided tactical control for aircraft in combat environments, I became qualified as an Electronic Combat Officer (ECO) and operated the Passive Detection System on the AWACS. Upgraded to Instructor ECO well before my peers, I garnered an 'Exceptionally Qualified' ranking and deployed again to south-west Asia. Upon returning to Oklahoma, I became an Evaluator ECO and the subject matter expert for all ECOs in the Air Force. Over the course of my military career, I earned multiple distinctions including two Air Medals (for flying combat hours), and an Air Force Achievement Medal (for leading the deployed Electronic Support Team).

During my last two years in the Air Force, I began working on my master's degree in Astronomy at the University of Oklahoma with X. Dai. I worked on X-ray observations of broad absorption line quasars, and developed a new method to determine their intrinsic X-ray weakness. During this time I also helped out with multiple observing runs on the optical 2.4 m Hiltner Telescope at the MDM Observatory adjacent to Kitt Peak in Arizona. I separated from the Air Force in 2011 and after earning my master's degree in May 2012 I spent three months at the National Radio Astronomy Observatory in Socorro, New Mexico, working with D. Meier, E. Momjian, and J. Ott on radio observations from the Very Large Array. I used these data to search for ammonia lines in nearby star-forming galaxies.

In September 2012 I began my PhD at Leiden Observatory under the guidance of H. Röttgering. My work in the last four years has focused on using low frequency radio astronomy to better understand the physical processes both in distant radio galaxies and in the cold neutral medium. My time has been divided between theoretical work on carbon radio recombination line models, commissioning work for the Low Frequency Array (LOFAR), and developing new methods to calibrate LOFAR data for observational projects. In addition to this, I have performed observing runs on the Isaac Newton Telescope on La Palma, and was the teaching assistant for the Radio Astronomy master's course in 2015. I have presented my work at international conferences and institutes in the United States, the United Kingdom, the Galápagos Islands, Germany, Austria, South Africa, and the Netherlands. I have also organised multiple LOFAR busy weeks for the purpose of commissioning work.

In October 2016 I will begin a post-doctoral researcher position at the University of Oxford in Oxford, the United Kingdom. I will continue to work on the topic of galaxy evolution from a radio perspective, but broaden my experience to include multi-wavelength data for a more complete analysis.

Acknowledgements

I would first like to thank Huub for the wonderful opportunity to work on my PhD at Leiden, and his continued support over the last four years. I am also very grateful for the enthusiastic support of George. I spent quite a bit of time at ASTRON learning about LOFAR and for this I have to thank George H., Michiel, and Maaijke. This thesis has also benefited greatly from the endlessly enthusiastic help of Tammo Jan. To my other ASTRON friends, thank you for putting up with me invading your offices and pestering you with questions. I especially appreciate the friendship and support of Liz and Tom.

This thesis relied heavily on computing resources, and would not have been possible without all the help from the Sterrewacht computer group. In particular, I want to say thank you to David for his help with LOFAR software installations (and all the problems that came with that). Also thanks to Erik and David for their help with the new parallel cluster.

Through the LOFAR Surveys Key Science Project I have met many people who have become mentors, friends, and valued co-workers, and I am grateful to be a part of this collaboration. I especially appreciate all of the interesting questions, discussions, and support I received from Glenn, Phillip, Neal, Michael W., and Gianfranco. For a deeper understanding of the unique problems of using the LOFAR long baselines, I have to thank Javier, Eskil, Adam, and Neal. I have learned so much from you, and I appreciate your patience and enthusiasm.

Thanks to Huib and Mike for taking me as their teaching assistant for Radio Astronomy, and giving me the freedom to design my own practical project. Thanks also to the students who were always engaged and had thoughtful questions. The course allowed me to share my deep enthusiasm for radio astronomy, and I am always grateful to be reminded how much I actually love what I do!

There are several key people at Leiden from whom I have learned so much about both science and life. I am deeply thankful to count Emma, Wendy, Tim, David, and Henriette among my friends. I have learned so much both professionally and personally from each of you. Emma, thank you for your scientific guidance, your daily presence in my life, the hugs when I needed them, and for being someone with whom I could share my passion for reading and feminist discourse. Wendy, I am always in awe of your quiet competence and the excel-

lence that you apply to everything in your life. Tim, I have learned more about radio astronomy from you than anyone else, and you have also been a great friend. David, thanks for all of the afternoon tea breaks and the conversations. Henriette, thank you for reminding me that there is life outside of work – we have done a lot of fun things together!

The inappropriately named 'LOFAR research group' has expanded well beyond LOFAR in my time at Leiden. I would like to thank all of its members for their help and friendship: Aayush, Andra, Huib I., Soumyajit, Ken, Francesco, Kim, Gaby, Duy, Edwin, Alex, Josh, Bas, and Pedro. Huib, I very much appreciated your enthusiasm, patience, and positive attitude. I have yet to have a conversation with you and *not* learn something wonderful. I must also thank my fellow Oort 464 occupants. Aayush: thank you for all your help over the past year, and I'm glad we got the chance to become friends. Julius: thanks for being such an awesome friend! I admire how you are always thinking, and open to new ideas. Thanks also to Gilles, for translating my summary into het Nederlands! Thanks also to all those I've spent time with at the Sterrewacht over the past four years – it is wonderful to have so many friends and valued colleagues that I can't list you all. If I have forgotten anyone, the fault is entirely mine.

To my friends abroad: Laura C., it has been truly wonderful breaking out of my astronomy shell with you and having silly adventures and craft nights. I look forward to many more in the future. Katey, I am so grateful for your friendship. You are an amazing scientist and a wonderful, passionate, and compassionate person. My life has been forever changed for the better from knowing you. Thank you Patty (and Bernie!) for your friendship and support. Thank you Jimmy, for putting up with me all of these years and always being the voice of reason. Amy, you are such a lovely person and I am thankful for your friendship and the fun we've had. Thanks also to Jon Z. and Jeremy for being good friends.

Thank you very much to my parents for always supporting my decisions, and being there for me when I needed it. I appreciate your continued love and support more than you know. Corentin, je te suis tellement reconnaissante d'être avec moi pour partager ce moment important de ma vie, et je suis impatiente des futurs bons moments à venir. Finally, to my best friend Laura. From the moment we met, we started having adventures together, even if they were just on paper at first. We've been friends for over 20 years now, and I cannot imagine life without your love and support. Thank you for always being there to pick me up when I'm down, encourage me when I need a push, celebrate and share major life events, and most especially for being proud of me when I succeed.